UNIVERSIDAD COMPLUTENSE DE MADRID

FACULTAD DE CIENCIAS FÍSICAS

Departamento de Física de Materiales

TESIS DOCTORAL

Electronic properties of graphene on a piezoelectric substrate

Propiedades electrónicas del grafeno sobre un sustrato piezoeléctrico

MEMORIA PARA OPTAR AL GRADO DE DOCTOR

PRESENTADA POR

David González González

Directores

Francisco Guinea López
Fernando Sols Lucia

Madrid, 2019

UNIVERSIDAD
COMPLUTENSE
MADRID

Departamento de Física de Materiales

Electronic properties of graphene on a piezoelectric substrate

Propiedades electrónicas del grafeno sobre un sustrato piezoeléctrico

David González González

Tesis dirigida por

Francisco Guinea López y Fernando Sols Lucia

Contents

Resumen en español

En el presente trabajo investigamos teóricamente las propiedades electrónicas de una capa de grafeno sobre un sustrato piezoeléctrico. Concretamente, estudiamos el efecto de los modos de vibración acústicos de superficie sobre los electrones del grafeno. Este trabajo está dividido en seis capítulos y varios apéndices, siendo el objetivo de estos últimos el que el material sea lo más autocontenido posible.

El primer capítulo introduce una visión general de los actores principales en este trabajo. El grafeno es un material de dos dimensiones que ha atraído una atención creciente internacionalmente desde su aislamiento por Novoselov y Geim en 2004. Está formado por una red de átomos de carbono en forma de panal. El grafito, la forma más común de carbono puro, puede ser visto como si estuviera hecho por láminas de grafeno débilmente acopladas. El grosor atómico del grafeno, combinado con sus propiedades electrónicas únicas originadas por el comportamiento de sus electrones como si no tuvieran masa, convierte a este material en un objeto excepcional de elevado interés fundamental y aplicado.

Dado que este alótropo del carbono es un material atómicamente fino, la dinámica de sus portadores de carga es muy sensible a los campos electromagnéticos circundantes, y la posibilidad de cambiar la concentración de sus portadores de carga *in situ* aplicando un voltaje externo de puerta es una característica clave de muchos dispositivos basados en el grafeno. La altísima movilidad de los portadores en grafeno suspendido es posibilitada por las altas frecuencias de los fonones ópticos en esta dura red de panal.

Por consiguiente, los efectos del scattering de electrón-fonón en su transporte son pequeños en comparación con los de los metales convencionales. Sin embargo, en la mayoría de arquitecturas de dispositivos, el grafeno está depositado en un sustrato, y todos los modos de la red del sustrato que inducen un campo eléctrico influirán sobre los portadores de la lámina de grafeno, haciendo que la elección del sustrato sea crucial para determinar las características resultantes de transporte en el dispositivo.

Por otro lado, las ondas acústicas de superficie (SAWs, del inglés) creadas en materiales piezoeléctricos residen en la superficie de un sólido o en la interfase entre dos sólidos. Han sido utilizadas por mucho tiempo para controlar las propiedades de estructuras y materiales semiconductores. Las SAWs pueden ser usadas para convertir señales mecánicas en señales eléctricas y viceversa. Una primera descripción básica de la piezoelectricidad y de sus ondas de superficie en el primer capítulo es seguida a continuación por un estudio cuantitativo de su propagación y de sus principales características en el segundo capítulo (en parte en forma de *review*).

Además de la deformación mecánica, la vibración de la red iónica en un material piezoeléctrico produce un campo eléctrico que viaja con la SAW. Este campo puede transportar portadores de carga en una monocapa de grafeno depositada sobre dicho material, lo cual permite investigar, por ejemplo, la estructura de niveles de Landau del grafeno en presencia de un campo magnético externo. La necesidad de cuantificar los efectos tanto para SAWs macroscópicas como sus cuantos de vibración, los fonones acústicos, conduce al tercer capítulo. Ahí se estudia la interacción entre los electrones de un metal bidimensional y los fonones acústicos del sustrato piezoeléctrico subyacente. A partir de argumentos energéticos fundamentales se pueden obtener desigualdades generales.

Como resultado, se puede probar que la atracción mediada por fonones nunca supera la repulsión de Coulomb electrónica, al menos para longitudes de onda largas. Por tanto, en el cuarto capítulo estudiamos la influencia de dichos fonones en las interacciones electrón-electrón y en las posibles inestabilidades de apareamiento de un gas de electrones bidimensional como

el del grafeno.

En el quinto capítulo investigamos las propiedades *many-body* del grafeno sobre un sustrato piezoeléctrico, centrándonos en la interacción entre los electrones del grafeno y los fonones piezoeléctricos de superficie. Calculamos las autoenergías de electrones y de fonones, como también la movilidad electrónica limitada por los fonones del sustrato. Enfatizamos la importancia del correcto apantallamiento del vértice de la interacción electrón-fonón y discutimos diversos comportamientos límite como función de la energía del electrón, la temperatura y el nivel de dopaje. El efecto de los fonones acústicos de superficie en los electrones del grafeno se compara con el de los fonones intrínsecos de deformación del grafeno. Se comprobará que los fonones del sustrato tienden a dominar sobre los fonones intrínsecos para dopajes bajos prácticamente a cualquier temperatura.

El último capítulo contiene las conclusiones globales de este trabajo. Los resultados numéricos para los recorridos libres medios y las movilidades electrónicas mostradas se muestran aplicables para diversos materiales piezoeléctricos con diferentes estructuras de red y magnitudes piezoeléctricas. Nuestro estudio puede ser por tanto relevante para dispositivos de grafeno operando en el régimen de transporte balístico, y en escenarios donde la interferencia cuántica induce fenómenos de localización.

El trabajo presentado aquí ha dado lugar a las siguientes dos publicaciones: Refs. [1, 2]. Los dos primeros capítulos, así como los apéndices, contienen material relevante de *review*, donde no se sigue ninguna fuente concreta sino que se combinan varias referencias de forma creativa. En algunas de sus subsecciones se presenta trabajo original no incluido en las Refs. [1, 2]. El tercer y el cuarto capítulo están basados en el contenido de la Ref. [1], mientras que la Ref. [2] ha inspirado el quinto capítulo. En ambos capítulos se añaden algunos comentarios cualitativos y detalles de cálculo no incluidos en las publicaciones por brevedad.

Finalmente, me gustaría dar las gracias a Francisco Guinea y Fernando Sols por la dirección de la presente tesis doctoral. Asimismo, doy las gra-

cias a Ivar Zapata por su paciencia y enseñanzas; a Jürgen Schiefele, Fernando Calle y Jorge Pedrós por su trabajo y valiosos comentarios, a mis simpáticos compañeros del departamento de Física de Materiales de la Universidad Complutense de Madrid (especialmente a los buenos de Luis Ruiz-Valdepeñas y Juan Ramón Muñoz de Nova), y a mi padre Emiliano González y mi tía Ana María González por su apoyo.

Abstract

In the present work, we investigate theoretically the electronic propierties of a graphene layer on a piezoelectric substrate. Specifically, we study the effect of the surface acoustic vibration modes on the graphene electrons. This work is divided in six chapters plus several appendices whose goal is to render the material as self-contained as possible.

The first chapter introduces a basic survey of the main actors in this work. Graphene is a two-dimensional material that has received increasing worldwide attention since its isolation by Novoselov and Geim in 2004. It is formed by a honeycomb lattice of carbon atoms. Graphite, the most common form of pure carbon, can be viewed as made of weekly coupled graphene layers. The single-atom thickness of graphene, combined with its unique electronic properties stemming from the effectively massless behavior of electrons, converts this material into a special object of high fundamental and applied interest.

Because this carbon allotrope graphene is an atomically thin material, its charge-carrier dynamics is very sensitive to the surrounding electromagnetic fields, and the possibility of changing graphene's carrier concentration *in situ* by applying an external gate voltage is a key feature in many graphene-based devices. The extremely high carrier mobility in suspended graphene is enabled by the high frequencies of the optical phonons in the stiff honeycomb lattice. Thus, the effects of electron-phonon scattering on transport are small in comparison with conventional metals. However, in most device architectures, graphene is deposited on a substrate, and all lattice modes of

the substrate material that induce an electric field will influence the carriers in the graphene sheet, making the choice of substrate material crucial for the resulting transport characteristics of the device.

On the other hand, surface acoustic waves (SAWs) created in piezoelectric materials reside at the surface of a solid or at the interface between two solids. They have for long been used to control the properties of semiconductor materials and structures. SAWs may be used to convert mechanical into electric signals and vice versa. A first basic description of piezoelectricity (highlighting their huge variety of applications and its importance in physics, as well as the important scientists spending some time within its study) and these waves in the first chapter, is followed by a quantitative study of their propagation and main characteristics in the second chapter (in part review-like).

Apart from the mechanical deformation, the vibration of the ionic lattice in a piezoelectric material produces an electric field travelling along with the SAW. This field permits the transport of charge carriers in monolayer graphene deposited on top of the piezomaterial and, for instance, the probing of graphene's Landau level structure in the presence of an external magnetic field. The need to quantify those effects accurately both for macroscopic SAWs and their vibration quanta, the acoustic phonons, leads to the third chapter. There, the interaction between the electrons of a two-dimensional metal and the acoustic phonons of an underlying piezoelectric substrate is investigated. Fundamental inequalities can be obtained from general energy arguments.

As a result, phonon-mediated attraction can be proven to never overcome electron Coulomb repulsion, at least for long phonon wavelengths. Therefore, in the fourth chapter, we study the influence of these phonons on the electron-electron interactions and the possible pairing instabilities of a two-dimensional electron gas such as graphene.

In the fifth chapter, we investigate the many-body properties of graphene on top of a piezoelectric substrate, focusing on the interaction between the

graphene electrons and the piezoelectric acoustic phonons. We calculate the electron and phonon self-energies as well as the electron mobility limited by the substrate phonons. We emphasize the importance of the proper screening of the electron-phonon vertex and discuss the various limiting behaviors as a function of electron energy, temperature, and doping level. The effect on graphene electrons of the piezoelectric acoustic phonons is compared with that of the intrinsic deformation acoustic phonons of graphene. Substrate phonons shall be seen to tend to dominate over intrinsic ones for low doping levels virtually at any temperature.

The global conclusions of this work are contained in the last chapter. The numerical results for mean free paths and electron mobilities shown are seen to be applicable to a variety of piezoelectrical materials with different lattice structures and piezoelectric strengths. Our study can be thus relevant for graphene devices operating in the ballistic transport regime and for scenarios where quantum interference induces localization phenomena.

The work presented here has given rise to the following two publications: Refs. [1, 2]. The first two chapters, as well as the appendices, contain relevant review material where no particular source is followed but rather several different references are combined in a creative form. Some subsections there contain original work not included in the former references, especially in Sec. 2.4. The third and fourth chapters are based on the content of Ref. [1], while Ref. [2] has inspired the fifth chapter. Some qualitative comments and calculation details not included in the publications for the sake of brevity, are added to both chapters.

Finally, I would like to thank Francisco Guinea and Fernando Sols for the direction of this doctoral thesis. Likewise, I thank Ivar Zapata for their patience and teachings; Jürgen Schiefele, Fernando Calle and Jorge Pedrós for their work and valuable discussions, all my nice colleagues at the Materials Physics Department of the Universidad Complutense de Madrid (especially the friendly Luis Ruiz-Valdepeñas and Juan Ramón Muñoz de Nova), and my father Emiliano González and aunt Ana María González for their support.

Chapter 1

Introductory material

1.1 Graphene and other 2D van der Waals materials

Graphene has received great attention since its isolation in 2004 [3] and the Nobel Prize in Physics in 2010 awarded to the main discoverers: Konstantin Novoselov and Andre Geim [4]. This two-dimensional material has quickly received attention in many scientific-research fields ranging from the very theoretical solid-state physics, to particle physics, nuclear physics, experimental physics, chemistry, and related technological fields. There are many great reviews and books (in particular about the theoretical-physics topics addressed in this thesis, e.g., Refs. [5, 6, 7]).

For the non-expert reader, we can say that graphene consists essentialy of an atom-thick layer of graphite. It is just a 2D array of carbon, the atomic element of "life" and the organic chemistry. An element whose atoms have 6 protons, 6 electrons ($1s^2 2s^2 2p^6$ as electronic configuration) and two stable isotopes: ^{12}C (the most common, being 98.9% of the natural carbon, with zero nuclear spin, and having 6 neutrons), and ^{13}C (with finite nuclear spin from its 7 neutrons, but constituting just 1.1% of all natural carbon). Moreover, carbon has many unstable isotopes as well, mostly quite

short-lived (from nanoseconds to minutes) except for the widely known ^{14}C, whose half-life is around 5730 years, which allows to estimate the age of carbonaceous materials.

This sixth element of the Periodic Table is widely known in its 3D forms, namely diamond and graphite. The former consists chemically of the carbon atoms arranged in a tetrahedral structure such that the necessary energy for exciting a $2s$ electron into a $2p$ state (electronic configuration $2s^1 2p^3$) becomes compensated by the bonding of the sp^3-hybridized orbitals, which makes a very robust, strong insulator. The graphene structure keeps just three electrons from each single sp^2-hybridized atom thus forming σ-bonds in a plane, whereas a last electron in each atom remains in a single p orbital perpendicular to that plane (benzene structure), begetting π-bonds. A collection of many planes like that just described, with very strong in-plane bondings while stacked onto each other by weak van der Waals perpendicular forces, forms the structure of graphite. This structure explains why it is so useful as a lubricant or as an instrument for writing (see Fig. 1.1). In fact, when one writes on a paper with a pencil, thin layers from the tip become separated and attached to the paper. Among them, we may find single layers (one-atom-thick graphite planes) which are referred to as *graphene*. This term is used as well when just a few layers of graphite remain, keeping some 2D and graphene characteristics. Then we may speak of bilayer graphene, trilayer graphene, etc.

1.1.1 Graphene and other 2D materials on substrates

This isolation and observation of graphene [3] as a purely 2D atomic crystal and its electronic charge-conducting carriers inside [8, 9] was really unexpected from both the Peierls-Landau theory on its stability [10] and the lack of experimental tools to observe one-atom-thick membranes. Despite these pessimistic expectations, graphene was luckily spotted by a subtle optical effect stemming from the pencil debris on a SiO_2 substrate. At the beginning of the new graphene era, its isolation was easily accepted by the community

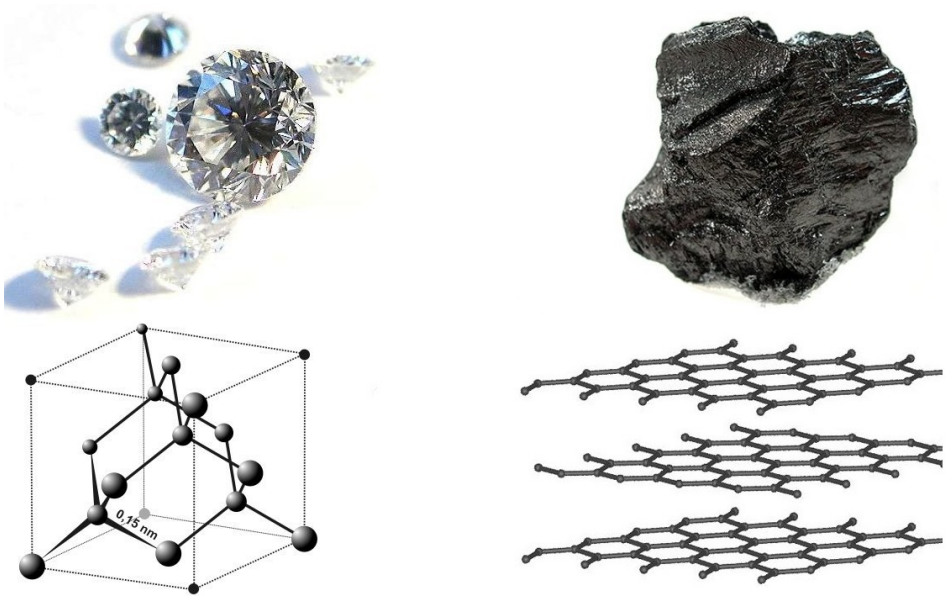

Figure 1.1: Carbon 3D structures. Left: diamond as macroscopically found (top) and its molecular tetrahedral structure (bottom). Right: same for graphite, showing a sample of three of its constituent graphene layers.

because graphene samples lied on the surface of a 3D bulk substrate or were embedded in a larger 3D structure. However, it was soon discovered that the support of a 3D substrate was not essential. In fact, freely suspended graphene membranes were fabricated and well characterized [11]. These samples were not totally flat due to out-of-plane deformations as high as 1 nm.

After years of predominance of the graphene paradigm, this topic of research has been extended to the large and growing family of many other single- or few-layer materials holding 2D electronic systems, with many different electronic properties among them, ranging from conductors (e.g. $NbSe_2$) to semiconductors (e.g. MoS_2) and insulators (e.g. hBN, for hexagonal boron nitride). The different mechanical, chemical and electronic properties of this new type of materials provide a wealth of research opportunities. They can be isolated or combined with the same van der Waals forces

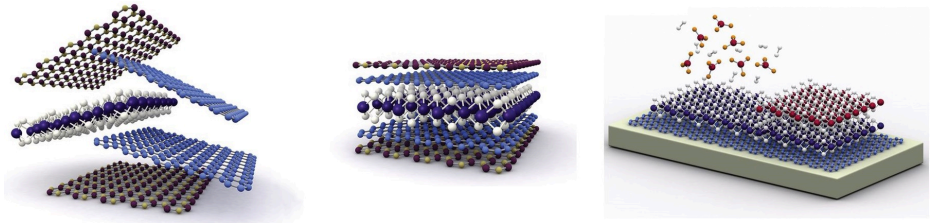

Figure 1.2: Two-dimensional (2D) materials and van der Waals heterostructures. Left: combination of different 2D materials by mechanically sandwich-assembling them. Center: van der Waals heterostructure already assembled. Right: the same heterostructure while being grown onto a substrate by techniques such as chemical vapor deposition (CVD) or physical-epitaxy technology. Taken from Ref. [12].

which bind graphene layers into graphite, raising new questions for further research and technological applications (see Fig. 1.2).

Regarding suspended 2D materials such as graphene, they are usually disordered and their quality and characteristics are poorer than expected in substrates like SiO_2. Whereas some improvements are caused by the aforementioned suspension in free space [13] (only at low temperatures due to the intrinsic flexural phonons [14]), that geometry imposes severe limitations regarding device funcionality and architecture. It is then essential for the future technological progress to get suspended-like sample qualities by placing the 2D material onto a proper substrate. In the case of graphene, it seems that hBN, as an isomorph of graphite with boron and nitrogen occupying the alternate positions of their periodic-table neighbor C, has produced the best results from the very beginning, in contexts where high mobilities and large carrier density homogeneities are requested [15, 16].

For the sake of completeness, the very basic and needed electronic properties of graphene are reviewed too and all the details are left to the App. A, an important part of the main material to be studied in this thesis.

1.2 The piezoelectric effect. Some history and basic phenomenology.

The *piezoelectric effect* is another key ingredient of the present work. As in the case of graphene and for completeness, we present here a short review of its essentials, leaving the technical parts to the Apps. B and C for those readers who are not familiarized with the topic.

Piezoelectricity can be defined as a "linear interaction between mechanical and electrical systems in non-centric crystals or similar structures" [17], see Fig. 1.3(a). It is thus mathematically stated as a proportional relation between the electric displacement vector $\mathbf{D}$ and the strain tensor $\hat{u}$ via a third-rank tensor, the piezoelectric tensor $\hat{e}$. Equivalently, and with different proportionality constants, one may use the stress tensor $\hat{T}$ for the mechanical degrees of freedom. The magnitude $\hat{e}$ has physical dimensions of polarization, that is, charge per unit area (if the stress tensor is used instead of the strain to establish the proportionality law, the other resulting piezoelectric tensor $\hat{d}$ has units of charge divided by force).

This common and useful effect was discovered by the brothers Pierre and Jacques Curie in 1880 from their work on pyroelectricity (an effect analogous to piezoelectricity, but relating the polarization to temperature instead of strain), which was discovered in tourmaline 23 centuries ago by Theophrastus, who observed the electrical charge in this material when he heated it. The French brothers realized that some crystals became polarized when they were macroscopically deformed in some directions, in contrast to others, making piezoelectricity a strongly anisotropic effect and very related to symmetry in crystals. Some months later, Gabriel Lippmann predicted successfully the *converse piezoelectric effect* in the same crystals, that is, the deformation of a piezoelectric crystal when placed inside electric fields [see Fig. 1.3(b)]. In 1888 and after the discovery of the piezoelectric effect in quartz, they proposed it as an instrument in metrology. This effect in quartz was used by Marie Curie later to measure radioactivity, achieving the Nobel Prize in Chemistry in 1911.

In general, the study piezoelectricity is rather multidisciplinary. Its research and development requires knowledge of tensor calculus, elasticity theory, crystallography, as well as thermodynamics. Moreover, the experimental work requires the cooperation of physicists, chemists and engineers. Its study can be addressed within a macroscopic (phenomenological) framework (as in App. B) or a microscopic (atomistic) one (as in App. C), both being necessary for a comprehensive understanding.

The first big treatise about piezoelectricity using the physics of crystals and their symmetry was completed by Voigt more than 100 years ago (we owe him the famous "Voigt notation" in terms of some tensors), who used some thermodynamic potentials for the study, based in the principles formulated by Lord Kelvin. Later, towering figures such as Ginzburg appeared in the field and applied the Landau theory to the thermodynamics of piezoelectrics (and ferroelectrics). Even Schrödinger and Born tried to use an atomic aproach in order to explain piezoelectric properties of quartz. We may also mention Bragg and Gibbs, who used X-ray methods for some qualitative explanations [17]. Piezoelectricity has even been suggested as a mechanism for the functioning of biological systems, first done by Pasteur about 100 years ago.

The ubiquitous applications of piezoelectricity in scientific and technological fields were discussed at major conferences from the very beginning by physicists as well-known as the aforementioned ones. For example, Paul Langevin invented sonars due to his activity on the emission and detection of underwater sound waves. Piezoelectric devices are nowadays used in all kind of circuitry in sensors, watches, microphones, speakers, medical diagnosis, vecell phones, computer memories... as outlined in Fig. 1.3(c), where a list of piezoelectricity-based applications is given.

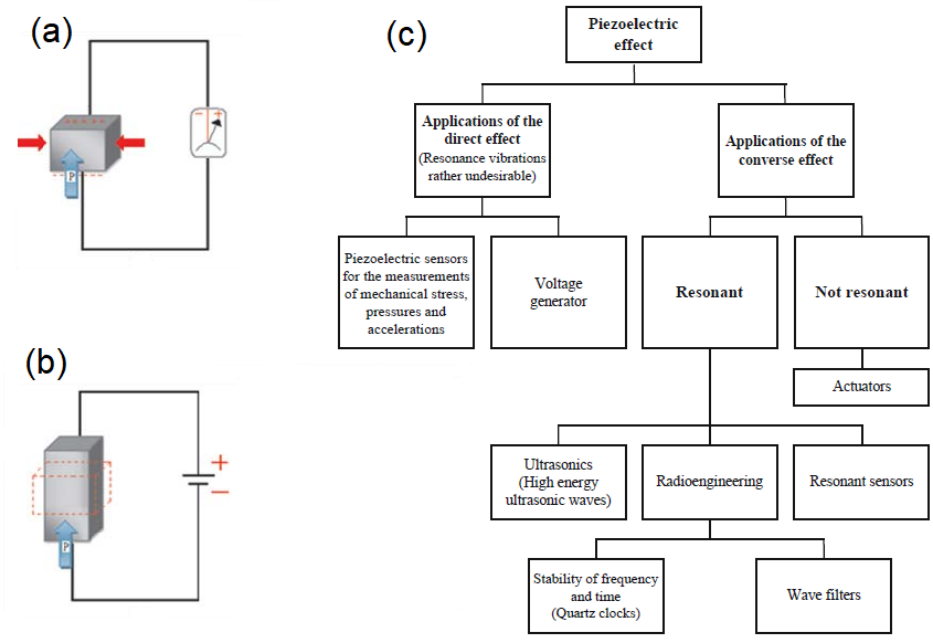

Figure 1.3: Schematics of the piezoelectric effect. (a) Sketch of the direct effect: the pressure/strain applied to a piezoelectric material produces a measurable voltage. (b) The converse piezoelectric effect: now the electric field applied to the body causes its deformation. (c) Summary of the technical applications of piezoelectricity, as taken from Ref. [17].

1.3 Elastic waves in crystals

As P. G. de Gennes (Nobel Prize in Physics 1991) writes in the foreword of Refs. [18, 19]: "The story of elastic waves is fascinating, from the very early mechanical aspects -well covered in *The theory of solids* by Lord Rayleigh- right up to the quantum behavior, initiated by Einstein and Debye early in the 20th century.".

Elastic waves are mechanical vibrations that propagate in gases, liquids and solids. Our topic of surface acoustic waves in piezoelectrics requires the previous knowledge of the general subject of elastic (non-piezoelectric) crystals, which have their own elastic waves in the bulk (as reviewed in

App. D) and at the surface (mostly detailed in App. E). These purely elastic waves have properties related to those in piezoelectric materials. In general, however, the term "SAW" is used for elastic waves occuring at the surface of a piezoelectric crystal, specifically those of the Rayleigh type (there are others types of waves, as will be seen), which lie at the basis of many electronic devices.

1.3.1 Surface acoustic waves in piezoelectrics

In general, there are many scenarios of non-infinite media carrying acoustic waves in the literature. The boundaries of such a finite medium impose additional conditions in the wave equations to be satisfied, and they can change the type of wave by reflections and transmissions, including the possibility to build mechanical waveguides by confining them in some concrete parts of the solid.

But the main kind of waves to be studied in this work are those taking place at the surface of a crystal in vacuum. The most important waves in this scenario are called *Rayleigh waves* (see Fig. 1.4) and their details are discussed in App. E for isotropic solids before turning to the more anisotropic crystals (in App. F for the bulk, and in Ch. 2 for the surface). While the former admit relatively easy analytical solutions, the latter cases must be usually solved just by numerical methods.

Apart from their intrinsic theoretical interest, isotropic elastic waves have also many features in common with the solutions for anisotropic materials, as is the case with bulk waves. After a proper understanding of waves in purely elastic materials without any piezoelectric effects, one must turn to the more general and complicated case of crystals with both anisotropic elastic and piezoelectric properties, where the mechanical stresses and strains are coupled to electric fields.

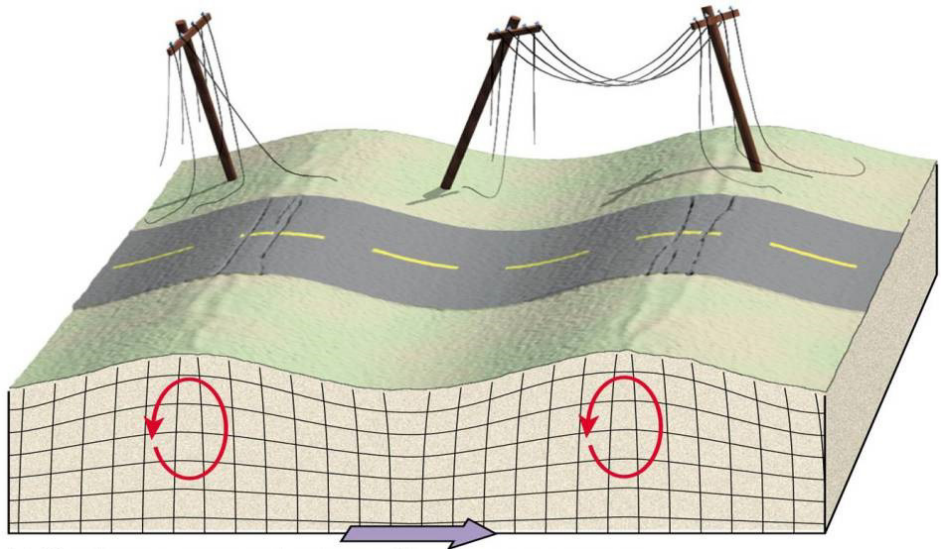

Figure 1.4: Sketch of a Rayleigh wave at the surface of a semi-infinite medium. Just after their discovery, they became important for geophysicists because, as pointed out by Lord Rayleigh: "...play an important part in earthquakes... diverging in two dimensions only, they must acquire at a great distance from the source a continually increased preponderance..." [20, 21].

1.3.2 Generation of SAWs and main applications

After the first decades of applications of piezoelectrics and acoustic waves in the bulk, the 1960s gave rise to the common usage of SAWs in many fields of electronics, with many different compact and inexpensive signal-processing components, yielding big size savings of the order of 10^5 (the ratio of the light velocity to the sound velocity). In contrast to bulk waves, surface waves are always accesible for this goal [22].

The first proposals for ultrasonic surface-wave generation consisted of a wedge arrangement [24], which converted a homogeneous plane wave sup-

(a)

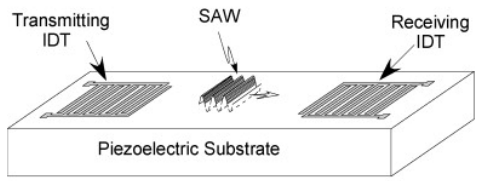

(b)

Device	Applications
Delay line	Oscillator, monopulse radar, electronic countermeasures (repeaters), sensors
Tapped delay line (fixed or programmable)	PSK correlation in communications
Tapped delay line, reflective	Sensors (temperature, pressure, chemicals), identity tags
Resonator (one or two port)	Oscillator, sensors
Chirp filter (interdigital or RAC)	Radar pulse compression and expansion, spectral analysis, Fourier analysis, variable delay
Bandpass filter, transversal	Domestic TV receiver, TV equipment, general communications and radar, PSK–MSK conversion, cordless phones, pagers, clock recovery (in fiber-optic repeaters), clutter filters for radar
Bandpass filter bank	Electronic surveillance
Low-loss bandpass filter[a] (IEF or LCR filter)	RF front end filtering[b]
Low-loss bandpass filter[a] (TCR filter)	Narrow-band IF filtering[b]
Low-loss bandpass filter (SPUDT)	IF filtering[b, c]

[a] Resonator filter.
[b] Including mobile phone handset.
[c] Including mobile phone basestation.

Figure 1.5: SAW devices and applications. (a) Sketch of the elementary SAW device with two transducers, one for generation and the other for reception. (b) Summary of the main surface-wave devices and their applications, as taken from Ref. [23].

ported by the wedge into a surface wave along the interface region under it. Then, the *interdigital transducer* (IDT) appeared, opening the possibility to generate propagating surface waves in the gigahertz-frequency range [25, 26] and allowing to borrow all the lithographic techniques from semiconductor manufacture for their developement. IDTs consist essentially in comb-shaped electrodes photoetched onto a piezoelectric substrate [see Fig. 1.5(a)] that can convert a sinusoidal voltage applied on it into a propagating SAW and vice versa, that is, to receive a SAW signal and convert

it into an electric pulse (provided that the frequency of the signal matches the proper sound wavelength imposed in the geometry of the electrodes, see Refs. [19, 23] for further information on their operation).

After the discovery of the IDT, all kind of SAW devices with different applications were developed and integrated in many different instruments such as TVs and cell phones, as outlined in Fig.1.5(b). Billions of SAW devices are produced every year this way. As early as in 1977, Williamson [27] pointed out 44 different SAW devices and 45 government systems using them.

1.3.3 SAWs and two-dimensional electron systems

In addition to their general applications, coherent SAWs generated on piezoelectric substrates have also many applications both for nanoscale electronic devices and for the theoretical and experimental physics in the field of low-dimensional systems by probing their electronic properties. For example, in the topic of graphene and its related 2D van der Waals materials.

Especially important is the well-known equation, derived elsewhere [28, 29]:

$$\frac{\Delta v_s}{v_s} - i\frac{\kappa}{q} = \frac{K^2/2}{1 + i\sigma_{xx}/\sigma_m} \ , \tag{1.3.1}$$

relating the SAW-velocity change Δv_s, the SAW-attenuation coefficient κ and the longitudinal electronic conductivity in a 2D electronic sample σ_{xx}, as functions of the chemical potential, temperature and/or magnetic field (with K and σ_m being constants depending on the geometry and the intrinsic properties of the piezoelectric substrate where the SAW is generated). The interaction of these coherent waves have measured this way the Shubnikov-de Haas oscillations many decades ago in classical quasi-2D electronic systems in GaAs/Al_xGa_{1-x}As heterostructures [30] and more recently in graphene [31].

On the other hand, since the first theoretical prediction of the classical *acoustoelectric effect* [32] (generation of a non-linear-coupled electric current

from an acoustic wave) in the bulk and its subsequent experimental observation [33], this effect was probed as well in the context of SAWs in classical 2D electronic systems [30, 34], and lately in graphene sheets [35, 36] and graphene nanoribbons [37]. These studies in 2D have also suggested important applications of SAWs for metrology and quantum computation in the single-electron regime, both in classical 2D electronic systems [38, 39] and with related technologies in graphene [40]. Even in the fields of chemical sensors [41] and plasmonics [42], SAWs have generated interest in the study of their coupling with charge carriers living in two dimensions.

Chapter 2

Piezoelectric surface acoustic waves

2.1 Reformulation of the surface-acoustic-wave problem with piezoelectricity

Appendix E is dedicated entirely to analytical methods to find elastic waves confined to surfaces from the solutions in the bulk, where exact analytical solutions for Rayleigh waves were given in isotropic, non-piezoelectric scenarios. The introduction of anisotropy requires the use of numerical methods to find the analogous solutions from those in the bulk, albeit a related method to solve the wave equation is used.

First, we note that a general solution in the surface cannot be guaranteed to exist [43], but there seems to be no practical conditions where they actually do not exist, especially with the proven bound (given below) for the electromechanical coupling constant $K_R^2 < 1$, with $K_R^2 \sim e^2/\varepsilon c$. An inspection of the literature theorems (see e.g. Refs. [43, 44, 45]) assures existence for all anisotropic, non-piezoelectric media, unless in very exceptional cases where the bulk waves directly satisfy the boundary conditions. This guarantees an almost-general solution for piezoelectric SAWs with metal-cover

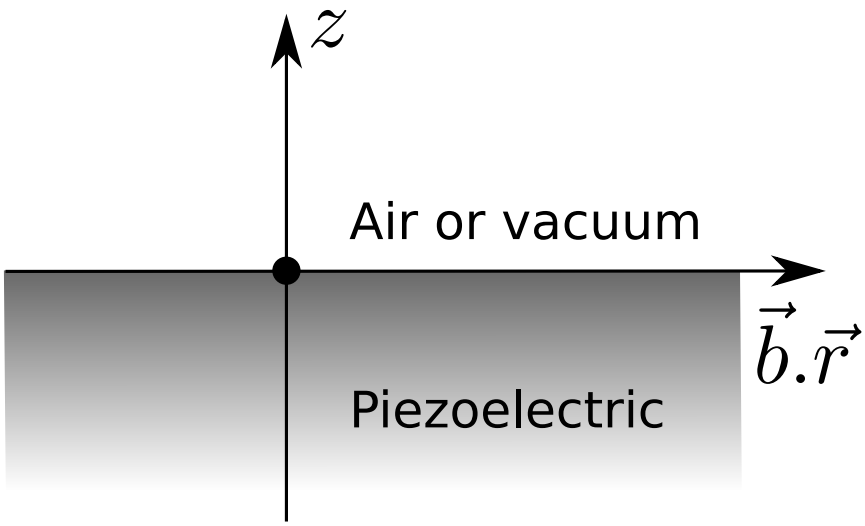

Figure 2.1: A flat piezoelectric substrate with an interface to air or vacuum, with $\mathbf{b} = [\cos(\theta), \sin(\theta)]$ the propagation direction of the piezoelectric SAW.

(zero electric field) boundary conditions (see below), but this result cannot be extended to the free-surface piezoelectric case, except for the smallest piezoelectric-tensor values.

The situation is schematically depicted in Fig. 2.1. The $\{x_3 \equiv z = 0\}$ surface is supposed to be free of tension and, when acting as a substrate to a deposited 2D electronic material sheet, free of electrodes as well. In further sections below, flat electrodes (at $z = 0^+$), which supply no mechanical stresses, will be allowed.

The SAWs are solutions to the equations derived in Apps. D, F for the displacements u_1, u_2, u_3 [see Eqs. (F.1.1)]:

$$\begin{aligned} \rho\ddot{u}_i &= c_{ijkl}\frac{\partial^2 u_k}{\partial x_j \partial x_l} + e_{kij}\frac{\partial^2 \varphi}{\partial x_j \partial x_k} \ , \quad i = 1, 2, 3 \ , \\ 0 &= \varepsilon_{jk}\frac{\partial^2 \varphi}{\partial x_j \partial x_k} - e_{jkl}\frac{\partial^2 u_k}{\partial x_j \partial x_l} \ , \end{aligned} \tag{2.1.1}$$

where c_{ijkl} are the components of the elastic tensor, e_{jkl} are the components of the piezoelectric tensor, and ε_{jk} are the components of the dielectric

tensor. The Einstein summation convention of repeated indices is used.

These solutions have the form of plane waves propagating along and localized near the surface $z = 0$ in the direction specified by the unit vector $\mathbf{b} = [\cos\theta, \sin\theta]$, that is:

$$\begin{aligned} u_j &= A_j \exp[ik(b_i x_i - vt)] \ , \\ \varphi &= A_4 \exp[ik(b_i x_i - vt)] \ , \end{aligned} \tag{2.1.2}$$

where the definition of $\mathbf{b} := [\cos(\theta), \sin(\theta), b_3]$ has been extended here to three dimensions, so that b_3 is now a complex variable to be determined by the requirements of boundedness or causality of normal modes (see below). In what follows, $v > 0$ and $k > 0$ is always assumed, and the dielectric tensor $\hat{\varepsilon}$ is taken relative to vacuum. In that case, the resulting Christoffel equations for the amplitudes A_a (here $a, b = 1, 2, 3, 4$ and $i, j, k, l = 1, 2, 3$) read

$$0 = \left(\Gamma_{ab} - \delta'_{ab}\rho v^2\right) A_a \ , \tag{2.1.3}$$

with Γ_{ab} defined as

$$\begin{aligned} \Gamma_{jk} &= b_i b_l c_{ijkl} \ , \\ \Gamma_{j4} &= b_i b_k e_{ijk} \ , \\ \Gamma_{44} &= -b_i b_k \varepsilon_{ik}\varepsilon_{\text{vac}} \ , \end{aligned} \tag{2.1.4}$$

where $\delta'_{ij} = \delta_{ij}$, $\delta'_{4a} = \delta'_{a4} = 0$, and ρ is the constant density of the piezoelectric solid.

Note that the modulus k disappears, which means that there is no dispersion for a given propagating direction. Hence, given the propagation direction θ and the velocity v, the solutions for $\det\left(\Gamma_{ab} - \delta'_{ab}\rho v^2\right) = 0$ as a function of b_3 is a set of no more than 8 complex values, in which, because of the reality of the coefficients, each complex root comes together with its conjugate, and among these, one must choose the ones with $\operatorname{Im} b_3 < 0$, so that the modes are not exponentially growing deep into the solid. In the

case of purely real solutions, usual arguments on causality demand that one has to take only those modes with radiation (outgoing from the surface $z = 0$) boundary conditions $db_3(v)/dv < 0$ (see Ref. [46]). Hence, the total number of allowed modes is 4, and the general solution is written as the sum [we use now $u_4 := \varphi$ and write $\mathbf{r} = (\mathbf{R}, z)$, with the 2D position vector $\mathbf{R} = (x, y)$]:

$$u_a(\mathbf{r}, t) = C_n A_a^{(n)} e^{ikb_3^{(n)} z} \exp\left[ik(\mathbf{b} \cdot \mathbf{R} - vt)\right] \ , \tag{2.1.5}$$

with $n = 1, 2, 3, 4$ indexing the normal modes.

Much simpler is the equation at vacuum/air. The solution is purely electric and can be written as:

$$\varphi(\mathbf{R}, z, t) = u_4(\mathbf{R}, 0, t) e^{-kz} \ , \tag{2.1.6}$$

because of the continuity of the potential.

Cut terminology

A convention to specify the direction of the surface and the wave propagation with respect to the crystal is needed to define unambiguously the problem. The direction x_3 perpendicular and pointing outwardly to the surface is called the cut. For example, "Z-Cut zinc oxide" means that a ZnO crystal is bounded with a surface perpendicular to its Z-axis. The axis cut can be followed by the propagation direction, so that "Z-X zinc oxide" would mean a wave vector parallel to the X-axis of the crystal in the previous cut.

2.1.1 Boundary conditions

The mechanical boundary conditions are the same as in Eq. (E.1.2) for a free-surface, that is, $T_{i3}(\mathbf{R}, 0, t) = 0$ for $i = 1, 2, 3$. This leads to:

$$C_n b_k^{(n)} (A_j^{(n)} c_{3ijk} + A_4^{(n)} e_{k3i}) = 0 \ , \tag{2.1.7}$$

where $\mathbf{b}^{(n)} := \left[\cos(\theta), \sin(\theta), b_3^{(n)}\right]$, hence C_i are proportional to C_4.

These conditions are to be supplemented now with an electric boundary condition, for which we will consider two main possibilities in this problem. If the surface is free, the continuity of the normal component of the electric displacement D_3 in the surface is imposed, since there are no free charges:

$$D_3(\mathbf{R}, 0^-, t) = k\,\varphi(\mathbf{R}, 0^+, t)\,\varepsilon_{\text{vac}} \ . \tag{2.1.8}$$

The second possibility applies when the boundary is covered by a thin metal layer with perfect conductivity. Then, the electric field drops to 0 at the surface without modification of the mechanical conditions, which means:

$$\varphi(\mathbf{R}, 0, t) = 0 \ . \tag{2.1.9}$$

These two typical conditions give different solutions with different velocities. The difference between both wave velocities is a measure of the coupling of the electric and mechanical fields, as pointed out in the App. F.2 regarding the piezoelectric stiffening.

2.2 Typical approximations

For the sake of completeness and to make connection with the existing literature about these surface waves and the theoretical derivations of the interactions, some sections regarding the typical approximations made in these systems are attached, justifying why they work so well with the prototypical case of GaAs. This ubiquitous piezoelectric material is explored as an example.

2.2.1 Isotropic approximation for weak piezoelectricity

Even though the most common definition for a piezoelectric tensor in the literature of elasticity and piezoelectricity (usually engineer-oriented) is that

which we have given for e_{ijk} in SI units of $\mathrm{C/m^2}$ with [23]

$$\begin{aligned} D_i &= \varepsilon_{ij}\varepsilon_{\mathrm{vac}} E_j + e_{ijk} u_{jk} \\ &= -\varepsilon_{ij}\varepsilon_{\mathrm{vac}} \frac{\partial \varphi}{\partial x_j} + \frac{1}{2} e_{ijk} \left(\frac{\partial u_j}{\partial x_k} + \frac{\partial u_k}{\partial x_j} \right) , \end{aligned} \tag{2.2.1}$$

this same phenomenon is sometimes described in c.g.s. units, with the electric displacement $\mathbf{D}$ in such material, given as $\mathbf{D} = \varepsilon_0(4\pi\mathbf{P} - \nabla\varphi)$. In c.g.s language, the polarization vector is $\mathbf{P} = P_i = \beta_{ijk} u_{jk}$, where $\hat{\beta} = \beta_{ijk}$ is the *tensor of piezoelectric moduli* [47, 48, 49, 50], and here ε_0 is the adimensional, relative dielectric constant of the material (1 in vacuum).

In a general material, in the case of certain symmetries and the choice of some specific coordinate axes, as in Sec. C.2, the piezoelectric tensors reduce to a number, i.e., all the terms β_{ijk} being 0 except for ijk all different. This occurs, for example, with the cubic structure of gallium arsenide choosing its inner latice axis to be X-Y-Z for the problem, where $\beta = 2.4 \times 10^7\ \mathrm{V/cm}$ in the former description [49]; and the dielectric tensor is a scalar, with $\varepsilon_{ij} \equiv \varepsilon_0 = 12.8$. In the Voigt notation:

$$\begin{pmatrix} P_x \\ P_y \\ P_z \end{pmatrix} = \begin{pmatrix} 0 & 0 & 0 & \frac{\beta}{8\pi} & 0 & 0 \\ 0 & 0 & 0 & 0 & \frac{\beta}{8\pi} & 0 \\ 0 & 0 & 0 & 0 & 0 & \frac{\beta}{8\pi} \end{pmatrix} \begin{pmatrix} u_{xx} \\ u_{yy} \\ u_{zz} \\ 2u_{yz} \\ 2u_{xz} \\ 2u_{xy} \end{pmatrix}_{\text{(cgs)}} , \tag{2.2.2}$$

which is equivalent to the former description in Eq. (2.2.1):

$$\begin{pmatrix} D_x \\ D_y \\ D_z \end{pmatrix} = \begin{pmatrix} \varepsilon_0\varepsilon_{\rm vac} & 0 & 0 \\ 0 & \varepsilon_0\varepsilon_{\rm vac} & 0 \\ 0 & 0 & \varepsilon_0\varepsilon_{\rm vac} \end{pmatrix} \begin{pmatrix} E_x \\ E_y \\ E_z \end{pmatrix} + \\ + \begin{pmatrix} 0 & 0 & 0 & e_{14} & 0 & 0 \\ 0 & 0 & 0 & 0 & e_{14} & 0 \\ 0 & 0 & 0 & 0 & 0 & e_{14} \end{pmatrix} \begin{pmatrix} u_{xx} \\ u_{yy} \\ u_{zz} \\ 2u_{yz} \\ 2u_{xz} \\ 2u_{xy} \end{pmatrix}_{\rm (SI)} . \qquad (2.2.3)$$

Eq. (2.2.2) is equivalent to $P_x = \frac{\beta}{4\pi}u_{yz}, P_y = \frac{\beta}{4\pi}u_{xz}, P_z = \frac{\beta}{4\pi}u_{xy}$ and Eq. (2.2.3) to $D_x = \varepsilon_0\varepsilon_{\rm vac}E_x + 2e_{14}u_{yz}, D_y = \varepsilon_0\varepsilon_{\rm vac}E_y + 2e_{14}u_{xz}, D_z = \varepsilon_0\varepsilon_{\rm vac}E_z + 2e_{14}u_{xy}$. Therefore, both descriptions are related by $\beta \equiv 2e_{14}/\varepsilon_0$.

In App. D, dealing with an isotropic [i.e., a cubic material with $2c_{44} = c_{11} - c_{12}$, see Eq. (D.3.1)], non-piezoelectric ($\hat{e} = 0$) material, Rayleigh solutions were given in terms of the longitudinal $\partial^2\mathbf{u}_l/\partial t^2 = v_l^2\Delta\mathbf{u}_l$ and transversal $\partial^2\mathbf{u}_t/\partial t^2 = v_t^2\Delta\mathbf{u}_t$. The solution was:

$$\mathbf{u}_\mathbf{q}(\mathbf{r}, t) = C_\mathbf{q}\exp[i(\mathbf{q}\cdot\mathbf{R} - \omega_\mathbf{q}t)]\mathbf{v}_\mathbf{q}(z) + \text{c.c.} \qquad (2.2.4)$$

for 3D $\mathbf{r} = (x, y, z)$ and 2D $\mathbf{R} = (x, y)$, with elliptic polarization:

$$\mathbf{v}_\mathbf{q}(z) = -i\hat{\mathbf{q}}\,(e^{\kappa_l qz} - f\kappa_t e^{\kappa_t qz}) + \hat{\mathbf{z}}\,(\kappa_l e^{\kappa_l qz} - f e^{\kappa_t qz}) \ , \qquad (2.2.5)$$

provided that $\hat{\mathbf{q}} = \mathbf{q}/q$, $\hat{\mathbf{z}} = \hat{\mathbf{n}}$ are the proper unit vectors, $\kappa_l(\alpha) = \sqrt{1 - \alpha\zeta^2}$, $\kappa_t(\alpha) = \sqrt{1 - \zeta^2}$, $\alpha = v_t^2/v_l^2$, $\omega_\mathbf{q} = \zeta v_t q = v_s q$, $f(\alpha) = \sqrt{\kappa_l/\kappa_t}$ and ζ is the solution of a sixth order equation containing just the parameter α, which determines the sound velocity of the Rayleigh modes v_s [51, 49], as discussed after Eq. (E.1.3).

When the material is in addition a piezoelectric crystal, the previous Rayleigh solution to the surface-wave equation is not exact, because it ne-

glects the coupling term $e_{ijk}\,\partial^2\varphi/\partial x_j\partial x_k$ between displacement and electric fields as well as possible anisotropies among the elastic terms. From the Poisson equation $\nabla\cdot(-\hat{\varepsilon}\nabla\varphi+\hat{e}\mathbf{u})=0$, one gets that $\varphi\sim\frac{\hat{e}\mathbf{u}}{\varepsilon}$, and this term $e_{ijk}\,\partial^2\varphi/\partial x_j\partial x_k$ is then of the order of $\sim\frac{\hat{e}^2}{\hat{\varepsilon}\hat{c}}c_{ijkl}\frac{\partial u_{kl}}{\partial x_j}$. Here, the important number $K^2=\frac{\hat{e}^2}{\hat{\varepsilon}\hat{c}}$ plays the role of the electromechanical coupling coefficient (discussed in App. F.2). In the case of K^2 of 1% or less, it is reasonable to neglect the electric term $e_{ijk}\,\partial^2\varphi/\partial x_j\partial x_k$ for the wave equation, assuming a very small error in this way.

In this common example of GaAs, it is $\beta=2.4\times10^7\,\mathrm{V/cm}$ or $e_{14}=0.16\,\mathrm{C/m^2}$, though there is a considerable uncertainty among the measurements of this quantity [29]. On the other hand, $c_{11}=12.26\times10^8\,\mathrm{N/m^2}, c_{12}=5.71\times10^8\,\mathrm{N/m^2}, c_{44}=6.00\times10^8\,\mathrm{N/m^2}, \rho=5307\,\mathrm{Kg/m^3}$, and $K^2<0.01$ so that the previous reasoning applies to neglect the terms with $\hat{e}^2/\varepsilon$ in comparison with the much bigger elastic terms with $\hat{c}$, which are 2 or 3 orders of magnitude bigger. On top of it, the anisotropy ratio is 1.8, so the isotropic approximation for the purely elastic wave serves as a good first approximation.

In that case, one considers the "bare" approximate elastic Rayleigh displacement fields as the solution of the first three Eqs. (F.1.1), so that the electric field $\varphi_{\mathbf{q}}(\mathbf{r},t)$ is solved from the Poisson equation and the appropiate boundary conditions [49, 50] (free surface in this case):

$$[\partial_z^2-q^2]\varphi_{\mathbf{q}}(\mathbf{r},t)=C_{\mathbf{q}}\beta q_x q_y e^{i\omega_{\mathbf{q}}t}[-3\kappa_l e^{\kappa_l qz}+f(1+2\kappa_t^2)e^{\kappa_t qz}]\;, \tag{2.2.6}$$

$$4\pi\varepsilon_0 P_z-\varepsilon_0\partial_z\varphi_{\mathbf{q}}(z\to0^-)=-\varepsilon_0\partial_z\varphi_{\mathbf{q}}(z\to0^+)\;, \tag{2.2.7}$$

$$\partial_{\mathbf{r}}\varphi_{\mathbf{q}}(z\to0^-)=\partial_{\mathbf{r}}\varphi_{\mathbf{q}}(z\to0^+)\;, \tag{2.2.8}$$

and then, after some straightforward algebra:

$$\begin{aligned}\varphi_{\mathbf{q}}(\mathbf{r},t)=&C_{\mathbf{q}}\zeta^{-2}\frac{q_xq_y}{q^2}\beta\exp\left[i(\mathbf{q}\cdot\mathbf{R}-\omega_{\mathbf{q}}t)\right]\\&\times[3\kappa_l\alpha^{-1}e^{\kappa_l qz}-f(1+2\kappa_t^2)e^{\kappa_t qz}+Ce^{qz}]\;,\end{aligned} \tag{2.2.9}$$

with $C=(\varepsilon_0+1)^{-1}[-3\kappa_l\alpha^{-1}(1+\kappa_l\varepsilon_0)+f(1+2\kappa_t^2)(1+\kappa_t\varepsilon_0)-\varepsilon_0\zeta^2(1-f\kappa_t)]$,

and finally solving the problem of the displacements and the electric field analytically within a good approximation.

2.2.2 Perturbative treatment

The former problem for the purely elastic wave can also be solved approximately without assuming isotropy, taking into account the anisotropic nature of the elastic tensor. The piezoelectricity remains neglected provided that the electromechanical factors are still small enough.

In that case, whereas the general problem must be solved numerically with the formalism in App. D.2 with the appropiate boundary conditions in the interface, there are some cases in high-symmetry directions or specific materials that admit a very accurate analytical treatment. For example, many different cases in cubic (and some non-cubic) materials and their trends are discussed in Refs. [18, 21]. Unfortunately, since there are so many different scenarios, surface cuts and propagation directions among crystals, it is impossible to derive general formulas for all those cases.

For example, in the studied case of GaAs (or any cubic crystal), the whole equations for the three spatial and the electrical degrees of freedom read exactly:

$$\begin{aligned}\rho\partial_t^2 u_x = {} & c_{11}\partial_x^2 u_x + c_{44}[\partial_y^2 u_x + \partial_z^2 u_x] + (c_{11}+c_{44})[\partial_x\partial_y u_y + \partial_x\partial_z u_z] \\ & + 2e_{14}\partial_y\partial_z\varphi \ , \end{aligned} \tag{2.2.10}$$

$$\varepsilon_0\varepsilon_{\text{vac}}\Delta\varphi = 2e_{14}[\partial_y\partial_z u_x + \partial_x\partial_z u_y + \partial_x\partial_y u_z] \ . \tag{2.2.11}$$

Equation (2.2.10) actually represents three equations, with $\rho\partial_t^2 u_y$ and $\rho\partial_t^2 u_z$ obtained from cyclic permutations of (2.2.10).

The boundary conditions for the free surface at $z = 0$ are:

$$\begin{aligned} T_{13} &= c_{44}(\partial_x u_z + \partial_z u_x) + e_{14}\partial_y\varphi = 0 \ , \\ T_{23} &= c_{44}(\partial_y u_z + \partial_z u_y) + e_{14}\partial_x\varphi = 0 \ , \\ T_{33} &= c_{11}\partial_z u_z + c_{12}(\partial_x u_x + \partial_y u_y) = 0 \ , \\ D_z(0^-) - D_z(0^+) &= [e_{14}(\partial_y u_x + \partial_x u_y) - \varepsilon_0\varepsilon_{\rm vac}\partial_z\varphi + \varepsilon_{\rm vac}k\varphi]_{z=0} = 0 \ . \end{aligned} \tag{2.2.12}$$

The solution of both systems of equations simultaneously would provide an exact solution. In the justified case of the non-piezoelectric approximation $e_{14} \equiv 0$, one can take the solutions of the first system from the ansatz [52]:

$$\mathbf{u_q}(\mathbf{r}, t) = \mathbf{A}e^{-\Omega q z}e^{i(\mathbf{q}\cdot\mathbf{R}-\omega_\mathbf{q} t)} \ , \tag{2.2.13}$$

with given 2D wave vector $\mathbf{q}$ in the surface, and the frequency $\omega_\mathbf{q}$ remaining a parameter to give three complex solutions in Ω. Then, one varies the frequency till the combination of the three partial waves satisfy the second set of solutions of the boundary conditions.

In this example, taking $\mathbf{q} = q(1,1)/\sqrt{2}$, that is, propagation in the [110]-direction, and after some straightforward algebra [53, 29, 39], one finds that the equation for the boundary conditions is independent of Ω, numerically found from:

$$\left(1 - \frac{c_{11}}{c_{44}}X\right)\left(\frac{c_{11}c'_{11} - c_{12}^2}{c_{11}^2} - X\right)^2 = X^2\left(\frac{c'_{11}}{c_{11}} - X\right) \ , \tag{2.2.14}$$

with $c'_{11} = \frac{1}{2}(c_{11} + c_{12} + 2c_{44})$ and $X = \rho v_s^2/c_{11}$, giving the velocity in this direction by $v_s = \omega_{(1,1)}/q$ [here $\omega_{(1,1)}$ stands for $\omega_\mathbf{q}$ at $\mathbf{q} = q(1,1)/\sqrt{2}$]. Moreover, in this case of propagation direction, the three solutions of Ω in the ansatz are reduced to two complex-conjugate ones Ω, Ω^*, satisfying the quadratic equation, after choosing the proper sign of $\mathrm{Re}(\Omega)$ to avoid divergences at $z \to -\infty$ in the ansatz:

$$0 = \ (c'_{11} - Xc_{11} - \Omega^2 c_{11})(c_{44} - Xc_{11} - \Omega^2 c_{44}) + \Omega^2(c_{12} + c_{44})^2 \ , \tag{2.2.15}$$

and such that the solution for the global purely elastic problem in the surface lies again in the sagittal plane, as the isotropic Rayleigh waves do, but given analytically in the present case by:

$$\mathbf{u_q} \cdot \frac{1}{\sqrt{2}}(1,1,0) = C_{\mathbf{q}} \left(e^{-\Omega q z - i\phi} + e^{-\Omega^* q z + i\phi} \right) e^{i(\mathbf{q}\cdot\mathbf{R} - \omega_{(1,1)} t)} \ , \tag{2.2.16}$$

$$i\,\mathbf{u_q} \cdot (0,0,1) = C_{\mathbf{q}} \left(\gamma e^{-\Omega q z - i\phi} + \gamma^* e^{-\Omega^* q z + i\phi} \right) e^{i(\mathbf{q}\cdot\mathbf{R} - \omega_{(1,1)} t)} \ , \tag{2.2.17}$$

with

$$\gamma = \Omega \left[\frac{c_{12} + c_{44}}{c_{44} - (X + \Omega^2) c_{11}} \right], \quad e^{-2i\phi} = -\frac{\gamma^* - \Omega^*}{\gamma - \Omega} \ . \tag{2.2.18}$$

In general, and contrary to the isotropic case, the velocity (or frequency) now turns out to be direction dependent, and the decay to the bulk has both real and imaginary parts, so that the amplitude oscillates with depth. It is interesting to note from the solution how the bigger the anisotropic ratio [defined as $A := 2c_{44}/(c_{11} - c_{12})$] is, the slower the decay becomes (see Fig. 5.15 in Ref. [18] and App. D).

Finally, as in the previous section for the isotropic case, one assumes this solution for the mechanical fields in first order and plugs the displacement from Eq. (2.2.16) into the Poisson equation [Eq. (2.2.11)], obtaining the following expression for the electric field:

$$\varphi_{\mathbf{q}} = i C_{\mathbf{q}} \frac{e_{14}}{\varepsilon_0 \varepsilon_{\text{vac}}} \left(C_1 e^{-\Omega q z - i\phi} + C_2 e^{-\Omega^* q z + i\phi} + C_3 e^{q z} \right) e^{i(\mathbf{q}\cdot\mathbf{R} - \omega_{(1,1)} t)} \ ,$$

$$C_1 = C_2^* = \frac{\gamma - 2\Omega}{\Omega^2 - 1} \ , \tag{2.2.19}$$

with C_3 obtained from the boundary conditions:

$$C_3 = \frac{-2}{1 + \varepsilon_0^{-1}} \left[\cos\phi + \varepsilon_0^{-1} \mathrm{Re}(C_1 e^{-i\phi}) + \mathrm{Re}(\Omega C_1 e^{-i\phi}) \right] \ . \tag{2.2.20}$$

This solution is of course located inside the material, the electric field in the outside vacuum being much simpler. It is a harmonic function (the Poisson

equation here becomes the Laplace equation) given by:

$$\varphi_{\mathbf{q}} = \varphi_{\mathbf{q}}(0) e^{-qz} e^{i(\mathbf{q}\cdot\mathbf{R} - \omega_{(1,1)}t)} \ , \tag{2.2.21}$$

with an elementary decay law from its initial value, given by the boundary condition of the continuity of the potential. In this manner, this section illustrates with an example how this typical approximation method works.

2.2.3 Approximation using stiffened elastic constants

As pointed out after Eq. (F.2.3), in order to find the solution of bulk piezoelectric waves, it is possible to solve the problem in the bulk for a piezoelectric plane wave as in Eq. (F.2.1), exactly as if it were a non-piezoelectric anisotropic elastic wave as in Eq. (D.1.2). This becomes possible after a replacement is made of the actual elastic constants c_{ijkl} of the material by the effective ones:

$$c'_{ijkl} = c_{ijkl} + \frac{e_{mij} e_{nkl} k_m k_n}{\varepsilon_{mn} k_m k_n} \ , \tag{2.2.22}$$

once the wave vector $\mathbf{k} = (k_1, k_2, k_3)$ of the problem is given, and the solution being valid for any crystal and surface/wave vector orientation.

Unfortunately, it is impossible to get an exact solution in the case of surface acoustic waves by this method, since the given surface wave vector is 2D and the third component, k_3, is in general complex and can have many different values; except in very particular cases, e.g., the Bleustein-Gulyaev waves, to be studied below. There, one solves easily for the elastic terms, and it is enough to consider the wave equations without the piezoelectric term, just with a renormalized elastic constant $\tilde{c} = c + e^2/\varepsilon$ (in these very simple modes e, c, ε are constants and c is related to the sound velocity, $c = \rho v_s^2$) [54].

However, if one sets $k_3 \equiv 0$ as an approximation to obtain stiffened elastic constants as in Eq. (2.2.22), it is feasible to obtain an approximate solution of the surface-wave problem by just solving a purely elastic problem. Such an approximation would be exact for bulk waves in the crystal whose wave

vectors were parallel to the cut surface ($\mathbf{k}_3 = 0$).

For example, $LiNbO_3$ has piezoelectric parameters of order of $\hat{e} \sim 1\,\mathrm{C/m^2}$ and $\varepsilon \sim 40\varepsilon_{\mathrm{vac}}$, so that $K^2 \approx 0.027$, which is much larger than its GaAs counterpart. When the above approximation is used, lithium niobate is found to have velocities differing less than 3% from the experimentally observed ones. If the alternative (isotropic) approximation is made of taking $\hat{e} \equiv 0$ from the beginning, the estimated velocities are lower than the experimental ones by at least 15% [21, 55].

2.3 Exact solution

In the general case of piezoelectric materials, it is no longer suitable to neglect the e_{ijk} terms in the wave equation [Eq. (F.1.1)] for the problem at the surface. For example, the isotropic Rayleigh-wave approximation in the case of $LiNbO_3$ leads to surface-acoustic-wave velocities about 15% too low, as it was said in the previous section, and without the correct angular dependence [21, 23]. Moreover, we note that even some perovskites have $K^2 \sim 0.6 - 0.8$ in some directions.

2.3.1 General method

The general theory of the surface-wave solution with the proper boundary conditions is already developed in many references [23, 56, 18]. The solutions must be numerically found with the aid of the full elastic, dielectric and piezoelectric tensors, and the correct use of the direction of the cut in the substrate, which could make necessary an appropiate change of the coordinate basis.

Once the 2D direction $\mathbf{q}$ and the ansatz in Eq. (2.1.2) is established, the trial of a surface-wave velocity $v_s = \omega/q$ gives the general solution as a combination of partial waves, Eq. (2.1.5). This has to be done in the computer iterating in the unknown v_s till a combination of partial waves, satisfying

the system of wave equations, fulfills as well the boundary conditions stated in Sec. (2.1.1).

A computer is not able in general to solve the above problem exactly, but with an arbitrary finite accuracy for the velocity and the coefficients C_n in Eq. (2.1.5). While there is no dispersion on a given direction, the dependence on the velocity with the direction can range from highly non-trivial shapes to constant functions. The former case happens, for example, in $LiNbO_3$, whose velocities are shown in Fig. 2.2 as a funcion of direction in three canonical cuts and for a free surface. The latter case occurs, for example, with the trigonal wurtzites when they are cut with the Z-axis in the c-direction of their lattice pyramids (see Fig. C.1). The wave direction is symmetric enough to reduce as well the four general partial-wave solutions to three or even two as in the isotropic non-piezoelectric materials.

The *piezoelectric Rayleigh waves* are those solutions which have the lowest velocity. They are similar to the classical Rayleigh waves in isotropic materials, but show extra particular features, namely, the mentioned anisotropic velocity magnitude, the oscillatory decay (stemming from the nonzero real and imaginary parts of k_3), and the fact that the displacement is not confined to the sagittal plane, but usually has a nonzero component perpendicular to it. This last remark does not apply to the electric field since the electric potential is constant in the direction perpendicular to the saggital plane. These features make piezoelectric Rayleigh waves slightly different from isotropic Rayleigh waves.

There is another equivalent approach used to solve this problem exactly. It consists in evaluating the surface permittivity, as outlined below [18, 23, 28].

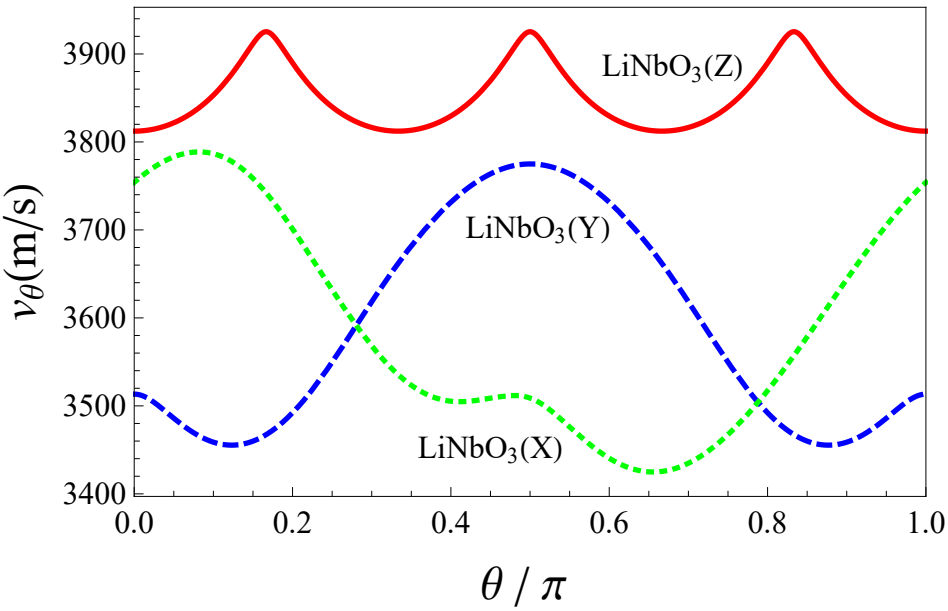

Figure 2.2: Calculated Rayleigh-wave velocities in the X,Y and Z-Cuts of $LiNbO_3$, in coincidence with the solutions found many years ago in Ref. [55]. For the Z-cut (Xcut/Y-cut), the zero angle corresponds to the x-axis (y-axis/z-axis) with the angle growing towards the y-axis (z-axis/x-axis), as in Ref. [2].

2.3.2 Surface permittivity

For any proposed velocity for the solution, the normal component of the electric displacement is, at the interface:

$$D_3(\mathbf{R}, 0^-, t) = ik \exp\left[ik(\mathbf{b}\cdot\mathbf{R} - vt)\right] C_n b_k^{(n)} (A_j^{(n)} e_{3jk} - A_4^{(n)} \varepsilon_{3k}\varepsilon_{\text{vac}}) \ , \tag{2.3.1}$$

and this allows to introduce the (relative) *piezoelectric surface permittivity* as the ratio [using the general solution Eq. (2.1.5)]:

$$\tilde{\varepsilon}(\mathbf{k}/\omega) := -\frac{D_3(\mathbf{R}, 0^-, t)}{k\varphi(\mathbf{R}, 0^-, t)\,\varepsilon_{\text{vac}}} = -i\frac{C_n b_k^{(n)} (A_j^{(n)} e_{3jk} - A_4^{(n)} \varepsilon_{3k})}{C_m A_4^{(m)}\,\varepsilon_{\text{vac}}} \ , \tag{2.3.2}$$

which depends on $v(\theta)$ and θ only through the relations $\mathbf{k} := k\mathbf{b}$ and $\omega := kv$.

Similarly, on the other side of the interface, this obvious relation holds:

$$1 = \frac{D_3(\mathbf{R}, 0^+, t)}{k\varphi(\mathbf{R}, 0^+, t)\,\varepsilon_{\text{vac}}} \ . \tag{2.3.3}$$

Hence, the surface charge at the interface can be expressed as the difference of the electric displacements at either side of the interface:

$$\sigma(0) = D_3(0^+) - D_3(0^-) = k\varphi(0)[1 + \tilde{\varepsilon}(\mathbf{k}/\omega)]\varepsilon_{\text{vac}} \ , \tag{2.3.4}$$

where the factor $\exp\left[ik(\mathbf{b}\cdot\mathbf{r} - vt)\right]$ is implicitly assumed.

From Eq. (2.3.4), a free-surface propagating wave only exists if

$$1 + \tilde{\varepsilon}(\mathbf{k}/\omega) = 0 \ , \tag{2.3.5}$$

i.e. the phase velocity $v_s(\theta)$ of the wave is given by $1 + \tilde{\varepsilon}(\mathbf{b}/v_s(\theta)) = 0$. This is the piezoelectric-Rayleigh-wave condition within the free-surface boundary conditions, to be solved in the computer by iteration until the minimum result for the modulus $|1 + \tilde{\varepsilon}(\mathbf{b}/v_s(\theta))|$ is found.

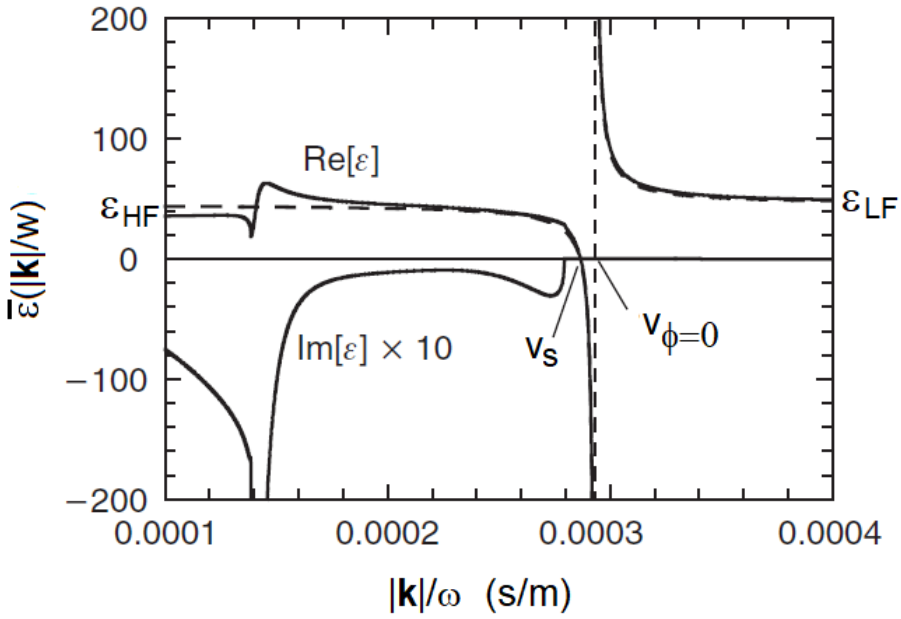

Figure 2.3: Example of plot of a surface permittivity, in this case for $LiNbO_3$ (Y-Cut) and wave propagation along the Z-axis, solved with a program as that in Ref. [57] (solid lines). The dashed lines are calculated with the Ingebrigsten's approximation [18, 28]. The velocities v_s and $v_{\varphi=0}$ are those of a free surface ($\tilde{\varepsilon} = -1$) and a metallic-covered surface ($\tilde{\varepsilon} = \infty$), respectively.

On the other hand, if the boundary is covered by a perfectly conducting metallic film, the short-circuit condition would mean $\varphi(\mathbf{R}, 0, t) = 0$, that is:

$$\tilde{\varepsilon}(\mathbf{k}/\omega) = \infty \ . \tag{2.3.6}$$

2.4 Properties of the surface permittivity

There are free-software tools available to compute any kind of surface waves and permittivities [57], which can be programmed numerically either, and the results have the structure shown in Fig. 2.3 as an example.

It was shown in the previous section that $\tilde{\varepsilon} = \infty$ for the velocity $v_{\varphi=0}$ of a surface wave with metallic boundary condition, and $\tilde{\varepsilon} = -1$ for the usual piezoelectric Rayleigh waves with the free surface covered by a vacuum. In-between, there are the negative values of $\tilde{\varepsilon}$ that solve theoretically the problem when the piezoelectric material is covered by any hypothetical dielectric with $\varepsilon = -\varepsilon_{\text{vac}}\,\tilde{\varepsilon}$. The lowest velocity arises with the metallic covering, since the electric fields screen completely the tangential electric fields accompanying the wave, so that the piezoelectric stiffening (see App. F.2) becomes lower.

In Ref. [58] it is shown that the energetic stability of the piezoelectric guarantees that $\operatorname{Im}\tilde{\varepsilon}(\mathbf{b}/v_s(\theta)) = 0$ up to a $v_L(\theta) > v_0(\theta)$, with $\tilde{\varepsilon}(\mathbf{b}/v_0(\theta)) = 0$. In that range, the four modes in Eq. (2.1.5) are purely decaying on the substrate side. $v_L(\theta)$ marks the starting point at which the piezoelectric surface permittivity has an imaginary part, which reflects the influence of bulk modes (recall that, exactly as in the case of isotropic Rayleigh waves, the piezoelectric modes have velocities lower than the bulk ones, owing to the imaginary component of the wave vector k_3 perpendicular to the surface).

The pseudo-resonances above that threshold correspond to the so-called "pseudo-surface" waves, which leak energy of the wave into the bulk of the piezoelectric material. In the important resonance for surface waves with metallic covering and near the Rayleigh solution, the permittivity can be well approximated by Ingebrigsten's formula:

$$\tilde{\varepsilon}(\mathbf{k}/\omega) = \tilde{\varepsilon}_{\text{HF}}\frac{(\omega/k)^2 - v_0^2}{(\omega/k)^2 - v_{\varphi=0}^2}\ . \tag{2.4.1}$$

Here, this $\tilde{\varepsilon}_{\text{HF}} := \lim_{\omega\to\infty}\tilde{\varepsilon}(\mathbf{k}/\omega)$ will be shown to be lower than $\tilde{\varepsilon}_{\text{LF}} = \lim_{\omega\to 0^+}\tilde{\varepsilon}(\mathbf{k}/\omega)$. The former will also be shown in the next subsection to have the same functional form as the surface permittivity for a pure dielectric, when the coordinates 1-3 are taken, respectively, along the wave direction and the surface normal.

A central quantity in the evaluation of devices which use piezoelectric Rayleigh waves is the *SAW electromechanical coupling coefficient* $K_R(\theta)$,

introduced through the relation at $1 + \tilde{\varepsilon}(\mathbf{b}/v_s(\theta)) = 0$:

$$\frac{K_R^2(\theta)/2}{\tilde{\varepsilon}_{\rm HF}(\theta)+1} = \left[v_s(\theta) \frac{\partial \tilde{\varepsilon}(\mathbf{k}/v)}{\partial v}\Big|_{v=v_s(\theta)} \right]^{-1} \ . \tag{2.4.2}$$

Later it will be shown that very general considerations require the following bound:

$$0 \leq K_R(\theta) < 1 \ , \tag{2.4.3}$$

which is one of the central results of this thesis.

2.4.1 High-frequency limit of $\tilde{\varepsilon}(\mathbf{k}/\omega)$

In this section it will be shown that, if one takes the propagating direction along the x-axis, then:

$$\tilde{\varepsilon}_{\rm HF} = \varepsilon_p := \sqrt{\varepsilon_{11}\varepsilon_{33} - (\varepsilon_{13})^2} \ . \tag{2.4.4}$$

In fact, the modes equation Eq. (2.1.3) is written as:

$$\hat{M} \left(\begin{array}{c} \vec{u} \\ \varphi \end{array} \right) \equiv \left(\begin{array}{cc} \Gamma - \rho v^2 \mathbf{1} & \vec{\gamma} \\ \vec{\gamma}^{\top} & -\varepsilon\varepsilon_{\rm vac} \end{array} \right) \left(\begin{array}{c} \vec{u} \\ \varphi \end{array} \right) = 0 \ , \tag{2.4.5}$$

where the form of the 3×3 matrix Γ, 3×1 vector $\vec{\gamma}$ and constant ε as a function of b [where $\mathbf{b} = (1, 0, b)$] can be read from Eq. (2.1.3).

There are two possibilities for the variation of b as $v \to \infty$, either (a) $b \to \ b_{\rm sm} < \infty$, ("sm" means small) or (b) $b \sim b_{\rm bg} \to \infty$ ("bg" is for big).

In case (a), $\Gamma - \rho v^2 \mathbf{1}$ will never be singular. Then, using the determinant formula from Schur's complement $\det(\hat{M}) = \det(\Gamma - \rho v^2 \mathbf{1}) \det(-\varepsilon - \vec{\gamma} \cdot (\Gamma - \rho v^2 \mathbf{1})^{-1} \cdot \vec{\gamma})$, it is immediate to realize that $\varepsilon = O(v^{-2})$, which leads to the decaying root $b_{\rm sm} = -(\varepsilon_{31} + i\varepsilon_p)/\varepsilon_{33}$.

From the modes equation (2.4.5), it is found that:

$$\begin{pmatrix} \vec{u}_{\rm sm} \\ \varphi_{\rm sm} \end{pmatrix} \simeq \begin{pmatrix} O(v^{-2}) \\ 1 \end{pmatrix} , \tag{2.4.6}$$

where here and in the rest of this subsection, the modes amplitudes are normalized, so that $\varphi_{\rm sm,bg} = 1$.

For the other case (b), from the modes equation (2.4.5), one finds that $b_{\rm bg} = O(v)$. Hence, expanding $\hat{M}$ from:

$$\begin{aligned} \Gamma_{ij} &\simeq b_{\rm bg}^2\, c_{3ij3} \\ \gamma_i &\simeq e_{33i}\, b_{\rm bg}^2 \\ \varepsilon &\simeq \varepsilon_{33}\, b_{\rm bg}^2 , \end{aligned} \tag{2.4.7}$$

but now the general form of these modes is

$$\begin{pmatrix} \vec{u}_{\rm bg} \\ \varphi_{\rm bg} \end{pmatrix} \simeq \begin{pmatrix} \alpha_j^{(i)} \\ 1 \end{pmatrix} , \tag{2.4.8}$$

where the notation in Eq. (2.1.5) has been used, and $\alpha_a^{(1,2,3)}$ for the three $(\vec{u}_{\rm bg}, \varphi_{\rm bg})$ modes and $\alpha_a^{(4)}$ for the $(\vec{u}_{\rm sm}, \varphi_{\rm sm})$ mode are chosen.

Choosing the constant $C_4 = 1$, the mechanical boundary condition of Eq. (2.1.7) leads to:

$$0 \simeq C_k b^{(k)} (\alpha_j^{(k)} c_{3ij3} + e_{33i}) + (e_{13i} + b^{(4)} e_{33i}) , \tag{2.4.9}$$

and $C_k = O(v^{-1})$, so the denominator in Eq. (2.3.2) can be approximated as $C_m \alpha_4^{(m)} \simeq 1$.

On the other hand, the "big" (bg) contribution to the displacement field is, to order $O(v^0)$:

$$D_3(0^-)|_{\rm bg} \simeq ikc_i b^{(i)} (\alpha_j^{(i)} e_{33j} - \varepsilon_{33}\varepsilon_{\rm vac}) \simeq 0 , \tag{2.4.10}$$

the last approximate equality comes from the second Eq. (2.4.5) together

with Eq. (2.4.7).

Collecting all these results together with the "small" contribution to $D_3(0^+)$ into Eq. (2.3.2), one finally gets [59]:

$$\tilde{\varepsilon}_{\mathrm{HF}} = -ib_k^4(\varepsilon_{3k}) = \varepsilon_p \ . \tag{2.4.11}$$

2.4.2 Relation to response functions

Let us now consider a 1D situation, in which flat electrodes parallel to the y-axis operate on top of the piezoelectric substrate shown in Fig. 2.1. Therefore, the angle $\theta = 0$ is chosen, and there is no y dependence. Then, θ is omitted and not written in this subsection.

The charge-potential relation Eq. (2.3.4) for the amplitudes is written so that the complex admittance $\chi(k,\omega)$ is defined as:

$$\begin{aligned} \varphi(k,\omega) &= \gamma(k,\omega)\sigma(k,\omega) \\ \gamma(k,\omega) &:= \frac{1}{|k|}\frac{1}{(\tilde{\varepsilon}(k,\omega)+1)\varepsilon_{\mathrm{vac}}} \ , \end{aligned} \tag{2.4.12}$$

where the possibility of negative k is now allowed, because of the omission of the θ dependence. From Eq. (2.1.3), $\tilde{\varepsilon}(k,\omega) = f((\omega/k)^2) = f(v^2)$, and its analytical extensions can be guessed from the requirements of causality, which for $\omega > 0$ mean that the poles and zeros of $\gamma(k,\omega)$ are placed in the lower complex ω half-plane.

The instantaneous part is defined as:

$$\gamma_\infty(k) := \frac{1}{|k|}\frac{1}{(\tilde{\varepsilon}_{\mathrm{HF}}+1)\varepsilon_{\mathrm{vac}}} = \int dx\, e^{-ikx}\gamma_\infty(x) \ , \tag{2.4.13}$$

and the retarded and static contributions:

$$\gamma_{\mathrm{ret}}(k,\omega) := \gamma(k,\omega) - \gamma_\infty(k) = \int dx \int_0^\infty e^{i(\omega t - kx)}\phi(x,t) \ , \tag{2.4.14}$$

$$\gamma_0(k) := \gamma(k,0) = \frac{1}{|k|}\frac{1}{(\tilde{\varepsilon}_{\rm LF}+1)\varepsilon_{\rm vac}} = \int dx\, e^{-ikx}\gamma_0(x)\ ,$$
$$\gamma_0(x) = \gamma_\infty(x) + \int_0^\infty ds\, \phi(x,s)e^{-\eta s}\ , \tag{2.4.15}$$

where η is to be understood as $\eta \to 0^+$.

All this amounts to writing the general linear causal relation [60]:

$$\varphi(x,t) = \int dx' \left[\gamma_\infty(x-x')\sigma(x',t) + \int_{-\infty}^{t} dt'\, \phi(x-x',t-t')\sigma(x',t')\right]\ . \tag{2.4.16}$$

The power delivered to the electrodes to maintain a given $\varphi(x,t), \sigma(x,t)$ (in this subsection, it is assumed that all fields which depend on space-time are real) is:

$$\frac{dU(t)}{dt} = \sqrt{A}\int dx\, \varphi(x,t)\dot{\sigma}(x,t)\ , \tag{2.4.17}$$

where $\sqrt{A}$ is the length along the y-direction.

If starting from zero fields and charges, one adiabatically turns on a given surface charge distribution $\sigma(x,t) = \sigma(x)\exp(\eta t)$, from Eqs. (2.4.16-2.4.17) the total energy supplied is:

$$\frac{\Delta U_{\rm ad}}{\sqrt{A}} = \int dx \int dx' \sigma(x)\frac{\gamma_0(x-x')}{2}\sigma(x')$$
$$= \frac{1}{2(\tilde{\varepsilon}_{\rm LF}+1)\varepsilon_{\rm vac}}\int \frac{dk}{2\pi}\frac{|\sigma(k)|^2}{|k|}\ . \tag{2.4.18}$$

Analogously, an instantaneous charging to the same final charge distribution $\sigma(x,t) = \theta_\epsilon(t)\sigma(x)$, with $\theta_\epsilon(t)$ a differentiable approximation to the Heaviside θ-function such that $\theta_\tau(t) \to \theta(t), \tau \to 0^+$, requires an amount of work given by:

$$\frac{\Delta U_{\rm inst}}{\sqrt{A}} = \int dx \int dx'\, \sigma(x)\frac{\gamma_\infty(x-x')}{2}\sigma(x')$$
$$= \frac{1}{2(\tilde{\varepsilon}_{\rm HF}+1)\varepsilon_{\rm vac}}\int \frac{dk}{2\pi}\frac{|\sigma(k)|^2}{|k|}\ . \tag{2.4.19}$$

The second process, being non-adiabatic, absorbs more energy from the source that exerts work on the system. This extra energy is employed in inducing surface-wave and bulk-wave excitations. As a result, $\Delta U_{\rm inst} > \Delta U_{\rm ad}$, which implies:

$$\tilde{\varepsilon}_{\rm HF} < \tilde{\varepsilon}_{\rm LF} \ . \tag{2.4.20}$$

2.4.3 Energy carried by a piezoelectric SAW pulse

For piezoelectric phenomena, the Poynting vector is given in Eq. (F.4.3) in the App. F:

$$P_j = -T_{ij}\dot{u}_i + \varphi \dot{D}_j \ , \tag{2.4.21}$$

which after use of Eq. (F.1.1) can be seen to be a bilinear expression in the vectors $(u_a, u_{a,i})$ and $(\dot{u}_b, \dot{u}_{b,j})$ (here $i,j = 1,2,3$ and $a,b = 1,2,3,4$; where $u_4 = \varphi$).

For any given pulse propagating in the x-direction, $u_a(x,y,z,t) = f_a(x - vt, z)$, one can compute the total energy which crosses x (it is obviously independent of x)

$$\begin{aligned} \Delta U_{\rm pulse} &= \int\!\!\!\int\!\!\!\int_{-\infty}^{\infty} dt\, dy\, dz\, P_1(x,y,z,t) \\ &= \sqrt{A} \int\!\!\!\int_{-\infty}^{\infty} dt\, dz\, g_r(x - vt, z) P_{rs} g_s(x - vt, z) \ , \end{aligned} \tag{2.4.22}$$

where g_r, g_s are taken from the vector components $u_a, u_{a,i}, \dot{u}_a, \dot{u}_{a,i}$ with $r,s = 1,2,...,16$, and P_{rs} is a constant matrix whose elements come from the tensors $\hat{e}, \hat{c}, \hat{\varepsilon}$. Fourier-analyzing $g_r(x - vt, z) = \int (dk/2\pi)\, e^{ik(x-vt)} g_r(k,z)$, where because of reality $g_r(k,z)^* = g_r(-k,z)$, one obtains:

$$\Delta U_{\rm pulse} = \sqrt{A}\, \frac{1}{v} \int \frac{dk}{2\pi} \int dz\, g_r(k,z) P_{rs} g_s(k,z)^* \ , \tag{2.4.23}$$

but then [18, 23], the expression:

$$\frac{1}{2}\int dz\, g_r(k,z)P_{rs}g_s(k,z)^* = \frac{v|k|}{4}\omega\frac{\partial\tilde{\varepsilon}(\mathbf{k},\omega)}{\partial\omega}|\varphi(k,0)|^2 \tag{2.4.24}$$

is the time-average power per unit length crossing a yz-section, carried by a harmonic piezoelectric SAW, whose electric-potential amplitude is $\varphi(k,0)$ at the interface. The result is therefore:

$$\Delta U_{\text{pulse}} = \sqrt{A}\,\frac{(\tilde{\varepsilon}_{\text{HF}}+1)\varepsilon_{\text{vac}}}{K_R^2}\int\frac{dk}{2\pi}|k||\varphi(k,0)|^2\ . \tag{2.4.25}$$

2.5 Other types of piezoelectric surface acoustic waves

One must be aware that Rayleigh-like solutions do not exhaust the possible solutions of piezoelectric surface acoustic waves, in spite of being the most important by far. As in the case of purely elastic materials (outlined in Sec. E.2 in the App. E), there are other possibilities for solutions of the wave equation arising in this piezoelectric scenario in the surface.

The case of a standard, semi-infinite, non-layered, piezoelectric surface contains new kind of waves different than the Rayleigh ones. A very important example lies in the so-called *Bleustein-Gulyaev* [54] waves, strongly related to the SH waves in the elastic scenario. These analytical solutions only appear if the saggital plane is normal to an even-order axis of the crystal, with an exponential decay from the surface of the form $\exp(-K^2kz)$. Here, k is the wave vector, z is the spatial coordinate perpendicular to the surface, and K^2 is a nonzero electromechanical coupling coefficient, whose smallness makes the wave to be lightly bounded to the surface (for example, the penetration depth of this wave in CdS is around 44 wavelengths, in stark contrast to the single-wavelength penetration of Rayleigh waves). In exactly the same way as the Rayleigh modes, a metallic layer renormalizes the bare velocity of free Bleustein waves from v_s to $\tilde{v}_s$, where $\tilde{v}_s^2 = v_s^2(1-K^4)$ [see Eq. (3.3.15)].

In other circumstances, extra solutions appear in unique propagation directions, such as the *pseudo-surface acoustic* waves, and there is a small interval around their direction allowing for the so-called *leaky surface acoustic* waves, which are not true surface waves. Even though they can be important for the topic of surface-acoustic-wave devices and IDTs, the fact that they appear only in very singular directions make them much less important for the topic of microscopic electron-phonon interactions.

In the case of the layered systems, it is seen in the App. E that elastic Rayleigh waves can become dispersive, and comprise multiple modes. The situation in piezoelectric materials becomes much more complex and is developed in more specialised literature (cited in Refs. [23, 18, 56]). A deeper analysis of a piezoelectric substrate, possibly layered, would require their computation and a quantization to study their coupling to the carriers in the 2D metallic material placed onto the substrate (which is the topic of Ch. 3), since these other waves appear in all directions, exactly as the semi-infinite Rayleigh-wave solutions do.

All surface waves together modify the slowness-surface projections as those shown in Fig. D.1 after the introduction of the other modes [21, 23], begetting new curves and branches.

Chapter 3

Quantization of surface acoustic waves and their interaction with electrons

3.1 Surface electron-phonon Hamiltonian

The surface of any material interacts with quantum fields such as those of electrons, photons, and phonons, very much as in the bulk. For example, an electron (or charged quasiparticle) attached to a surface exerts forces upon the charged ions of the surface, changing their dynamics. Moreover, the ions act back again on the first electron, modifying its properties, such as its energy and effective mass. This influence modifies as well the properties of ensembles of 2D electron gases near that surface and the space-time dependent dielectric functions $\varepsilon(\mathbf{r}, \mathbf{r}', t, t')$ describing these fields. The quantum-mechanical theory of these general kind of interactions (in the form of electron-phonon Hamiltonians) is described in any many-body physics literature [61, 62, 63, 64].

While many lattice-induced surface effects are analogous to the 3D bulk ones, there are some features arising due the new dimensionality and geom-

etry. For example, the usual (bare) 3D Fourier transform of the Coulomb potential changes from $\frac{e^2}{4\pi\varepsilon_{\rm vac} r} \to \frac{e^2}{\varepsilon_{\rm vac} q^2}$ to the new q-dependent function $\frac{e^2}{2\varepsilon_{\rm vac} q}$. Also, a dielectric constant in a plane medium surrounded by two dielectrics with ε_1 above and ε_2 below changes the in-plane dielectric constant to $\frac{\varepsilon_1+\varepsilon_2}{2}$ [65, 29]. All the 2D electron-phonon physics is relevant for surfaces near classical 2DEG in semiconductor heterostructures [66, 67] or with the placing of two-dimensional materials like graphene onto them, something unavoidable in the practical uses of these 2D crystals (see Sec. 1.1.1).

3.1.1 Fröhlich Hamiltonian

In a polar semi-infinite material, the coupling of a single electron in its surface with the longitudinal optical phonons in that surface is given by the Fröhlich Hamiltonian [16, 42, 68, 69, 70, 71]. This is usually written in second-quantized language in the form:

$$H_{\rm Fr} = \sum_{\mathbf{k},\sigma} E_{\mathbf{k}} a^\dagger_{\mathbf{k},\sigma} a_{\mathbf{k},\sigma} + \hbar\omega_0 \sum_{\mathbf{q}} b^\dagger_{\mathbf{q}} b_{\mathbf{q}} + H^{\rm op}_{\text{e-ph}} \ , \tag{3.1.1}$$

$$H^{\rm op}_{\text{e-ph}} = \frac{1}{\sqrt{A}} \sum_{\mathbf{k},\mathbf{q},\sigma} \gamma^{\rm op}_{\mathbf{q}}\, a^\dagger_{\mathbf{k}+\mathbf{q},\sigma} a_{\mathbf{k},\sigma} b_{\mathbf{q}} + \text{H.c.} \ ,$$

where $a^\dagger_{\mathbf{k}+\mathbf{q},\sigma}$, $a_{\mathbf{k},\sigma}$ are the electron creation and annihilation operators, respectively, with momentum $\mathbf{k}$ and spin σ and $b^{(\dagger)}_{\mathbf{q}}$ is the phonon annihilation (creation) operator. $E_{\mathbf{k}}$ is the energy of the electron in the state $(\mathbf{k},\sigma)$ and $\hbar\omega_0$ for each phonon (they are approximated by Einstein dispersionless modes with frequency ω_0). If the electron is embedded in a 2DEG, its energies can always be linearized close to the Fermi surface by $E_{\mathbf{k}} = \pm\hbar v_{\rm F} k$. The area A will drop by passing from the sum to an integral in k-space via the density of states. This Fröhlich interaction is given by the vertex $\gamma^{\rm op}_{\mathbf{q}}$,

usually in units of eV cm (but adimensional in some references [72]):

$$|\gamma_{\mathbf{q}}^{\mathrm{op}}|^2 = g\frac{e^2\hbar\omega_0}{2q} = g\frac{2\pi\varepsilon_{\mathrm{vac}}\alpha_{\mathrm{fs}}\hbar(\hbar\omega_0)v_{\mathrm{F}}}{q} \ , \tag{3.1.2}$$

$$g = \frac{1}{\varepsilon_{\mathrm{vac}}}\left(\frac{1}{\varepsilon_\infty+1} - \frac{1}{\varepsilon_0+1}\right) \ , \tag{3.1.3}$$

and derived exactly as in the case of 3D [64]. Here, $\varepsilon_\infty, \varepsilon_0$ denote the relative dynamic and static dielectric constants, respectively; and $\alpha_{\mathrm{fs}} = \frac{e^2}{4\pi\varepsilon_{\mathrm{vac}}\hbar v_{\mathrm{F}}}$. The high-frequency dielectric constant ε_∞ only includes the screening of the very fast excitons. In three dimensions, in the bulk of the polar material, this interaction looks quite the same, except for the fact that the long-range Coulomb factor is q^{-2} instead of q^{-1} and one has just ε_i instead of $\varepsilon_i + 1$ (the former 1 applying when the system is covered by the air/vacuum) for $i = 0, \infty$; together with an extra factor 2 [64, 61]. The change from SI units to cgs proceeds just with the replacement $e^2/\varepsilon_{\mathrm{vac}} \to 4\pi e^2$.

This Hamiltonian is the basis of the *Fröhlich polaron* theory [61, 73, 74, 75], a classical topic in the big problem of the polaron arising many decades ago and strongly studied since the 40-50s with any kind of perturbation theory or variational methods with path integrals.

3.1.2 Dielectric function for 2D electron gases interacting with Fröhlich optical phonons

In a many-electron system, one just adds to the previous single-electron Hamiltonian [Eq. (3.1.1)] the extra electron-electron interaction, and the chemical potential μ is introduced through the replacement $E_{\mathbf{q}} \to E_{\mathbf{q}} - \mu$,

where $E_{\mathbf{q}}$ is the single-electron energy:

$$H = H_{\rm Fr} + \frac{1}{2A}\sum_{\mathbf{q}} v_{\mathbf{q}}^{(\infty)} \rho(\mathbf{q})\rho(-\mathbf{q}) \ , \tag{3.1.4}$$

$$v_{\mathbf{q}}^{(\infty)} = \frac{e^2}{2\overline{\varepsilon}_\infty \varepsilon_{\rm vac} q} \ , \qquad \overline{\varepsilon}_\infty = \frac{\varepsilon_\infty + 1}{2} \ ,$$

$$\rho(\mathbf{q}) = \sum_{\mathbf{k},\sigma} a^\dagger_{\mathbf{k}+\mathbf{q},\sigma} a_{\mathbf{k},\sigma} \ .$$

In particular, when a graphene layer or a 2D material is placed onto such a polar semi-infinite 3D substrate (surrounded by air/vacuum), the carriers from the 2DEG of graphene interact with the polar optical 2D phonons arising in the interfacial surface of the substrate. The Hamiltonian is exactly like this except for an exponential factor $\gamma_{\mathbf{q}}^{\rm op} \propto e^{-qd}$, with d the distance from graphene to the substrate. This must be attached as a factor to the vertex from before. It can be approximated as 1 provided that the graphene layer is placed directly onto the substrate, since d would be some angstroms, and the inverse of the wave vectors q would be much bigger, as we shall see. Actually, the Fröhlich matrix element term in Eq. (3.1.2) is only valid for long wavelengths from phonons quite far from the edge of the Brillouin zone, such as those in the range of the Fermi wave vector of graphene.

In order to describe the properties of this coupled system of 2D phonons and electrons (or, more specifically, graphene electrons and surface optical modes from the substrate), the main goal is to compute the dielectric function $\varepsilon(\mathbf{q},\omega)$ in such a way that the total dressed electron-electron interaction is:

$$V_{\rm eff}(\mathbf{q},\omega) = \frac{v_{\mathbf{q}}}{\varepsilon(\mathbf{q},\omega)} = \frac{e^2}{2\varepsilon(\mathbf{q},\omega)q} \ . \tag{3.1.5}$$

The calculation of $\varepsilon(\mathbf{q},\omega)$ can be done at least in three ways. One can use a phenomenological model for the ions as oscillators with polarizability $\propto (\omega_0^2 - \omega^2)^{-1}$. Or it is possible to consider the ions as a plasma analogous to the electronic one but with charge Ze and mass M much bigger than the

electrons' [76]. In any case, one gets the well-known result [61]:

$$\varepsilon(\mathbf{q},\omega) = \overline{\varepsilon}_\infty + \frac{\overline{\varepsilon}_0 - \overline{\varepsilon}_\infty}{1 - \frac{\omega^2}{\omega_0^2}} - v_\mathbf{q}\,\Pi_0(\mathbf{q},\omega)\ , \tag{3.1.6}$$

where Π_0 is the irreducible polarization function of the 2D electron gas [66, 77].

The third (and most common and rigorous) method to get an effective interaction proceeds by combining both electron-electron and electron-phonon interactions in a RPA scheme from the combined Hamiltonian, dressing the interaction as in Fig. 3.1, by summing to infinite order in perturbation theory to get a Dyson-like equation. All the non-bubble virtual processes are neglected and this is well justified for low values of the parameter r_s [62] [Eq. (4.2.3)]. The result can be expressed as:

$$V_{\text{eff}}(\mathbf{q},\omega) = \frac{v_\mathbf{q}}{\varepsilon(\mathbf{q},\omega)} = \frac{v_\mathbf{q}^{(\infty)} + V_{\text{ph}}^{\text{op}}(\mathbf{q},\omega)}{1 - \left[v_\mathbf{q}^{(\infty)} + V_{\text{ph}}^{\text{op}}(\mathbf{q},\omega)\right]\Pi_0(\mathbf{q},\omega)}, \tag{3.1.7}$$

where $V_{\text{ph}}^{\text{op}}(\mathbf{q},\omega) = |\gamma_\mathbf{q}^{\text{op}}|^2 G_0^{\text{op}}(\mathbf{q},\omega)$, and $G_0^{\text{op}}(\mathbf{q},\omega) = \frac{2\omega_0}{\hbar\left(\omega^2-\omega_0^2+i\eta\right)}$ as the bare optical phonon propagator ($\eta \to 0^+$). Solving the Dyson equation self-consistently leads to the previous effective interaction in Eq. (3.1.7). This mechanism of remote electron-phonon scattering in graphene has been mainly studied for substrates supporting these kind of Fröhlich optical-phonon modes [16, 78, 79, 80, 81, 82, 83, 84].

At low frequencies ($\omega \ll \omega_0$), corresponding to the interaction between electrons whose difference in energies is very small in the scale of the optical energies (around $\hbar\omega_0 \sim 0.1\,\text{eV}$), the bare phonon-mediated electron-electron interaction is $V_{\text{ph}}^{\text{op}}(\mathbf{q},\omega \simeq 0) = |\gamma_\mathbf{q}^{\text{op}}|^2 G_0^{\text{op}}(\mathbf{q},\omega \simeq 0) = \frac{e^2}{\varepsilon_{\text{vac}} q}\left(\frac{1}{\varepsilon_\infty+1} - \frac{1}{\varepsilon_0+1}\right)$. This has the same form as the Coulomb interaction because $|\gamma_\mathbf{q}^{\text{op}}|^2 \sim 1/q$ and $\hbar\omega_0$ is constant, except for a factor which implies that at small frequencies (in the scale of ω_0) the dynamic core-exciton-generated dielectric constant $\overline{\varepsilon}_\infty$ is to be substituted by the static $\overline{\varepsilon}_0$, and that is exactly the definition of the static dielectric constant which enters in the derivation of

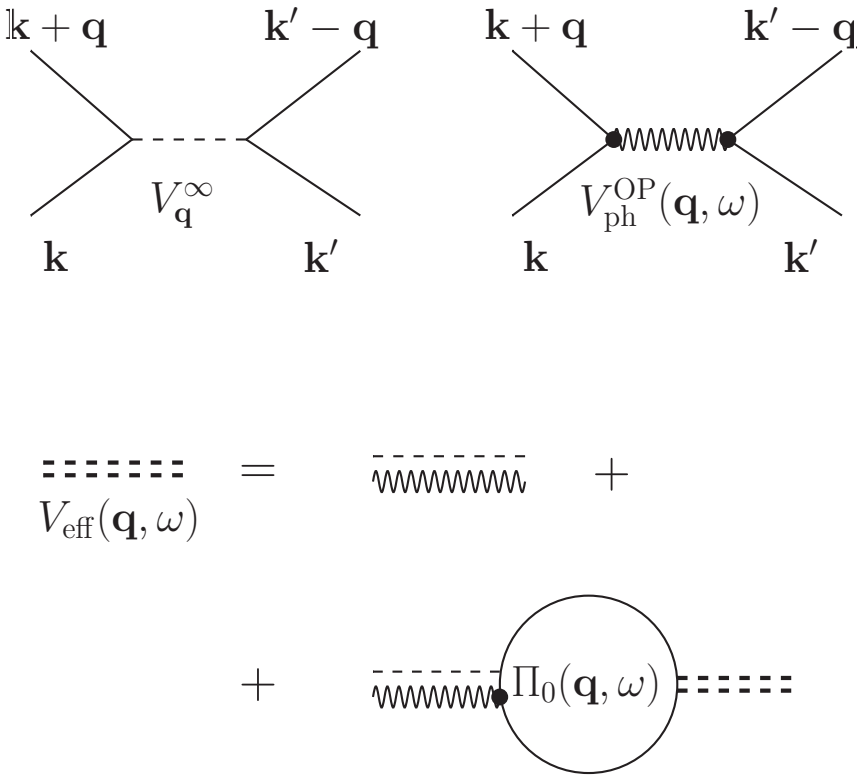

Figure 3.1: Diagrammatics of the electron-electron interaction in a solid. Top: bare electron-electron interactions mediated by the Coulomb repulsion (photons) and by optical phonons, respectively. Bottom: effective electron-electron interaction in the RPA.

the phenomenological Fröhlich interaction.

At these small frequencies and for $q < 2k_F$, the dielectric function leads to the classical RPA result:

$$\varepsilon(\mathbf{q},\omega \simeq 0) = \overline{\varepsilon}_0\, \varepsilon_{\mathrm{RPA}}(\mathbf{q},0)\ , \tag{3.1.8}$$

$$\varepsilon_{\mathrm{RPA}}(\mathbf{q},0) = 1 - v_{\mathbf{q}}^{(0)}\Pi_0(\mathbf{q},0) = 1 + \frac{k_{\mathrm{TF}}}{q}\ , \tag{3.1.9}$$

$$k_{\mathrm{TF}} = \frac{e^2 D(E_F)}{2\,\varepsilon_{\mathrm{vac}}\,\overline{\varepsilon}_0} = \frac{2g_v\alpha_{\mathrm{fs}}}{\overline{\varepsilon}_0}k_{\mathrm{F}} = 2g_v r_s k_{\mathrm{F}}\ , \tag{3.1.10}$$

being k_{TF} the Thomas-Fermi screening wave vector and $D(E_F) = g_v k_{\mathrm{F}}/\pi\hbar v_{\mathrm{F}}$ the electronic density of states at the Fermi energy (g_v is the valley degeneracy, e.g. $g_v = 2$ in monolayer graphene).

In these materials, the long-range net electron-electron interaction is always repulsive and never overscreened, even though it can become greatly reduced by the optical phonons provided that the ratio $\varepsilon_\infty/\varepsilon_0$ is quite small. That happens in very polar materials such as the ferroelectrics. This oversimplified model does not account for direction anisotropies or the usual case of many different modes (it can be refined with better anisotropic oscillator models with similar results) but it contains the important essence of the role of the optical modes screening the slower acoustic phonons.

3.1.3 Deformation-potential interaction

Another important source for the electron-phonon interaction, both in the bulk or in a 2D surface, comes from the deformation potential [49, 85, 86, 87], especially important for crystals lacking a piezoelectric effect, such as a pure ideal graphene layer. To lowest order in the displacement of the atoms of a solid, the electric energy stored in a displacement is proportional to the strain:

$$e\phi = \Xi_{ij} u_{ij} \ , \tag{3.1.11}$$

where the deformation-potential tensor Ξ_{ij} has the same symmetry considerations as the piezoelectric one and other tensors (see Sec. C.2). In particular, it becomes a scalar in a cubic crystal, so that the interaction of electrons with acoustic deformation-potential phonons reads:

$$H_{\text{e-ph}}^{\mathrm{DA}} = \Xi \nabla \cdot \mathbf{u} \ , \tag{3.1.12}$$

where $\mathbf{u}$ is the mechanical displacement of the phononic field.

From the very introduction of this phenomenon (see Ch. 3 in Ref. [47]) as a microfield, a key feature of this potential is that it should not be screened like other macroscopic fields, i.e., ϕ is not a macroscopic potential

in the sense of the macroscopic Maxwell's equations in Eq. (3.1.11). All the screening processes are included in the first-order approximation within the deformation tensor. In discussing theoretical issues, however, many researchers do it and compare to non-screened results [88, 89, 90]. The results after screening might be accounted with reasonable skepticism.

3.2 2D piezoelectric electron-phonon interactions

The coupling of the piezoelectric-SAW phonons to the electrons from a 2DEG or from graphene has been computed, within certain simplifying assumptions and for definite substrate crystal structures, for example in Refs. [29, 49, 50], based in the bulk theory [47, 61]. These methods of derivation of the surface electron-phonon interaction for a piezoelectric material have been performed only within a purely elastic Rayleigh wave approximation [49, 50] or for definite propagating directions [29], exactly as the solutions for SAWs explained in Sec. 2.2. But these methods fail in stronger piezoelectric materials and for other crystal symmetries, as pointed out there. Moreover, the obtained vertices are expressed in terms of a matching constant whose physical interpretation is rather obscure, allowing for just order of magnitude estimates.

A central topic in this work is to calculate a general electron-phonon interaction [see Eq. (4.1.2)], which is expressed solely in terms of physical quantities characterizing the response of the substrate surface. We emphasize that all the quantities appearing in the vertex are both computable from linear piezo-elasticity theory and experimentally measurable. One of them, the ubiquituous electromechanical coupling coefficient, K_R, will turn out to be central to all computations, serving as a natural dimensionless parameter which provides the scale for the effect of the substrate piezoelectricity on the 2D electron system. Moreover, from very general considerations, it will be possible to provide bounds on its size: $0 \leq K_R < 1$ [see Eq. (4.1.17)].

It is important to note that the vertex written here is derived within the framework of linear piezo-elastic theory, which means that its validity should be restricted to low-amplitude, low-frequency and long-wavelength phenomena. Bulk modes are also left aside in this work. On the other hand, our study is not restricted to any approximation based on the symmetry or the piezoelectric softness of the substrate.

3.2.1 Classical approximations

Let us suppose the simple case of a GaAs substrate (see Sec. 2.2), with a 2DEG at the interface ($z = 0$) between vacuum ($z > 0$) and the substrate ($z \leq 0$), as in Fig. 2.1. In order to compute the interaction of the 2DEG electrons with the acoustic piezoelectric phonons located in this surface, it is needed to find the displacement $u_{\mathbf{q}}(\mathbf{r}, t)$ for each mode with any wave vector $\mathbf{q}$, to quantize it and to find the associated electric potential $\varphi_{\mathbf{q}}(\mathbf{r}, t)$.

From the approximate solution in Sec. 2.2, the constant $C_{\mathbf{q}}$ is taken such that the total energy (averaged in time) of the mode [see Eq. (F.3.3)], given by

$$\langle E(\mathbf{u_q})\rangle = \frac{1}{2}\,\rho \int d^3\mathbf{r} \left[(\ddot{\mathbf{u}})^2 + (v_l^2 - 2v_t^2)(\nabla \cdot \mathbf{u})^2 + 2v_t^2 \sum_{ij} (u_{ij})^2 \right] , \tag{3.2.1}$$

is equal to $\langle E(\mathbf{u_q})\rangle = \hbar\omega_{\mathbf{q}}$. The constant is found this way to be

$$C_{\mathbf{q}} = \left(\frac{1}{A} \frac{\hbar}{\rho v_s a} \right)^{1/2} \equiv C \ , \tag{3.2.2}$$

with a of order 1. It does not depend on $\mathbf{q}$, as opposed to the bulk modes [49]. From the classical field in Eq. (2.2.4) in this non-piezoelectric case, the general quantized displacement field becomes:

$$\mathbf{u}(\mathbf{r}, t) = C \sum_{\mathbf{q}} b_{\mathbf{q}} \exp[i(\mathbf{q} \cdot \mathbf{R} - \omega_{\mathbf{q}} t)]\, \mathbf{v}_{\mathbf{q}}(z) + \text{H.c.} \ , \tag{3.2.3}$$

including the electric-potential operator from Eq. (2.2.9):

$$\phi(\mathbf{r},t) = C\sum_{\mathbf{q}} b_{\mathbf{q}}\varphi_{\mathbf{q}} + \text{H.c.}\ , \tag{3.2.4}$$

where $b_{\mathbf{q}}^{(\dagger)}$ is now the phononic annihilation (creation) operator for a SAW mode with wave vector $\mathbf{q}$, acting on the Fock space of the SAW phonons.

In this example of GaAs within this isotropic non-piezoelectric approximation, the electron-phonon-interaction term for the Hamiltonian, analogous to the Fröhlich interaction in Eq. (3.1.1), comes from the new matrix elements of the electric potential felt by the electrons ($e = 1.6\times10^{-19}\,\text{C}$ is in this case the electron charge and should not be confused with the piezoelectric tensor $\hat{e}$ or its components e_{ij}):

$$H_{\text{e-ph}}^{\text{PA}} = \int d\mathbf{r}\, e\rho(\mathbf{r},t)\phi(\mathbf{r},t) = \frac{1}{\sqrt{A}}\sum_{\mathbf{k},\mathbf{q},\sigma}\gamma_{\mathbf{q}}^{\text{PA}}\, a_{\mathbf{k}+\mathbf{q},\sigma}^{\dagger}a_{\mathbf{k},\sigma}b_{\mathbf{q}} + \text{H.c.}\ , \tag{3.2.5}$$

and the vertex in this case is given by [see Eq. (2.2.9)]:

$$\begin{aligned}\gamma_{\mathbf{q}}^{\text{PA}} = C\sqrt{A}\,\frac{e\beta\zeta^{-2}\varepsilon_0}{\varepsilon_0+1}\,\frac{q_xq_y}{q^2}[&3\kappa_l\alpha^{-1}(1-\kappa_l)\\ &- f(1+2\kappa_t^2)(1-\kappa_t) - \zeta^2(1-f\kappa_t)]\ ,\end{aligned} \tag{3.2.6}$$

which is of order:

$$\gamma_{\mathbf{q}}^{\text{PA}} \sim \sqrt{\frac{\hbar}{\rho v_s}}e\beta_{(\text{cgs})} = \sqrt{\frac{\hbar}{\rho v_s}}\frac{2ee_{14}}{\varepsilon_0\varepsilon_{\text{vac}\,(\text{SI})}}\ . \tag{3.2.7}$$

The proportionality factor $\frac{1}{\sqrt{a}}[3\kappa_l\alpha^{-1}(1-\kappa_l) - ...]$ is [see Eq. (3.2.2)] of course of order 1 and it depends just on the elastic constants and the geometry. This interaction is anisotropic because $q_x = q\cos\theta$ and $q_y = q\sin\theta$ with θ measured in the surface. For a general material, it has an

expansion within this (non-piezoelectric wave) approximation as:

$$|\gamma_{\mathbf{q}}^{\mathrm{PA}}|^2 = \sum_{n\geq 0} c_j^{\mathrm{PA}} (\sin\theta)^{2n} \ , \tag{3.2.8}$$

with terms c_j^{PA} of order $\sim \frac{\hbar}{\rho v_s}\frac{e^2\hat{e}^2}{\varepsilon^2}$.

In addition to their characteristic anisotropy, it must be noted that $\gamma_{\mathbf{q}}^{\mathrm{PA}}$ does not depend on the modulus q. This happens because the electric potential ϕ is proportional to the displacement and thus to the characteristic normalization $C \propto \left(\frac{\hbar}{\rho v_s a}\right)^{1/2}$, not dependent on q, that arises at the surface for these modes [see the discussion right before Eq. (3.2.3)] from the fact that a quantum of energy $\propto q$ is confined in a layer below the surface of thickness $\sim \lambda \propto 1/q$. By contrast, a dependence on q does arise in the typical metal bulk-phonon modes or in semiconductor deformation potentials, where $\gamma_{\mathbf{q}} \sim \sqrt{q}$ [86, 76], or even in piezoelectric modes in the bulk, where $\gamma_{\mathbf{q}} \sim q^{-1}$ [47].

Deformation-potential interaction

In addition to the mainly studied piezoelectric interaction, one must add the electron-phonon-interaction effects arising from the deformation potential of the acoustic phonons from this GaAs substrate (or from the 2D material itself). As explained in Sec. 3.1.3, and from Eqs. (3.2.3) and (3.1.12), one ends up in this case with the interaction term:

$$H_{\text{e-ph}}^{\mathrm{DA}} = \frac{1}{\sqrt{A}} \sum_{\mathbf{k},\mathbf{q},\sigma} \gamma_{\mathbf{q}}^{\mathrm{DA}}\, a_{\mathbf{k}+\mathbf{q},\sigma}^{\dagger} a_{\mathbf{k},\sigma} b_{\mathbf{q}} + \mathrm{H.c.} \ , \qquad \gamma_{\mathbf{q}}^{\mathrm{DA}} = C\sqrt{A}\,\alpha\zeta^2 \Xi_{\mathrm{GaAs}}\, q \ . \tag{3.2.9}$$

This vertex, being proportional to the change in volume associated with each phonon, is now proportional to q and hence its influence decreases for long wavelengths. In the case of GaAs and upon introduction of the proper numerical values [49], the ratio of both vertices becomes $\gamma_{\mathbf{q}}^{\mathrm{DA}}/\gamma_{\mathbf{q}}^{\mathrm{PA}} \simeq$

$q \times 10^{-7}\,\mathrm{cm}$.

3.2.2 Figure of merit for GaAs

It is possible to compute K^2 in the simple well-known cubic example of GaAs, as outlined before. Recall (see Sec. 2.2) that the piezoelectric and dielectric tensors are given by the numbers $e_{14} \approx 0.15\,\mathrm{C/m^2}$ (strongly dependent on the reference), $\varepsilon_0 \approx 12$ [now denoting a relative constant, so that $\hat{\varepsilon} = 12\,\varepsilon_{\mathrm{vac}}\mathbf{1}_{3\times 3}$ in SI units as in Eq. (2.2.3)], and the elastic tensor is [see Eq. (C.2.6)]:

$$\hat{c} = \begin{pmatrix} c_{11} & c_{12} & c_{12} & 0 & 0 & 0 \\ c_{12} & c_{11} & c_{12} & 0 & 0 & 0 \\ c_{12} & c_{12} & c_{11} & 0 & 0 & 0 \\ 0 & 0 & 0 & c_{44} & 0 & 0 \\ 0 & 0 & 0 & 0 & c_{44} & 0 \\ 0 & 0 & 0 & 0 & 0 & c_{44} \end{pmatrix} , \tag{3.2.10}$$

with the GaAs parameters $c_{11} = 12.26 \times 10^{10}\,\mathrm{N/m^2}$, $c_{12} = 5.71 \times 10^{10}\,\mathrm{N/m^2}$, $c_{44} = 6.00 \times 10^{10}\,\mathrm{N/m^2}$. From those values in the wave equation, the longitudinal and transversal (isotropic-approximated) sound velocities are easily deduced: $v_l^2 = c_{11}/\rho$ and $v_t^2 = c_{44}/\rho$. Moreover, $\zeta = 0.9$ for the Rayleigh velocity $v_s = \zeta v_t$.

So, should one estimate a magnitude of the electron-phonon interaction (as in Sec. 3.1.2 for optical phonons) for the acoustic piezophonons on GaAs, we would write:

$$V_{\mathrm{ph}}^{\mathrm{PA}}(\mathbf{q},0) = \frac{2|\gamma_{\mathbf{q}}^{\mathrm{PA}}|^2}{\hbar v_s q} \sim \frac{e^2}{\overline{\varepsilon}_0 \varepsilon_{\mathrm{vac}}} \frac{e_{14}^2}{\varepsilon_0 \varepsilon_{\mathrm{vac}} c_{44}} , \tag{3.2.11}$$

which enters the calculation through the dimensionless product:

$$V_{\mathrm{ph}}^{\mathrm{PA}}(\mathbf{q},0)[-\Pi_0(\mathbf{q},0)] = p \frac{\alpha_{\mathrm{fs}}}{\overline{\varepsilon}_0} K^2 \frac{k_{\mathrm{F}}}{q} . \tag{3.2.12}$$

The proportionality constant p in this simple case is [see Eq. (3.2.6)]:

$$p = \frac{16}{a\zeta^6}[3\kappa_l\alpha^{-1}(1-\kappa_l) - f(1+2\kappa_t^2)(1-\kappa_t) - \zeta^2(1-f\kappa_t)]^2 \times \sin^2 2\theta_{\mathbf{q}} \approx 1.9 \sin^2 2\theta_{\mathbf{q}} \ . \tag{3.2.13}$$

Considering also the fact that $K^2 \approx 0.003$ for these parameters, we conclude that the static phonon-mediated electron-electron interaction for this substrate is negligible compared to the Coulomb repulsion.

In a polaron theory such as that developed for the optical phonons [61], we may write Eq. (3.1.7) as:

$$V_{\text{eff}}(\mathbf{q},\omega) = \frac{\frac{e^2}{2\bar{\varepsilon}_0\varepsilon_{\text{vac}}q} + \frac{2|\gamma_{\mathbf{q}}^{\text{PA}}|^2 v_s q}{\hbar(\omega^2 - v_s^2 q^2)}}{1 - \left[\frac{e^2}{2\bar{\varepsilon}_0\varepsilon_{\text{vac}}q} + \frac{2|\gamma_{\mathbf{q}}^{\text{PA}}|^2 v_s q}{\hbar(\omega^2 - v_s^2 q^2)}\right]\Pi_0(\mathbf{q},\omega)} \ . \tag{3.2.14}$$

In the static limit, with the parameters from above for monolayer graphene (or another material with a linearized electronic dispersion):

$$V_{\text{eff}}(\mathbf{q},\omega \simeq 0) = \frac{\left(\frac{\alpha_{\text{fs}}\hbar v_{\text{F}}}{\bar{\epsilon}_0} - \frac{\alpha_{\text{fs}}\hbar v_{\text{F}} p K^2}{\bar{\varepsilon}_0}\right)\frac{2\pi}{q}}{1 + \left(\frac{\alpha_{\text{fs}}\hbar v_{\text{F}}}{\bar{\epsilon}_0} - \frac{\alpha_{\text{fs}}\hbar v_{\text{F}} p K^2}{\bar{\varepsilon}_0}\right)\frac{2\pi}{q}\frac{2k_{\text{F}}}{\pi\hbar v_{\text{F}}}} \ , \tag{3.2.15}$$

one concludes that in the range of frequencies $\omega \ll \omega_{\mathbf{q}} = v_s q$, the only effect of the piezoelectric phonons is that of providing an extra source of screening to further renormalize the static dielectric constant exactly in the same way as has been shown for the optical Fröhlich phonons [61], since all interactions have the 2D Coulomb form $1/q$ in Eq. (3.2.15).

Finally, we note that the fact that piezoelectric effects in GaAs play a small role in the electron-electron interaction, is compatible with those effects being important in the carrier mobility [50] or in the interactions underlying SAW-based conveyor belts [38, 39].

3.2.3 General electron-piezoelectric phonon interaction

Even though most materials are either non-piezoelectric or their piezoelectric coupling constants are small enough (K^2 is 0.01 or even lower), it has been noticed [see Eq. (3.2.6)] that the piezoelectric vertex, which is proportional to the piezoelectric tensor, enters the effective interactions through a second order process. Therefore, a variation in this tensor of about an order of magnitude results in a variation of two orders of magnitude in the coupling parameters. Several works on electron-phonon interactions in piezoelectrics use other materials such as ZnO and AlN, whose associated piezoelectric fields are around 10 times stronger than those of GaAs [91], which increases the previous interaction by a factor of 100. But there exist piezoelectric materials whose coefficients are even an order of magnitude bigger than ZnO/AlN, for example $LiNbO_3$, $BaTiO_3$ or PZT (lead zirconate titanate, $PbTi_xZr_{1-x}O_3$), among many oxides with the perovskite structure and formula ABO_3. These compounds tend to show ferroelectric properties, and are sometimes reminiscent of the layers between CuO_2 planes in cuprate high-temperature superconductors (see Table 3.1).

Since it is no longer feasible to neglect the e_{ijk} terms in the wave equations for these hard piezoelectrics (as explained in Sec. 2.3.1), one must solve the wave equation with an exact solution [of the type of Eq. (2.1.5)] with an arbitrary factor $C_{\mathbf{q}}$, to be quantized as in the GaAs case, but based on an exact energy equation including all the fields [see Eqs. (F.3.1),(F.3.2)]:

$$u_a(\mathbf{r},t) = C_{\mathbf{q}} \sum_{n=1}^{4} C_n A_a^{(n)} e^{ikb_3^{(n)}z} \exp\left[ik(\mathbf{b}\cdot\mathbf{R} - vt)\right] \ , \tag{3.2.16}$$

$$\langle E_{\mathbf{q}} \rangle = \left\langle \int_{\text{average A}} d\mathbf{R} \int_{-\infty}^{0} dz \frac{dE}{dV}(\mathbf{r},t) \right\rangle = h\omega_{\mathbf{q}} = \hbar v_s(\mathbf{q}) q \equiv F(C_{\mathbf{q}}) \ ,$$

$$\frac{dE}{dV} = \frac{1}{2}\left[(\ddot{u}_x^2 + \ddot{u}_y^2 + \ddot{u}_z^2) + u_{ij}T_{ij} + \mathbf{D}\cdot\mathbf{E}\right] \ . \tag{3.2.17}$$

To determine $C_{\mathbf{q}}$ here, it is useful for computational purposes to note that the average kinetic energy is equal to the potential energy, as will be seen in Eq. (3.3.4).

In order to proceed to obtain the pure quantum-mechanical interaction, it is better to adopt an alternative approach involving useful dielectric and response functions, so that the matrix element for the interaction can be expressed from directly measurable quantities (not having large uncertainties like the tensors $\hat{e}, \hat{c}$) for the coupling. The numerically approximated parameter $p\,K^2$ [Eqs. (3.2.14), (3.2.15)] becomes K_R^2 (with p exactly one) when K is replaced by K_R.

3.3 Exact electron-SAW interaction

We return to the general scenario (see Fig. 2.1) but considering the possibility of flat electrodes at $z = 0^+$, which supply no mechanical stresses. The purpose of this section is to show that the general interaction between the propagating piezoelectric SAWs and an electron at the surface can be described with a Hamiltonian of the form (3.1.1) with (SI units are used throughout the present section, as is typical for piezoelectrics)

$$\begin{aligned} \omega_{\mathbf{q}} &= v_s(\theta)|\mathbf{q}| \ , \\ \gamma_{\mathbf{q}}^{\mathrm{PA}} &= \frac{K_R(\theta)}{\sqrt{2}} \left[\frac{v_s(\theta)\hbar e^2}{(\tilde{\varepsilon}_{\mathrm{HF}}(\theta)+1)\varepsilon_{\mathrm{vac}}} \right]^{1/2} \ , \end{aligned} \tag{3.3.1}$$

where $\mathbf{q} := q\,[\cos(\theta), \sin(\theta)]$ and $\varepsilon_{\mathrm{vac}}$ is the air or vacuum electric permittivity. The piezoelectric specific parameters are $v_s(\theta)$, the piezoelectric SAW velocity; $0 \leq K_R^2(\theta) < 1$, the *SAW electromechanical coupling coefficient*; and $\tilde{\varepsilon}_{\mathrm{HF}}(\theta) := \lim_{\omega\to\infty} \tilde{\varepsilon}(\mathbf{q}/\omega)$ (with $\omega \to \infty$ within the acoustic frequency scale), the high-frequency (HF) limit of the *piezoelectric surface permittivity*, as in Sec. 2.4 (see Refs. [18, 19]). They all depend on the propagation direction of the SAW, as the notation suggests.

3.3.1 Hamiltonian and interaction vertex

The linear equations of piezoelectricity, Eqs. (F.1.1), can be derived from a Lagrangian (see Ref. [92]):

$$L\left[u_j,\varphi\right]=\frac{1}{2}\int d^3\mathbf{r}\left[\rho\dot{u}_i\dot{u}_i-c_{ijkl}u_{i,j}u_{k,l}-2e_{ijk}\varphi_{,i}u_{j,k}+\varepsilon_{ij}\varepsilon_{\mathrm{vac}}\varphi_{,i}\varphi_{,j}\right]\ , \tag{3.3.2}$$

where it has been written the subindex "$_{,j}$" stands for $\partial/\partial x_j$, while $\dot{u}_i := \partial u_i/\partial t$. The canonical momentum to φ is zero, so that the system is constrained. The Hamiltonian is then:

$$H\left[u_j,\varphi\right]=\frac{1}{2}\int d^3\mathbf{r}\left(\rho\dot{u}_i\dot{u}_i+c_{ijkl}u_{i,j}u_{k,l}+\varepsilon_{ij}\varepsilon_{\mathrm{vac}}\varphi_{,i}\varphi_{,j}\right). \tag{3.3.3}$$

For a given harmonic propagating piezoelectric SAW without surface charges, i.e., a wave with the form of $\mathrm{Re}\,u_a(\mathbf{r},z,t)$ from Eqs. (2.1.5), (2.1.6) fulfilling the equations of motion Eqs. (F.1.1) and boundary conditions Eqs. (2.1.7), (2.3.4) with $\sigma(0)=0$, it is straightforward to show that the kinetic energy [first term in Eq. (3.3.3), coming exclusively from elastic vibrations in the substrate] is the same as the potential energy [last two terms in Eq. (3.3.3), containing contributions from the elastic deformations and the electrostatic energy stored both in the substrate and in free space]. We just need to multiply the wave terms in Eq. (F.1.1) by u_i and to integrate by parts, and obtain a sort of virial theorem for piezoelectric termodynamics, that is:

$$\int d^3\mathbf{r}\left\langle T_{ij}u_{ij}+E_iD_i\right\rangle=\int d^3\mathbf{r}\ \frac{1}{2}\left\langle\rho\dot{u}_i^2\right\rangle\ . \tag{3.3.4}$$

On the other hand [18], for the interval $0<v_s(\theta)<v_L(\theta)$, the positivity of the kinetic and potential energies gives $\partial\tilde{\varepsilon}(\mathbf{k}/\omega)/\partial\omega>0$. For these kind of waves one has the following equation, obtained easily from the definition of a susceptance function and its relation to the total energy and surface

permittivity [18] [when $1+\tilde{\varepsilon}(\mathbf{k}/\omega)=0$]:

$$H_{\rm harm}=\frac{1}{4}Ak\omega\frac{\partial\tilde{\varepsilon}(\mathbf{k}/\omega)\varepsilon_{\rm vac}}{\partial\omega}|\varphi_0|^2=\frac{1}{2}Ak|\varphi_0|^2\frac{(\tilde{\varepsilon}_{\rm HF}(\theta)+1)\varepsilon_{\rm vac}}{K_R^2(\theta)}\ , \quad (3.3.5)$$

where A is the area of the sample, $\varphi_0:=C_n\alpha_4^{(n)}$ is the amplitude of the electric potential at the interface [see Eq. (2.1.5)], and the high-frequency limit $\tilde{\varepsilon}_{\rm HF}(\theta):=\lim_{\omega\to\infty}\tilde{\varepsilon}(\mathbf{k}/\omega)$ has been introduced together with the *SAW electromechanical coupling coefficient*, $K_R(\theta)$, through the relation at $1+\tilde{\varepsilon}(\mathbf{k}/\omega)=0$ [see Eq. (2.4.2)]:

$$\frac{K_R^2(\theta)/2}{\tilde{\varepsilon}_{\rm HF}(\theta)+1}=\left[\omega\frac{\partial\tilde{\varepsilon}(\mathbf{k}/\omega)}{\partial\omega}\right]^{-1}\ . \quad (3.3.6)$$

The electrons of the graphene sheet (or any other charged quasiparticle coming, for example, from a two-dimensional structure deposited at the piezoelectric substrate) feel the electric potential of the piezoelectric SAW. The interaction is then given by the total potential at the position of the electron:

$$V_{\rm PA}(\mathbf{R})=-e\,\varphi(\mathbf{R},0,t=0)\ . \quad (3.3.7)$$

On the other hand, the one-phonon normalization means that φ_0 from Eq. (3.3.5) should be chosen so that $H_{\rm harm}=\hbar\omega=\hbar v_s(\theta)k$, and thus one finally gets Eq. (3.1.1) with the vertex in Eq. (3.3.1) .

3.3.2 Boundedness of K_R^2

To prove rigorously the general bound $0\le K_R^2(\theta)<1$, it is necessary to recover the formalism of response functions in Sec. 2.4.2, allowing ideal electrodes, parallel to the y-axis, operating on top of the piezoelectric substrate. There, processes which turn on a given final charge distribution $\sigma(x)$ were considered, either adiabatic or instantaneous, each one with supplied energies $\Delta U_{\rm ad},\ \Delta U_{\rm inst}$, the former energy being smaller than the latter.

After the sudden charge, i.e., at $t>0$, the time evolution and relaxation

of the potential are, as follows from Eqs. (2.4.15) and (2.4.16):

$$\varphi(x,t) = \int dx'\sigma(x') \left[\gamma_\infty(x-x') + \int_0^t dt'\phi(x-x',t-t')\right] \xrightarrow{t\to\infty} \int dx'\sigma(x')\gamma_0(x-x') \ , \tag{3.3.8}$$

this relaxed field being the same as that obtained after the adiabatic process leading to the same charge distribution.

The space Fourier, time Fourier-Laplace transform of this potential is:

$$\varphi(k,\omega) := \int dx \int_0^\infty dt\, e^{i(\omega t-kx)}\varphi(x,t) = \frac{i\sigma(k)}{\omega+i\eta}\gamma(k,\omega) \ , \tag{3.3.9}$$

where the change $\omega \to \omega + i\eta$ ($\eta \equiv 0^+$) is made to ensure convergence.

Since $\gamma(k,\omega)$ has poles at the Rayleigh-wave condition [Eq. (2.3.5)], one can isolate their contribution $\varphi_{\rm RW}(x,t)$ to $\varphi(x,t)$. It is:

$$\varphi_{\rm RW}(k,\omega) := \frac{i\sigma(k)}{|k|}\frac{K_R^2/2}{(\tilde{\varepsilon}_{\rm HF}+1)\varepsilon_{\rm vac}}\left(\frac{1}{\omega-\omega_k+i\eta}+\frac{1}{\omega+\omega_k+i\eta}\right) \ , \tag{3.3.10}$$

where $\omega_k = vk$ and the two terms come from the two identical SAWs propagating to the right and to the left. A small 0^+ has been added to ensure that the poles of the admittance are in the lower complex-ω half-plane. Inverting to get the spacetime behavior, one obtains two dispersionless propagating SAWs:

$$\varphi_{\rm RW}(x,t) = \frac{K_R^2}{2}\left[\varphi(x-vt,0^+)+\varphi(x+vt,0^+)\right] \ , \tag{3.3.11}$$

where $\varphi(x\pm vt,0^+) = \int (dk/2\pi)\, e^{ik(x\pm vt)}\gamma_\infty(k)\sigma(k)$ [see Eq. (3.3.8)]. The energy carried by these two pulses is, using Eq. (2.4.25):

$$\Delta U_{\rm RW} = \sqrt{A}\frac{K_R^2/2}{(\tilde{\varepsilon}_{\rm HF}+1)\varepsilon_{\rm vac}}\int \frac{dk}{2\pi}\frac{|\sigma(k)|^2}{|k|} \ , \tag{3.3.12}$$

which is the energy stored in each traveling SAW, i.e. $\Delta U_{\rm RW} = K_R^2\,\Delta U_{\rm inst}$

from Eq. (2.4.19). Since we have at our disposal no more than $\Delta U_{\rm inst} - \Delta U_{\rm ad} > 0$, the condition $\Delta U_{\rm RW} < \Delta U_{\rm inst} - \Delta U_{\rm ad}$ must be fulfilled. From Eqs. (2.4.18)-(2.4.20) one concludes that:

$$K_R^2 \leq \frac{\tilde{\varepsilon}_{\rm LF} - \tilde{\varepsilon}_{\rm HF}}{\tilde{\varepsilon}_{\rm LF} + 1} < 1 \ . \tag{3.3.13}$$

Actually, this bound is slightly lower than 1.

One can obtain an alternative definition for the electromechanical coupling coefficient in this scenario, as the ratio of the efficiency of conversion between electric and acoustic energy in a piezoelectric material:

$$K_R^2 = \frac{\Delta U_{\rm RW}}{\Delta U_{\rm inst}} \ , \tag{3.3.14}$$

together with a third possible definition, all being equivalent. This third definition follows by applying Ingebrigsten's approximation [Eq. (2.4.1)], the definition in Eq. (2.4.2), and the fact that $v_0, v_s, v_{\varphi=0}$ are very close to each other [18]. This last definition is related to the piezoelectric-stiffening effect, as described in App. F.2, measuring the change in SAW velocities $\Delta v = v_s - v_{\varphi=0}$ due to the piezoelectric effect:

$$K_R^2 \approxeq \frac{2}{1+\varepsilon_p^{-1}} \frac{v_0 - v_{\varphi=0}}{v_{\varphi=0}} \approx \frac{2(v_s - v_{\varphi=0})}{v_{\varphi=0}} \ , \tag{3.3.15}$$

the second inequality being valid just when the relative dielectric constant of the piezoelectric material is much bigger than that of the air.

3.4 Numerical examples

Numerical values for the electromechanical coupling coefficient in many materials and directions can be found in the general literature on piezoelectricity. That is not the case for the less-studied electron-phonon vertex. Luckily, we can prove the general formula in Eq. (4.1.2), so that knowledge of the former coefficient is sufficient (together with knowledge of the sound

velocity and material dielectric constants) to obtain the latter. For the sake of completeness, we copy a few values from Ref. [56] in Table 3.1.

The numerical examples which we discuss in this section can be shown to agree with the approximation in Eq. (3.3.15). This represents an important simplification because the general formulæ involve complicated functions of many tensor components coming from the solution of the Christoffel equations. To compute the exact coupling in any direction in an arbitrary material, it is necessary to resort to numerical methods, as those used to find the SAW solutions.

Material (class)	Propagation	Wave	K_R
$Bi_{12}GeO_{20}$ (Cubic)	[1 1 0]	longitudinal	0
$Bi_{12}GeO_{20}$ (Cubic)	[1 1 0]	[0 0 1]- shear	$\sqrt{\frac{e_{41}^2}{c_{44}\varepsilon_{11}}} = 0.338$
$Bi_{12}GeO_{20}$ (Cubic)	[1 1 0]	$[\bar{1}\ 1\ 0]$-shear	0
CdS (6mm)	Z-axis	longitudinal	0
CdS (6mm)	Z-axis	shear	$\sqrt{\frac{e_{33}^2}{c_{33}\varepsilon_{33}}} = 0.156$
CdS (6mm)	X-axis	Z-shear	0
CdS (6mm)	X-axis	Y-shear	$\sqrt{\frac{e_{15}^2}{c_{44}\varepsilon_{11}}} = 0.192$
$LiNbO_3$ (3m)	Z-axis	longitudinal	$\sqrt{\frac{e_{33}^2}{c_{33}\varepsilon_{33}}} = 0.163$
$LiNbO_3$ (3m)	Z-axis	shear	0
ZnO (6mm)	Z-axis	longitudinal	$\sqrt{\frac{e_{33}^2}{c_{33}\varepsilon_{33}}} = 0.302$
ZnO (6mm)	Z-axis	shear	0
ZnO (6mm)	X-axis	Z-shear	$\sqrt{\frac{e_{15}^2}{c_{44}\varepsilon_{11}}} = 0.268$
ZnO (6mm)	X-axis	Y-shear	0

Table 3.1: Selected values of a few electromechanical coupling constants in several materials and specific direction propagations, which can be given easily in terms of a ratio $\frac{e_{\lambda\mu}^2}{c_{\nu\xi}\varepsilon_{ij}}$ for some $\lambda, \mu, \nu, \xi = 1, ..., 6$ and $i, j = 1, 2, 3$. Taken from Ref. [56].

The point group of ZnO and AlN gives isotropic couplings with the Z-cut and therefore isotropic sound velocities. On the other hand, their X and Y-cuts are equivalent. This is not the case, for example, in $LiNbO_3$, whose

$K_R^2(\theta)$ and vertex values in the X,Y and Z-cuts are shown in Fig. 3.2. For some graphs of the velocities in different cuts in this latter material, see Fig. 2.2 and Ref. [55]. Recall that the cut terminology refers to the lattice axis perpendicular to the surface. The reader may review the subsection "Cut terminology" in Sec. 2.1 or Refs. [93, 94] if not familiar with that terminology. In the case of GaAs, an excellent approximation for the vertex is given by the sinusoidal expression in Eq. (3.2.6).

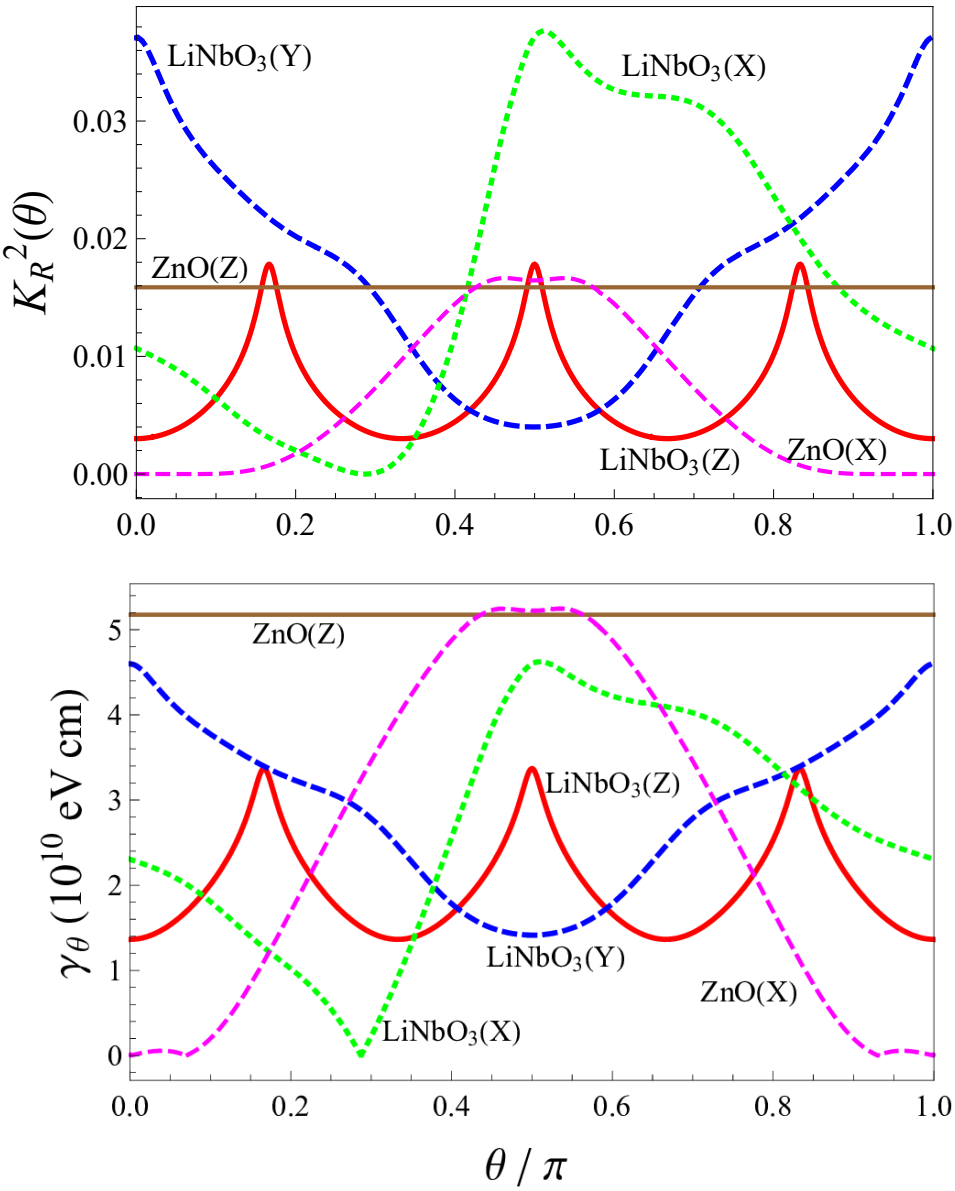

Figure 3.2: Some representative magnitudes for SAW phonons and for two different materials with different symmetries ($LiNbO_3$ and ZnO) as a function of the angle within the crystal plane parallel to the cut plane, in the X-Y-Z-cuts (denoted between parentheses) chosen for all. For the Z-Cut (X-Cut/Y-Cut), the 0 angle correspond to the x-axis (y-axis/z-axis) moving forward towards the y-axis (z-axis/x-axis). Upper: Electromechanical coupling coefficient. Lower: Electron-phonon vertex. The plots are obtained by processing data for the elastic, dielectric and piezoelectric tensors taken from Refs. [18, 49, 56] and references therein.

Chapter 4

SAW-induced many-body effects on electronic layers

4.1 Piezoelectric 2D electron-phonon Hamiltonian

The present chapter aims to clarify the role of acoustic piezoelectric surface phonons, which form the microscopic quanta of SAWs [95], in graphene-on-piezomaterial structures. It has been shown in the previous chapter (as well as in Ref. [18]) that there exists a relation between the amplitude of the electric potential at the surface of a piezoelectric material, $\varphi_0 = \varphi(\mathbf{q},\omega)$, and the total energy $H_{\rm harm}$ [see Eq. (3.3.5)]. Hence, a standard quantization procedure (see Sec. 3.3.1) showed that the interaction between a single electron and the spontaneous piezoelectric Rayleigh waves in that surface can be written as:

$$H_{\text{e-ph}}^{\text{PA}} = \frac{1}{\sqrt{A}} \sum_{\mathbf{k},\mathbf{q},\sigma} \gamma_{\mathbf{q}}^{\text{PA}}\, a_{\mathbf{k}+\mathbf{q},\sigma}^{\dagger} a_{\mathbf{k},\sigma} b_{\mathbf{q}} + \text{H.c.}\ , \tag{4.1.1}$$

$$\gamma_{\mathbf{q}}^{\text{PA}} = \frac{K_R(\theta)}{2} \sqrt{\frac{\hbar e^2 v_s(\theta)}{\overline{\varepsilon}_{\text{HF}}(\theta)\varepsilon_{\text{vac}}}}\ , \tag{4.1.2}$$

where A is the area of the sample, $a_{\mathbf{k},\sigma}, a^\dagger_{\mathbf{k},\sigma}$ are the electron operators with $\sigma = \pm$ for the electron spin, $b_{\mathbf{k}}, b^\dagger_{\mathbf{k}}$ are the piezoelectric-phonon operators, and $\bar{\varepsilon}_{\mathrm{HF}}(\theta) := [\tilde{\varepsilon}_{\mathrm{HF}}(\theta) + 1]/2$.

4.1.1 Layer containing an electron gas

When a two-dimensional material such as graphene is placed onto a piezoelectric substrate (see Sec. 1.1.1), the validity of the shown interaction Hamiltonian (4.1.2) requires two further assumptions: first, the 2DEG or multilayered graphene sample should be thin enough so that in Eq. (2.1.6), $k_{\max} d \ll 1$, where d is the width of the sample and $k_{\max}$ is the maximum allowed phonon momentum [see the comments after Eq. (3.1.4)]. And second, this maximum momentum should be sufficiently small for the classical piezo-elasticity theory, as shown in Eqs. (F.1.1), to remain valid. If one assumes a maximum momentum on the order of $k_F = \sqrt{\pi n} \sim 10^6 - 10^7\,\mathrm{cm}^{-1}$, this last restriction is not violated for the usual electronic densities n in doped semiconductors.

The resulting total Hamiltonian for the combined system of the 2D electron gas and the piezoelectric Rayleigh phonons is:

$$H = \sum_{\mathbf{k},\sigma} E_{\mathbf{k}} a^\dagger_{\mathbf{k},\sigma} a_{\mathbf{k},\sigma} + \hbar \sum_{\mathbf{q}} \omega_{\mathbf{q}}\, b^\dagger_{\mathbf{q}} b_{\mathbf{q}} + H^{\mathrm{PA}}_{\text{e-ph}} + \frac{1}{2A} \sum_{\mathbf{q}} v^{(0)}_{\mathbf{q}} \rho(\mathbf{q}) \rho(-\mathbf{q}) \;, \quad (4.1.3)$$

where $E_{\mathbf{k}}$ is the electron energy for a 2D wave vector $\mathbf{k}$ (see Sec. A.2), $\omega_{\mathbf{q}} = v_s(\theta) q$ is the dispersion relation for the piezoelectric SAW phonon of 2D wave vector $\mathbf{q}$, $v_s(\theta)$ is the SAW propagation velocity, $v^{(0)}_{\mathbf{q}} = e^2/2\bar{\varepsilon}_{\mathrm{HF}}\varepsilon_{\mathrm{vac}} q$, and $\rho(\mathbf{q}) = \sum_{\mathbf{k},\sigma} a^\dagger_{\mathbf{k}+\mathbf{q},\sigma} a_{\mathbf{k},\sigma}$ is the Fourier transform of the electron density. The derivation proceeds exactly like that for the total Hamiltonian of a 2D electron gas with optical phonons (see Sec. 3.1.2).

The sound velocities $v_s(\theta)$ of piezoelectric acoustic phonons are anisotropic (they depend on a direction angle θ) and typically two or three orders of magnitude smaller than the Fermi velocity v_F in graphene or another 2DEG, which yields a relatively low value of the maximum acoustic frequency. In

fact, in the derivation of any piezoelectric electron-phonon interaction, it is taken into account that the Fröhlich optical phonons (slower than the electrons) respond instantaneously in the time scales of the acoustic phonons by implicitly taking the effective dielectric constants of the problem as the static ones.

Thus the dielectric screening effects due to the substrate can be described by its static (also anisotropic) dielectric constant $\varepsilon_0(\theta)$. This constant combines both core excitons and optical phonons as well as any high-frequency (instantaneous) polarization forces which screen the fields created by the piezoelectric acoustic phonons [61]. Then, in the graphene case, the Fourier transform of the repulsive Coulomb interaction over the substrate reads the same, with $\overline{\varepsilon}_{\rm HF}(\theta)$ (see Sec. 2.4.1) replaced by $\overline{\varepsilon}_0$,

$$v_{\mathbf{q}}^{(0)} = \frac{e^2}{2\overline{\varepsilon}_0(\theta)\varepsilon_{\rm vac} q} \,, \tag{4.1.4}$$

where $\overline{\varepsilon}_0(\theta) = \frac{\varepsilon_0(\theta)+1}{2}$ is the effective (relative) dielectric constant at the substrate-air interface [29], and $q = |\mathbf{q}|$ with $\mathbf{q} = (q_x, q_y)$ and $\theta \equiv \arg(q_x + iq_y)$. The interaction between the graphene electrons and the piezoelectric acoustic (PA) phonons is therefore given by the former $H_{\text{e-ph}}^{\rm PA}$ in Eq. (4.1.1) with:

$$\gamma_{\mathbf{q}}^{\rm PA} = \frac{K_R(\theta)}{2}\left[\frac{\hbar e^2 v_s(\theta)}{\overline{\varepsilon}_0(\theta)\varepsilon_{\rm vac}}\right]^{\frac{1}{2}} = K_R(\theta)\left[\frac{\pi\alpha_{\rm fs}\hbar^2 v_F v_s(\theta)}{\overline{\varepsilon}_0(\theta)}\right]^{\frac{1}{2}} \,. \tag{4.1.5}$$

Here $\alpha_{\rm fs} = \frac{e^2}{4\pi\varepsilon_{\rm vac}\hbar v_F} \simeq 2.2$ in graphene, and $a_{\mathbf{k},\sigma}$ is the Fermi operator for an electron of the graphene layer with wave vector $\hbar\mathbf{k}$, spin-valley-cone index σ, and energy

$$E_{k\sigma} = \hbar s v_F k \,, \tag{4.1.6}$$

where $s = \pm 1$ is the cone index. It is to be understood that, in the absence of the substrate, we are in the usual Fermi-liquid regime of (doped) graphene.

4.1.2 Effective electron-electron interaction

The coupling in Eq. (4.1.5) enables a phonon-mediated electron-electron interaction

$$V_{\rm ph}^{\rm PA}(\mathbf{q},\omega) = |\gamma_{\mathbf{q}}^{\rm PA}|^2\, G_0^{\rm PA}(\mathbf{q},\omega)\ , \tag{4.1.7}$$

where

$$G_0^{\rm PA}(\mathbf{q},\omega) = \frac{2\omega_{\mathbf{q}}/\hbar}{\omega^2-\omega_{\mathbf{q}}^2+i0^+} \tag{4.1.8}$$

denotes the bare propagator of the surface acoustic phonons. This interaction admits a diagrammatic representation, as shown in Fig. 3.1 and as is standard for electron-phonon couplings.

By including screening effects due to the charge carriers in graphene, as described by the polarization $\Pi_0(q,\omega)$ (see Refs. [77, 96]), one can define the total effective electron-electron interaction in terms of an anisotropic dielectric function $\varepsilon(\mathbf{q},\omega)$:

$$\begin{aligned} V_{\rm eff}(\mathbf{q},\omega) &= \frac{e^2}{2\varepsilon(\mathbf{q},\omega)\varepsilon_{\rm vac}q} \\ &= \frac{v_{\mathbf{q}}^{(0)} + V_{\rm ph}^{\rm PA}(\mathbf{q},\omega)}{1-\left[v_{\mathbf{q}}^{(0)} + V_{\rm ph}^{\rm PA}(\mathbf{q},\omega)\right]\,\Pi_0(q,\omega)}\ . \end{aligned} \tag{4.1.9}$$

For frequencies small in the scale of the acoustic phonons [or the Bloch-Grüneisen temperature $k_B T_{\rm BG} := 2\hbar v_s k_F$, see Eq. (5.2.14)], the bare electron-phonon-electron interaction contributes to the long-range part of the total interaction with a $\mathbf{q}$ dependence similar to that of the Coulomb repulsion:

$$V_{\rm ph}^{\rm PA}(\mathbf{q},\omega\simeq 0) = |\gamma_{\mathbf{q}}^{\rm PA}|^2 G_0^{\rm PA}(\mathbf{q},\omega\simeq 0) = -\frac{2|\gamma_{\mathbf{q}}^{\rm PA}|^2}{\hbar v_s q}\ . \tag{4.1.10}$$

Note that, given the fact that $\gamma_{\mathbf{q}}^{\rm PA}$ is q-independent [see Eq. (4.1.5)], here it is the acoustic-phonon propagator $G_0^{\rm PA}(\mathbf{q},\omega\simeq 0)$ that introduces the coulombic long-range dependence in q via the dispersion of the modes. In Sec. 4.2.1, it will be shown that a similar final q dependence has a different origin in the case of optical phonons.

In this low-frequency limit, $\Pi_0(\mathbf{q}, \omega \simeq 0) \simeq -D(E_F) = -2k_F/\pi\hbar v_F$ for monolayer graphene [77], or $\Pi_0(\mathbf{q}, \omega \simeq 0) \simeq -D(E_F) = -m/2\pi\hbar^2$ for a 2DEG with effective mass m [97]. These two static limits are exact for $q < 2k_F$. In the graphene case, by defining:

$$\varepsilon_{\rm RPA}(\mathbf{q}, \omega) = 1 - v_{\mathbf{q}}^{(0)} \, \Pi_0(q, \omega) \, , \tag{4.1.11}$$

one obtains, for $\omega \to 0$:

$$\varepsilon_{\rm RPA}(\mathbf{q}, \omega) \simeq \varepsilon_{\rm RPA}(\mathbf{q}, 0) \, , \tag{4.1.12}$$

where the static dielectric function satisfies:

$$\varepsilon_{\rm RPA}(\mathbf{q}, 0) = 1 + \frac{k_{\rm TF}(\theta)}{q} \tag{4.1.13}$$

for $q < 2k_F$, where:

$$k_{\rm TF} = \frac{4\alpha_{\rm fs} k_F}{\bar{\varepsilon}_0(\theta)} \tag{4.1.14}$$

is the (anisotropic) Thomas-Fermi wave vector and k_F the Fermi wave vector, the factor of 4 accounting for spin-valley degeneracy.

We may also define the renormalized phonon propagator:

$$\tilde{G}^{\rm PA}(\mathbf{q}, \omega) = \frac{G_0^{\rm PA}(\mathbf{q}, \omega)}{1 - \frac{V_{\rm ph}^{\rm PA}(\mathbf{q}, \omega) \Pi_0(q, \omega)}{\varepsilon_{\rm RPA}(\mathbf{q}, \omega)}} \, . \tag{4.1.15}$$

Then, Eq. (4.1.9) can be decomposed into an electron-electron and an electron-phonon part [61, 62]. Some straightforward algebra leads to:

$$V_{\rm eff}(\mathbf{q}, \omega) = \frac{v_{\mathbf{q}}^{(0)}}{\varepsilon_{\rm RPA}(\mathbf{q}, \omega)} + \left| \frac{\gamma_{\mathbf{q}}^{\rm PA}}{\varepsilon_{\rm RPA}(\mathbf{q}, \omega)} \right|^2 \tilde{G}^{\rm PA}(\mathbf{q}, \omega) \, , \tag{4.1.16}$$

as shown diagrammatically in Fig. 4.1.

It is desirable to emphasize the importance of the electronic screening of the electron-phonon vertex as shown in Eq. (4.1.16). This will strongly

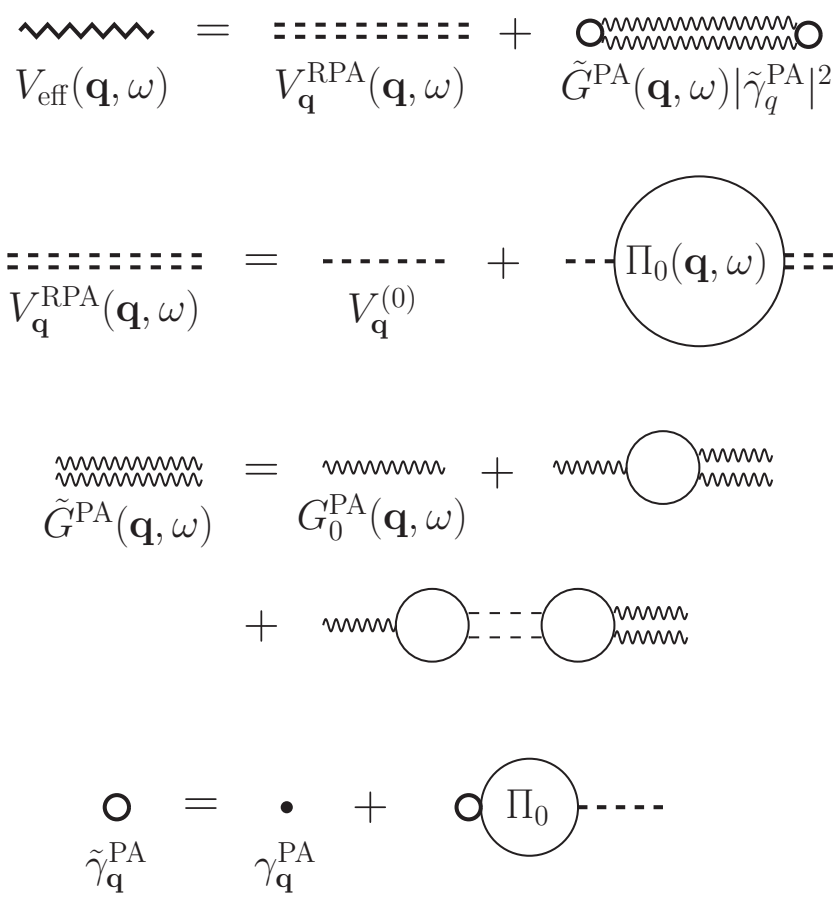

Figure 4.1: Diagrammatics of the screening of the electron-phonon vertex in a metallic system. Within an equivalent RPA scheme, the effective electron-electron interaction is separated into an electron-electron Coulombic part and an electron-phonon part with a screened vertex and renormalized phonon propagator. In the second line, $V^{\rm RPA}(\mathbf{q},\omega) = v_{\mathbf{q}}^{(0)}\left[\varepsilon_{\rm RPA}(\mathbf{q},\omega)\right]^{-1}$ is the first term of Eq. (4.1.16). In the fourth line, $\tilde{\gamma}_{\mathbf{q}}^{\rm PA} = \gamma_{\mathbf{q}}^{\rm PA}\left[\varepsilon_{\rm RPA}(\mathbf{q},\omega)\right]^{-1}$ is the screened vertex in the same equation.

influence the role of scattering processes involving low values of q, and is sometimes not well included in the literature, a common mistake being the placement of the screening outside the square of the second term in Eq. (4.1.16).

In the limit of low frequencies, $\omega \simeq 0$, there can be no effective attraction for electrons close to the Fermi surface. Specifically, we will prove that the following inequality [see Eq. (3.3.13)] is satisfied:

$$\frac{-V_{\rm ph}^{\rm PA}(\mathbf{q}, \omega \simeq 0)}{v_{\mathbf{q}}^{(0)}} = K_R^2(\theta) < 1 \ , \tag{4.1.17}$$

which is an important result of this thesis.

4.2 Basic input parameters of the theory and main approximations

Given the parameters $K_R(\theta)$, $v_s(\theta)$ and $\overline{\varepsilon}_0(\theta)$, the electron-phonon interaction $\gamma_{\mathbf{q}}^{\rm PA}(\theta)$ is computed from Eq. (4.1.5). A dimensionless parameter $\lambda_{\text{e-ph}}(\theta)$ characterizing the strength of the coupling of Eqs. (4.1.5), (4.1.10) can be obtained from multiplying the resulting effective interaction in Eq. (4.1.7) at $q = k_F$ by the density of states at the Fermi energy:

$$D(E_F) = -\Pi_0(k_F, 0) = \frac{2k_F}{\pi\hbar v_F} \, , \tag{4.2.1}$$

which leads to:

$$\lambda_{\text{e-ph}}(\theta) \equiv V_{\rm ph}^{\rm PA}(k_F\hat{\mathbf{q}}, 0)\, \Pi_0(k_F, 0) = \frac{4}{\pi\hbar^2 v_s(\theta) v_F} |\gamma_{\mathbf{q}}^{\rm PA}|^2 = 4K_R^2(\theta) r_s(\theta) \ , \tag{4.2.2}$$

where $\hat{\mathbf{q}} = \mathbf{q}/q$ and the parameter

$$r_s(\theta) \equiv \frac{\alpha_{\rm fs}}{\overline{\varepsilon}_0(\theta)} \tag{4.2.3}$$

characterizes the ratio between the interaction and kinetic energies (as in the Winger-Seitz theory [64]). This yields for the ratio between the piezoelectric interaction and the residual static Coulomb repulsion precisely the electromechanical coupling coefficient $K_R^2(\theta)$, characteristic of each piezoelectric material, that can be measured in SAW experiments:

$$\frac{\lambda_{\text{e-ph}}}{\lambda_{\text{e-e}}} = K_R^2 \ , \tag{4.2.4}$$

where

$$\lambda_{\text{e-e}}(\theta) = v^{(0)}_{k_F\hat{\mathbf{q}}}\,\Pi(k_F,0) = \frac{4\alpha_{\text{fs}}}{\overline{\varepsilon}_0(\theta)} = 4r_s(\theta) \tag{4.2.5}$$

is the dimensionless electron-electron coupling strength in substrate-screened graphene. The same parameter for the Fröhlich optical phonons would be $\lambda_{\text{e-op}} = 4\alpha_{\text{fs}}({\overline{\varepsilon}_\infty}^{-1} - {\overline{\varepsilon}_0}^{-1})$, as will be seen in Sec. 4.2.1.

Some angle-averaged values for selected representative materials, as taken from Refs. [18, 49, 56], are summarized in Table 4.1. Recall that roughly $K_R^2 \sim \frac{\hat{e}^2}{\hat{c}\epsilon_0}$, where $\hat{e}$ is a value for the piezoelectric tensor and $\hat{c}$ for the elastic tensor [30]. For example, the materials considered in Ref. [42], namely ZnO and AlN, have associated piezoelectric tensors that are much larger than those of the widely used GaAs [91], which increases the electron-phonon coupling by more than one order of magnitude. Despite being more piezoelectric, the dielectric tensors in the strongest ferroelectrics are so high that the interaction decreases [but not the ratio to the highly screened Coulomb repulsion; see Eq. (4.2.4)].

We keep the approximations made in the vertex (4.1.5) (flat interface and long wavelengths compared with the lattice spacing), which is in any case more accurate than those used in the previous literature on piezoelectric phonons. In the present work, and as in the previous literature, we do not take into account any possible deformation or influence of the geometrical details of the interface in the graphene sheet. Many parameters are used as well as if they were isotropic by employing an angle-averaging procedure (as shown in the Table 4.1) to give some exact analytical results mentioned below.

Material	Cut	K_R^2	$\bar{\varepsilon}_0$	$v_s(\frac{\text{cm}}{\text{s}})$	$\lvert\gamma_{\mathbf{q}}^{\text{PA}}\rvert^2$ (eVcm)^2	$\lambda_{\text{e-ph}}$	$4r_s$
GaAs (cubic)	X-Y-Z	0.0015	6.9	2.70×10^5	1.71×10^{-20}	0.0019	1.3
ZnO (6mm)	Z-Cut	0.016	4.8	2.71×10^5	2.70×10^{-19}	0.029	1.8
ZnO (6mm)	X-Cut	0.0064	4.8	2.63×10^5	6.60×10^{-20}	0.0074	1.8
AlN (6mm)	Z-Cut	0.0026	5.0	5.85×10^5	9.18×10^{-20}	0.0046	1.8
AlN (6mm)	X-Cut	0.0048	5.0	5.81×10^5	1.66×10^{-19}	0.0084	1.8
$LiNbO_3$ (3m)	Z-Cut	0.0068	19	3.85×10^5	4.25×10^{-20}	0.0032	0.46
$LiNbO_3$ (3m)	Y-Cut	0.017	20	3.59×10^5	9.35×10^{-20}	0.0077	0.44
$LiNbO_3$ (3m)	X-Cut	0.019	20	3.60×10^5	9.80×10^{-20}	0.0080	0.44
PZT-4 (6mm)	Z-Cut	0.027	350	2.26×10^5	5.37×10^{-21}	7.0×10^{-4}	0.025
PZT-4 (6mm)	X-Cut	0.0021	350	1.80×10^5	3.17×10^{-22}	5.2×10^{-5}	0.025

Table 4.1: Angle-averaged values of the electromechanical coupling coefficient K_R^2 appearing in Eq. (4.1.5), the effective dielectric constant $\bar{\varepsilon}_0$, the sound velocity v_s, the vertex strength $\gamma_{\mathbf{q}}^{\text{PA}}$ [see Eq. (4.1.5)], the dimensionless coupling strength $\lambda_{\text{e-ph}}$ defined in Eq. (4.2.2), and the ratio k_{TF}/k_F for several materials. Numerical values of the elastic tensors have been taken from Refs. [18, 49, 56] and references therein.

4.2.1 Comparison with optical phonons

For simplicity, let us focus on a single branch of the longitudinal optical (LO) phonons for which a constant frequency ω_0 is assumed. The total Hamiltonian reads as in Eq. (4.1.3) except for the replacements (see Sec. 3.1.1):

$$\omega_{\mathbf{q}} \to \omega_0 \,, \tag{4.2.6}$$

$$v_{\mathbf{q}}^{(0)} \to v_{\mathbf{q}}^{(\infty)} := \frac{e^2}{2\bar{\varepsilon}_\infty \varepsilon_{\text{vac}} q} \,, \tag{4.2.7}$$

$$\bar{\varepsilon}_\infty := \frac{\varepsilon_\infty + 1}{2} \,,$$

$$\gamma_{\mathbf{q}}^{\text{PA}} \to \gamma_{\mathbf{q}}^{\text{OP}} := \left(g \frac{e^2 \hbar \omega_0}{2\varepsilon_{\text{vac}} q} \right)^{\frac{1}{2}} \,, \tag{4.2.8}$$

$$g := \left(\frac{1}{\varepsilon_\infty + 1} - \frac{1}{\varepsilon_0 + 1} \right) > 0 \,,$$

where the previous standard notation for dielectrics is used: ε_∞ is the dielectric constant coming from very-high-frequency interband electronic transitions and ε_0 would be the static dielectric constant in the absence of the

piezoelectric phonons at frequencies much smaller than ω_0.

Again, as shown in the discussion around Eq. (4.1.10), for small frequencies ($\omega \ll \omega_0$), the bare phonon-mediated electron-electron interaction contributes to the long-range part of the total interaction like the Coulomb repulsion:

$$V_{\rm ph}^{\rm OP}(\mathbf{q}, \omega \simeq 0) = |\gamma_{\mathbf{q}}^{\rm OP}|^2 \, G_0^{\rm OP}(\mathbf{q}, \omega \simeq 0) = -g \frac{e^2}{\varepsilon_{\rm vac} q} \ . \tag{4.2.9}$$

However, in contrast to the piezoelectric case, it is here the vertex that introduces the coulombic dependence in q. At small frequencies, $\omega \ll \omega_0$, a single optical phonon is not enough either to provide overscreening, because

$$\frac{-V_{\rm ph}^{\rm OP}(\mathbf{q}, \omega \simeq 0)}{v_{\mathbf{q}}^{(\infty)}} = \frac{\varepsilon_0 - \varepsilon_\infty}{\varepsilon_0 + 1} < 1 \ . \tag{4.2.10}$$

4.3 Effect of piezoelectric phonons on superconducting instabilities

Equipped with the effective electron-electron interaction which results from taking into account the exchange of these acoustic phonons between the electrons in graphene (or other 2D materials), the question can be raised of whether these interactions might be attractive and, depending on some material parameters and the tunable electronic density of graphene, perhaps strong enough to generate electron Cooper pairing and superconductivity [61]. One can further ask whether such a superconductivity could be observed at temperatures attainable in a laboratory without resorting to huge (not achievable through gates) doping levels, as predicted for intrinsic graphene phonons [98] or for Kohn-Luttinger or electronic superconductivity in other graphene heterostructures with repulsive interactions [99].

From Eqs. (4.1.17) and (4.1.9), one sees that in the static limit ($\omega \simeq 0$)

and for $q < 2k_F$, V_{eff} can be written in the form:

$$V_{\text{eff}}(\mathbf{q},0) = \frac{[1-K_R^2(\theta)]v_{\mathbf{q}}^{(0)}}{1+\left[1-K_R^2(\theta)\right]v_{\mathbf{q}}^{(0)}D(E_F)} \ , \tag{4.3.1}$$

where it should be noted that we do not assume $q \ll k_F$, as discussed in the paragraph following Eq. (4.1.2). From the inequality in Eq. (4.1.17), one is thus led to conclude that overscreening of the Coulomb repulsion by the phonon-mediated attraction is not possible. Moreover, and following standard textbook reasoning (see for example Ref. [76]), BCS-type instabilities must also be ruled out. Note however that this conclusion could be substantially changed in case new hard-piezoelectric materials were found. A similar result holds for a single branch of optical phonons, as can be seen from Eq. (4.2.10) (see however Ref. [100] for the effect of multiple optical-phonon branches from the substrate on superconducting instabilities).

Moreover, in case such overscreening occurred, the static dielectric constant from Eq. (4.1.9) would predict unphysical features such as unstable phononic modes with $\tilde{\omega}(q_c) = 0$ for some $q_c \neq 0$ and even imaginary frequencies for $q < q_c$. No matter how small the absolute difference $|1-K_R^2(\theta)|$ happened to be, there would always exist a pole for the static interaction in Eq. (4.1.9) at small enough q (what cannot occur in standard BCS metals [76]), signaling a different type of instability, possibly a charge density wave.

On the other hand, the result in Eq. (4.1.17) for the vertex could still lead to higher-angular-momentum pairing instabilities (as in the Kohn-Luttinger mechanism [101]) provided that $K_R^2(\theta)$ is sufficiently large and anisotropic, a case not considered here.

4.3.1 Eliashberg formalism

The previous reasoning about the absence of superconducting instabilities, is incomplete and somewhat oversimplified. Three reasons support this claim: (i) Long-wave piezoelectric phonon excitations (as considered in the present work) can never be the only source of effective electron-electron in-

teractions; in particular, it has not been taken into account the short-range electric fluctuations of the substrate. (ii) There is definitely some dynamic overscreening at high frequencies [see Eq. (4.1.7)]. And (iii) Coulomb interaction has to be properly renormalized by taking into account collisions with high momentum transfer, which diminishes the Coulomb repulsion and thus comparatively strengthens the other attraction mechanisms.

Leaving aside the first objection momentarily, one can use the Eliashberg formalism, as applied to graphene (in Ref. [98]) to deal with the other two objections. The effective interaction could cause superconducting instabilities if a dimensionless electron-phonon coupling $\lambda^{\rm PA}$ happened to be greater than a (also dimensionless) Coulomb pseudopotential μ^* coming from high-energy renormalizations [102, 98]. The coupling constant $\lambda^{\rm PA}$ in the Eliashberg formalism is the same appearing in (the real part of the) self-energy calculations to renormalize the Fermi velocity (see Subsec. 5.2.2), and is given by:

$$\begin{aligned}
\alpha^2_{\rm PA}F(\omega) &= \frac{|\gamma^{\rm PA}|^2}{2\pi^2\hbar^2 v_s v_F}\frac{\sqrt{1-(\frac{\omega/v_s}{2k_F})^2}}{(1+\frac{k_{\rm TF}}{\omega/v_s})^2}\ , \\
\lambda^{\rm PA} &= 2\int_0^\infty \frac{\alpha^2_{\rm PA}F(\omega)}{\omega}d\omega = \frac{r_s}{\pi}K_R^2\,F(2r_s)\ , \\
F(x) &= \int_0^1 \frac{t\sqrt{1-t^2}\,dt}{(t+x)^2} = -2+x\pi+\frac{(1-2x^2)\,\mathrm{acosh}(x^{-1})}{\sqrt{1-x^2}}\ ,
\end{aligned} \tag{4.3.2}$$

where $r_s(\theta) := \alpha_{\rm fs}/\overline{\varepsilon}(\theta)$, and the symbols $r_s, v_s, \gamma^{\rm PA}, K_R^2$ stand for the Fermi surface angle-averaged quantities of the same name. The constant μ^* equals

$$\mu^* = \frac{\frac{1}{4}D(E_F)V}{1+\frac{1}{4}D(E_F)V\log(\frac{E_F}{\hbar\omega_c})}\ , \tag{4.3.3}$$

where ω_c is some energy cutoff which should satisfy $\omega_{\rm Debye} \ll \omega_c \ll E_F/\hbar$ [98] and V comes from the Fermi-surface average of the Thomas-Fermi

renormalized Coulomb repulsion $v_{\mathbf{q}}^{(0)}/(1+\frac{k_{\rm TF}}{q})$. Then:

$$\frac{1}{4}D(E_F)V = \frac{r_s}{\pi}G(2r_s)\ , \tag{4.3.4}$$
$$G(x) = \int_0^1 \frac{\sqrt{1-t^2}\,dt}{t+x} = -1+\frac{\pi x}{2}+\sqrt{1-x^2}\,\mathrm{acosh}(x^{-1})\ ,$$

and therefore, provided that one takes $\hbar\omega_c \simeq k_B T_{\rm BG}$, it is $\log\left(\frac{E_F}{\hbar\omega_c}\right) \simeq \log(\frac{v_F}{2v_s}) \simeq 5$. Thus, an estimate of the effective pseudo-potential is:

$$\mu^* \simeq \frac{\frac{r_s}{\pi}G(2r_s)}{1+\frac{5r_s}{\pi}G(2r_s)}\ . \tag{4.3.5}$$

There could be intravalley (note that in this analysis, just long-wavelength piezoelectric phonons are taken into account, hence no intervalley pairing instability could occur. This question is addressed in the next paragraph) superconducting instabilities provided that:

$$1 < \frac{\lambda^{\rm PA}}{\mu^*} = K_R^2\,\frac{F(2r_s)}{G(2r_s)}\left[1+\frac{5r_s}{\pi}G(2r_s)\right]\ , \tag{4.3.6}$$

which imposes a constraint on the value of K_R^2 from the piezoelectric substrate with respect to quantities depending on r_s. The coupling K_R should be very large and actually greater than 1 for this choice of ω_c, although there could exist superconductivity in this idealized case of a system consisting just of the graphene electrons and long-wavelength piezoelectric phonons, provided that $E_F/\hbar\omega_c$ is larger and K_R^2 close to 1.

In order to amend the first objection, one has to consider proper phonons of the electronic system (e.g. from graphene), in conjunction with the short range of the piezoelectric ones. Then, pairing instabilities due to intervalley scattering have to be considered as well, because the intravalley-scattering terms contribute also to the intervalley-pairing gap. With the notation in Ref. [98], an estimate of the critical temperature for the intravalley pairing is [98] $T_c^{\rm intra} = 1.13\,\hbar\omega_{\rm Debye}\exp\left(-\frac{1+\lambda}{\lambda_{11}-\mu_{11}^*}\right)$, and a very similar result is obtained for the intervalley transition $T_c^{\rm inter} = 1.13\,\hbar\omega_{\rm Debye}\exp\left(-\frac{1+\lambda}{\lambda-\mu_{12}^*}\right)$,

with $\lambda = \lambda_{11} + \lambda_{12}$ and the previously computed $\lambda^{\rm PA}$ included into the intravalley term λ_{11} (λ_{12} denotes the contribution from all intervalley terms). Here, the pseudo-potential μ^*_{12} is only slightly larger than μ_{11}, and both are given by similar formulas as in Eq. (4.3.3), but with the replacement $\omega_c \to \omega_{\rm Debye}$.

The upshot of this discussion is that the long-wavelength piezoelectric phonons work in favor of pairing instabilities, as shown in Fig. 4.2. It must be emphasized, however, that we are not claiming that a piezoelectric substrate *per se* necessarily increases the critical temperature, since it could be the case that other piezoelectric fluctuations not considered in the present study, for instance, shorter-wavelength modes (whose effect in other scenarios seems in any case to be negligible compared with the long-wavelength modes [103]) may work against pairing instabilities.

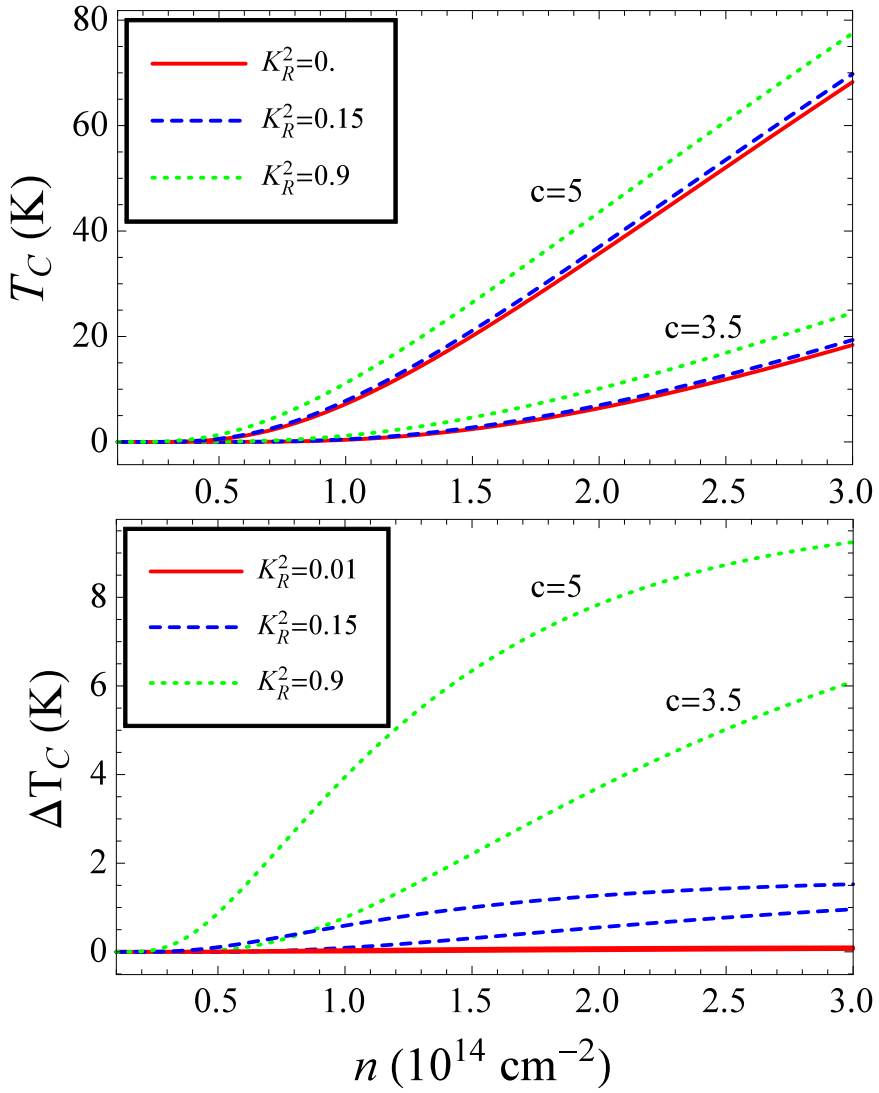

Figure 4.2: Critical temperature and variation from the "bare" one in Ref. [98] for graphene on a piezoelectric substrate, as a function of the conduction-band density. Three pairs of plots are given for three different values of K_R and the two values of the constant $C = 3.5$ and 5 in Eq. (5.1) for λ in the previous Ref. [98].

Chapter 5

Electron self-energy and mobility of doped graphene on a piezoelectric substrate

5.1 Phonon self-energy

After analyzing within a diagrammatic framework the effective carrier interaction due to exchange of surface phonons in the previous chapters, the self-energies acquired by both phonons and charge carriers are studied in the present chapter. Unlike in the previous section, here we focus on the case of graphene, while the piezoelectric material remains arbitrary except in some numerical examples. A generalization to other 2D materials would be straightforward.

Everything will be computed within the parameters and notation of Sec. 4.2, including the approximations there discussed. Specifically, we assume a flat interface and the elastic (long-phonon wavelength) limit for the piezoelectric material. The common assumption that the interface is large enough to permit the neglect of geometrical effects due to finite-size boundaries is made as well. This is expected to be a good approximation for

system sizes much larger than the length scales of the problem (k_F^{-1} and $k_{\rm TF}^{-1}$). The analytical limits and the computation of scattering rates will be often made with angle-averaged substrate parameters.

While the renormalization of the Fermi velocity and the phonon self-energy due to piezoelectric substrate phonons turns out to be small, it will be shown that in some regimes the substrate effects dominate momentum-relaxation mechanism in graphene. For that purpose, we will compare life-times and mobilities with those obtained when only the intrinsic acoustic deformation phonons are considered.

As the piezoelectric coupling of Eq. (4.1.1) enables the transfer of energy between carriers in graphene and the phonon modes of the substrate material, the latter acquire an extra decay rate due to Landau damping. In order to assess the magnitude of this effect, we proceed to estimate the self-energy of the substrate phonons due to their interactions with the graphene carriers. Substituting the bare propagator from Eq. (4.1.8):

$$\tilde{G}^{\rm PA}(\mathbf{q},\omega) = \frac{2\omega_{\mathbf{q}}/\hbar}{\omega^2 - \omega_{\mathbf{q}}^2 - 2\hbar^{-1}\omega_{\mathbf{q}}|\gamma_{\mathbf{q}}^{\rm PA}|^2 \frac{\Pi_0(q,\omega)}{\varepsilon_{\rm RPA}(\mathbf{q},\omega)}} \ . \tag{5.1.1}$$

In the phonon-frequency range $\omega \sim v_s q \ll v_F q$ which is the most interesting, the polarization function can be approximated by (see e.g. Ref. [104]):

$$\Pi_0(q,\omega) \simeq -D(E_F)\left(1 + i\frac{\omega}{v_F q}\right) \ , \tag{5.1.2}$$

in the RPA electron-electron dielectric function of Eq. (4.1.11), so that in terms of the parameter $\lambda_{\rm e-ph}(\theta)$, the poles of $\tilde{G}^{\rm PA}$ are shifted to:

$$\tilde{\omega}_{\mathbf{q}} = \pm v_s q \left(1 - \lambda_{\rm e-ph}\frac{k_F}{q + k_{\rm TF}}\right)^{\frac{1}{2}} \mp i\ \lambda_{\rm e-ph}\frac{v_s}{v_F}\frac{v_s k_F}{2}\left(\frac{q}{q + k_{\rm TF}}\right)^2 \ . \tag{5.1.3}$$

In the long-wavelength limit ($q \ll k_F$), the leading order of the ratio of the

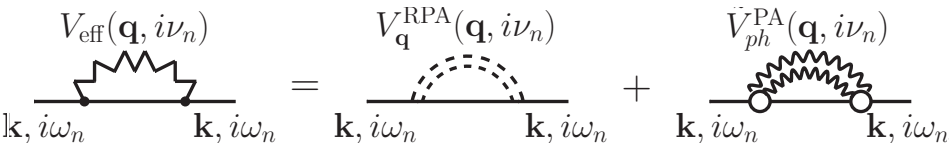

Figure 5.1: Electron self-energy in the G_0W approximation, see Eq. (5.2.1).

imaginary and real parts of the dressed-phonon energy goes like:

$$\left|\frac{\mathrm{Im}(\tilde{\omega}_{\mathbf{q}})}{\mathrm{Re}(\tilde{\omega}_{\mathbf{q}})}\right| \simeq \frac{1}{2} K_R^2 \, \frac{v_s}{v_F} \left(\frac{q}{k_{\rm TF}}\right)^{\pm 1} , \tag{5.1.4}$$

where $(q/k_{\rm TF})^{\pm 1} \ll 1$, the case $k_{\rm TF} \ll q \ll k_F$ being meaningful only in those materials where $k_{\rm TF}$ is substantially smaller that k_F. Due to the fact that $v_F/v_s \sim 300$ and to the $K_R^2(\theta)$ values shown in Table 4.1 for typical materials, the lifetime of the phonons can be neglected in all analyzed regimes. It can also be shown that, near the quasiparticle poles, the residue $Z_{\mathbf{q}}$ is close to unity (i.e., the wave-function renormalization is weak):

$$\tilde{G}^{\rm PA}(\mathbf{q}, \omega) \simeq Z_{\mathbf{q}} \frac{2\tilde{\omega}_{\mathbf{q}}/\hbar}{\omega^2 - \tilde{\omega}_{\mathbf{q}}^2} \tag{5.1.5}$$

$$Z_{\mathbf{q}} \simeq 1 + \lambda_{\rm e-ph} \frac{k_F}{q + k_{\rm TF}} \, . \tag{5.1.6}$$

Thus in the following, the fact that substrate phonons are well-defined, stable quasiparticles can be assumed, and the renormalized phonon propagator of Eq. (5.1.5) will be approximated by the bare one, Eq. (4.1.8).

5.2 Electron self-energy

This section focuses on the case of n-doped graphene ($E_F > 0$), so that the electron self-energies shall be calculated at energies $\hbar\omega$ in the upper Dirac cone. With an effective electron-electron interaction $V_{\rm eff}$ given in Eq. (4.1.16) and Fig. 4.1, the self-energy acquired by the charge carriers in graphene (within the G_0W approximation [61], as indicated in Fig. 5.1) has

the general form:

$$\Sigma_+(\mathbf{k}, i\omega_n) = -k_B T \sum_{s=\pm} \sum_{\mathbf{q}} \sum_{i\nu_n} F_{+s}(\mathbf{k}, \mathbf{k}+\mathbf{q}) \times G^{\mathrm{el}}_{0,s}(\mathbf{k}+\mathbf{q}, i\omega_n + i\nu_n) V_{\mathrm{eff}}(\mathbf{q}, i\nu_n) \ , \tag{5.2.1}$$

where the subscript + refers to the conduction band (the calculation for Σ_- being analogous), the index $s = \pm$ is summed over both bands,

$$G^{\mathrm{el}}_{0,s}(\mathbf{k}, \omega) = (\omega - E_{\mathbf{k}s} - \mu)^{-1} \tag{5.2.2}$$

denotes the (bare) electron propagator, $i\nu_n$ and $i\omega_n$ are, respectively, the bosonic and fermionic Matsubara frequencies, and the spinor-overlap factor

$$F_{+s}(\mathbf{k}, \mathbf{k}+\mathbf{q}) = \frac{1}{2}(1 + s\cos\alpha) \tag{5.2.3}$$

arises due to the sublattice structure of graphene [5], α being the angle formed by $\mathbf{k}$ and $\mathbf{k}+\mathbf{q}$.

Equation (4.1.16) for V_{eff} allows one to separate the self-energy Σ_+ into contributions due to electron-electron and electron-phonon interactions. While the former has been considered in Refs. [104, 105], the contributions of graphene intrinsic optical or acoustic phonons, as well as optical substrate phonons, to the electron self-energy have been studied in Refs. [84, 104]. Thus the present work shall focus entirely on the effect of piezoelectric acoustic substrate phonons, as expressed in the self-energy term:

$$\Sigma^{\mathrm{PA}}_+(\mathbf{k}, i\omega_n) = - k_B T \sum_{s=\pm} \sum_{\mathbf{q}} \sum_{i\nu_n} F_{+s}(\mathbf{k}, \mathbf{k}+\mathbf{q}) \times G^{\mathrm{el}}_{0,+}(\mathbf{k}+\mathbf{q}, i\omega_n + i\nu_n) \tilde{V}^{\mathrm{PA}}_{\mathrm{ph}}(\mathbf{q}, i\nu_n) \ , \tag{5.2.4}$$

where

$$\tilde{V}^{\mathrm{PA}}_{\mathrm{ph}}(\mathbf{q}, \omega) \equiv \left| \frac{\gamma^{\mathrm{PA}}_{\mathbf{q}}}{\varepsilon_{\mathrm{RPA}}(\mathbf{q}, \omega)} \right|^2 \tilde{G}^{\mathrm{PA}}(\mathbf{q}, \omega). \tag{5.2.5}$$

In order to sum over Matsubara frequencies, one must follow Ref. [61] and

approximate the vertex renormalization by its static limit [see Eq. (4.1.13)] while neglecting the phonon self-energy, i.e., the factor $\tilde{V}_{\rm ph}^{\rm PA}(\mathbf{q},\omega)$ is replaced in Eq. (5.2.4) by:

$$\bar{V}_{\rm ph}^{\rm PA}(\mathbf{q},\omega) \equiv \left|\frac{\gamma_{\mathbf{q}}^{\rm PA}}{\varepsilon_{\rm RPA}(\mathbf{q},0)}\right|^2 G_0^{\rm PA}(\mathbf{q},\omega)\,. \tag{5.2.6}$$

The result is the following retarded self-energy:

$$\Sigma_+^{\rm PA}(\mathbf{k},\omega) = \sum_{s=\pm}\int \frac{d\mathbf{q}}{(2\pi)^2}\left|\frac{\gamma_{\mathbf{q}}^{\rm PA}}{\varepsilon_{\rm RPA}(\mathbf{q},0)}\right|^2 F_{+s}(\mathbf{k},\mathbf{k}') \times\left[\frac{n_B(\hbar\omega_{\mathbf{q}})+n_F(\epsilon_{k's})}{\hbar\omega+\hbar\omega_{\mathbf{q}}-\epsilon_{k's}+i0^+}+\frac{n_B(\hbar\omega_{\mathbf{q}})+1-n_F(\epsilon_{k's})}{\hbar\omega-\hbar\omega_{\mathbf{q}}-\epsilon_{k's}+i0^+}\right], \tag{5.2.7}$$

where $\mathbf{k}'$ stands for $\mathbf{k}'\equiv\mathbf{k}+\mathbf{q}$,

$$n_B(\hbar\omega_{\mathbf{q}}) = \left[\exp\left(\frac{\hbar\omega_{\mathbf{q}}}{k_BT}\right)-1\right]^{-1}, \tag{5.2.8}$$

$$n_F(\epsilon_{k's}) = \left[\exp\left(\frac{\epsilon_{k's}}{k_BT}\right)+1\right]^{-1}, \tag{5.2.9}$$

denote the Bose and Fermi distributions, respectively, and the energies $\epsilon_{ks}=E_{ks}-\mu$ are taken relative to the chemical potential. The real and imaginary parts of Eq. (5.2.7) are being evaluated separately. Hereafter, the assumption $T\ll T_F\equiv k_B^{-1}E_F$ is understood, so that the zero-temperature RPA dielectric function can be used [77]. Since $\mu\simeq E_F$, one can write:

$$\epsilon_{ks} = \hbar v_F(ks-k_F)\ . \tag{5.2.10}$$

One must be aware too that very low doping leads to a low Fermi temperature T_F, so that the zero-temperature $\varepsilon_{\rm RPA}$ may become inaccurate and should be replaced by the Debye-Hückel approximation. Then, the screening would increase in this scenario of graphene with bigger temperatures. This behavior contrasts sharply with that found in conventional (nonzero mass) 2D electron systems [106].

5.2.1 Imaginary part

The imaginary part of Eq. (5.2.7) acquires the form:

$$\mathrm{Im}\,\Sigma_{+}^{\mathrm{PA}}(\mathbf{k},\omega) = -\pi \sum_{s=\pm}\sum_{t=\pm}\int \frac{d\mathbf{q}}{(2\pi)^2}\left|\frac{\gamma_{\mathbf{q}}^{\mathrm{PA}}}{\varepsilon_{\mathrm{RPA}}(\mathbf{q},0)}\right|^2 \frac{1+s\cos\alpha}{2} \times \left[n_F(\hbar\omega_{\mathbf{q}}+t\hbar\omega)+n_B(\hbar\omega_{\mathbf{q}})\right]\delta(\hbar\omega+t\hbar\omega_{\mathbf{q}}-\epsilon_{k's}), \tag{5.2.11}$$

where $t{=}\pm1$ corresponds to the absorption or emission of a phonon, respectively.

Setting $\omega = \epsilon_{k+}$ in Eq. (5.2.11), that is, considering the on-shell self-energy, yields the value $\hbar/(2\tau_{\mathbf{q}})$ for the decay width of charge carriers with wave vector $\mathbf{k}$. Here, it is assumed that the renormalization of the Fermi energy $\Delta E_F = \mathrm{Re}\,\Sigma^{\mathrm{PA}}(k_F,0)$, as given by the pole of the dressed electron propagator, is tiny enough, as can be checked in the next section [see Eq. (5.2.32) and related ones]. To obtain analytical expressions for the asymptotic behaviors of the on-shell self-energy, it is convenient to introduce the quasi-elastic approximation:

$$\delta(\epsilon_{k+}+t\hbar\omega_{\mathbf{q}}-\epsilon_{k's}) \simeq \delta(\epsilon_{k+}-\epsilon_{k's}) \tag{5.2.12}$$

in Eq. (5.2.11), which is well justified since $v_F/v_s \sim 300$. Since we work with $k_F > 0$, the $s = -$ term is null. Hereafter, ϵ_k will be equivalent to ϵ_{k+}, so that:

$$\epsilon_k = \hbar v_F(k-k_F)\,. \tag{5.2.13}$$

For magnitude estimates, $\epsilon_k > 0$ will be assumed.

The relevant scale for finite-temperature effects in graphene, like in any other system whose carrier densities are much smaller than in conventional metals, is the Bloch-Grüneisen temperature T_{BG}, defined as the temperature scale of the acoustic phonons in the Fermi sea.

$$k_B T_{\mathrm{BG}} \equiv 2\hbar v_s k_F\,. \tag{5.2.14}$$

Note that $T_{\rm BG}$ is different from the Debye temperature in the usual case of an integer number of carriers per atom.

Zero temperature, small k

At zero temperature (here it means $T \ll \epsilon_k/k_B, T_{\rm BG}$), n_F in (5.2.11) becomes a step function which cuts off the momentum integration, while n_B vanishes. Then, in the limit $\epsilon_k \ll \hbar v_s k_{\rm TF}$ [for which the largest contributing q in Eq. (5.2.11) is $q \sim \epsilon_k/\hbar v_s$, so that one can assert $q \ll k_{\rm TF}$] the quasiparticle lifetime decays as a ϵ_k^3 near the Fermi surface while depending on the direction of the $\mathbf{k}$ vector:

$$-\mathrm{Im}\,\Sigma_+^{\rm PA}(\mathbf{k},\epsilon_k) \simeq \frac{1}{6\pi}\frac{|\gamma_\perp^{\rm PA}|^2}{\hbar v_F k_{{\rm TF}\perp}^2}\frac{\epsilon_k^3}{(\hbar v_{s\perp})^3} = \frac{\lambda_\perp}{24}\left(\frac{k_F}{k_{{\rm TF}\perp}}\right)^2\left(\frac{v_F}{v_{s\perp}}\right)^2\left(\frac{\epsilon_k}{E_F}\right)^3 \hbar v_F k_F\ , \qquad (5.2.15)$$

where all the substrate-related constants, like $\lambda_\perp \equiv \lambda_{\text{e-ph}}(\theta_{\perp\mathbf{k}})$ of Eq. (4.2.2), have to be taken in the direction $\theta_{\perp\mathbf{k}}$ perpendicular to $\mathbf{k}$. The fast ϵ_k^3 decrease (as $\epsilon_k \to 0$) is due to the vertex renormalization, since $\varepsilon_{\rm RPA}$ in Eq. (5.2.11) diverges for $q \ll k_{\rm TF}$ [see Eq. (4.1.13)].

Hereafter, the subindex $\perp$ is removed from the anisotropic parameters in those expressions where they are assumed to be direction-independent or only their order of magnitude matters.

Zero temperature, larger k

For $\epsilon_k \gg \hbar v_s k_{\rm TF}$, one obtains the result:

$$-\mathrm{Im}\,\Sigma_+^{\rm PA}(k,\epsilon_k) \simeq \frac{\lambda}{4}\hbar v_s k\int_0^1 \frac{y^2\sqrt{1-y^2}}{\left(y+\frac{k_{\rm TF}}{2k}\right)^2}\,dy = \frac{\lambda\hbar v_s k}{4} f\left(\frac{k_{\rm TF}}{2k}\right)\ , \qquad (5.2.16)$$

$$f(x) = 3x + \frac{\pi}{4}(1-6x^2) + \frac{(3x^3-2x)\,\mathrm{acosh}(x^{-1})}{\sqrt{1-x^2}}\,. \qquad (5.2.17)$$

This admits two regimes, one for $\hbar v_s k_{\rm TF} \ll \epsilon_k \ll E_F$,

$$-\operatorname{Im}\Sigma_+^{\rm PA}(k,\epsilon_k) \simeq \frac{\lambda k_B T_{\rm BG}}{8} f\left(\frac{2\alpha_{\rm fs}}{\bar{\varepsilon}_0}\right) , \tag{5.2.18}$$

while for $\epsilon_k \gg E_F$:

$$-\operatorname{Im}\Sigma_+^{\rm PA}(k,\epsilon_k) \simeq \frac{\lambda\pi v_s}{16 v_F}\epsilon_k \, . \tag{5.2.19}$$

Returning to the low-energy ($\epsilon_k \ll \hbar v_s k_{\rm TF}$) regime [see Eq. (5.2.15)], it should be noted that, without the vertex-screening effect [that is, setting $\varepsilon_{\rm RPA} \to 1$ in Eq. (5.2.11)], instead of the ϵ_k^3 behavior one would find the linear-ϵ_k dependence characteristic of a marginal Fermi liquid:

$$-\operatorname{Im}\Sigma_{+(\text{no scr})}^{\rm PA}(\mathbf{k},\epsilon_k) \simeq \frac{\lambda_\perp}{8}\epsilon_k \ , \tag{5.2.20}$$

which (for materials such that $k_{\rm TF} \ll k_F$) behaves similarly to the true self-energy in the range $\hbar v_s k_{\rm TF} \ll \epsilon_k \ll \hbar v_s k_F$, since $\varepsilon_{\rm RPA}$ tends to unity for the momenta $q \gg k_{\rm TF}$ dominating the integral in Eq. (5.2.11). We will see however that a small offset remains due to the contribution of the screened low-q values ($q \ll k_{\rm TF}$).

Table 4.1 shows representative angle-independent material parameters, including those that will be used for the numerical calculations discussed in Sec. 5.3. From Eqs. (5.2.15),(5.2.20) and the parameter values shown in Table 4.1, it is safe to conclude that, at zero temperature, the damping rate due to the electron-phonon coupling is always much smaller than ϵ_k. Thus the single-electron quasiparticles near the Fermi surface are well defined.

Small k, low nonzero temperature

So far we have assumed zero temperature, i.e., $k_B T \ll \epsilon_k$. At nonzero temperatures, the vertex renormalization is fundamental to avoid logarithmic divergences. These occur for the unscreened self-energy at any nonzero temperature due to the divergent contribution of small-q values. Focusing on the correctly screened self-energy, it is considered first the nonzero, low-temperature limit $\epsilon_k \ll k_B T \ll 2\hbar v_s k_{\rm TF}, k_B T_{\rm BG}$. Again, only the

perpendicular-to-**k** substrate-related constants appear. One obtains:

$$-\mathrm{Im}\,\Sigma_+^{\mathrm{PA}}(k,\epsilon_k) \simeq \lambda_\perp k_B T \left(\frac{k_F}{k_{\mathrm{TF}\perp}}\right)^2 \left(\frac{T}{T_{\mathrm{BG}\perp}}\right)^2 \frac{7\zeta(3)}{2} \ , \tag{5.2.21}$$

with $7\zeta(3)/2 \simeq 4.21$. The essential independence from k of the lifetime (which allows for the replacement $k \simeq k_F$) is a general property of the case $\epsilon_k \ll T$. In those materials where ε_0 is so high that $k_{\mathrm{TF}} \ll k_F$, and therefore a temperature regime exists such that $\epsilon_k \ll \hbar v_s k_{\mathrm{TF}} \ll k_B T \ll k_B T_{\mathrm{BG}}$, the T^3 law is replaced by a $\sim T \log T$ behavior. Specifically, the asymptotic expression reads:

$$-\mathrm{Im}\,\Sigma_+^{\mathrm{PA}}(k,\epsilon_k) \simeq \lambda_\perp k_B T \left(\frac{k_F}{k_{\mathrm{TF}\perp}}\right)^2 \log\left(\frac{\hbar v_s k_{\mathrm{TF}}}{k_B T}\right) \ . \tag{5.2.22}$$

Extra crossing terms appear when both $k_B T$ and ϵ_k are of comparable magnitude, but both smaller than $\hbar v_s k_{\mathrm{TF}}$:

$$\begin{aligned} -\mathrm{Im}\,\Sigma_+^{\mathrm{PA}}(k,\epsilon_k) \simeq{}& \frac{\lambda}{32}\left(\frac{\bar{\varepsilon}_0}{\alpha_{\mathrm{fs}}}\right)^2 \left(\frac{T}{T_{\mathrm{BG}}}\right)^2 \left[4\zeta(3) - 4\mathrm{Li}_3\left(-e^{-\epsilon_k/k_B T}\right)\right] k_B T \\ &+ \frac{\lambda}{96}\left(\frac{\bar{\varepsilon}_0}{\alpha_{\mathrm{fs}}}\right)^2 \left(\frac{\epsilon_k}{k_B T_{\mathrm{BG}}}\right)^2 \epsilon_k + \frac{\lambda\pi^2}{96}\left(\frac{\bar{\varepsilon}_0}{\alpha_{\mathrm{fs}}}\right)^2 \left(\frac{T}{T_{\mathrm{BG}}}\right)^2 \epsilon_k \ , \end{aligned}$$

with $\mathrm{Li}_3(x)$ denoting the trilogarithm function. This is equivalent to the typical expression for 3D metals $\tau^{-1} \propto [\epsilon_k^2 + (\pi k_B T)^2]\,[1+\exp(\epsilon_k/k_B T)]^{-1}$ [97], but in our case with some extra crossing terms. Of course, one must add the electron-electron contribution with the known laws $\tau^{-1} \propto \epsilon_k^2 \log(\epsilon_k/E_F)$ for $T \ll \epsilon_k$ and $\tau^{-1} \propto T^2 \log(T/T_F)$ for $\epsilon_k \ll T$ in the 2DEG, whether parabolic or (chiral) linear [97, 104].

Small k, high temperature

The high-temperature limit ($T_{\mathrm{BG}} \ll T$, while only $\epsilon_k \ll E_F$ is required),

where phonons are nondegenerate, yields:

$$-\mathrm{Im}\,\Sigma_+^{\mathrm{PA}}(k,\epsilon_k) \simeq \frac{\lambda}{4} k_B T \int_0^1 \frac{y\sqrt{1-y^2}}{\left(y+\frac{k_{\mathrm{TF}}}{2k}\right)^2}\, dy = \frac{\lambda k_B T}{4} g\left(\frac{k_{\mathrm{TF}}}{2k}\right) , \quad (5.2.23)$$

$$g(x) = -2 + \pi x + \frac{(1-2x^2)\,\mathrm{acosh}(x^{-1})}{\sqrt{1-x^2}} . \quad (5.2.24)$$

The logarithmic divergence of the function g at $x \to 0$ becomes relevant in the limit $k \gg k_{\mathrm{TF}}$, where:

$$-\,\mathrm{Im}\,\Sigma_+^{\mathrm{PA}}(k,\epsilon_k) \simeq \frac{\lambda k_B T}{4}\left[\log\left(\frac{4k}{k_{\mathrm{TF}}}\right) - 2\right] . \quad (5.2.25)$$

Comparison with graphene intrinsic phonons

Comparing Eqs. (5.2.15), (5.2.21), and (5.2.23) with the corresponding limiting expressions for the electron self-energy induced by the graphene intrinsic deformation-potential acoustic (DA) phonons (see Sec. 3.1.3), we see below that, for an important range of parameter values, the inverse lifetime is dominated by the piezoelectric substrate phonons.

For estimates, we borrow the values of $\Sigma_+^{\mathrm{DA}}(k,\epsilon_k)$ from Ref. [104]. Specifically, with a deformation constant $D \simeq 25$ eV, and taking $k_F = [k_F]\,10^6\ \mathrm{cm}^{-1}$ (this momentum unit corresponds to a density of $k_F^2/\pi \simeq 3.2 \times 10^{11}\ \mathrm{cm}^{-2}$, see Sec. A.3), one obtains from Eq. (5.2.15):

$$\frac{\mathrm{Im}\,\Sigma_+^{\mathrm{PA}}(k,\epsilon_k)}{\mathrm{Im}\,\Sigma_+^{\mathrm{DA}}(k,\epsilon_k)} \simeq \frac{20}{[k_F]^2}\lambda\,\overline{\varepsilon}_0^2 \frac{\epsilon_k}{1\ \mathrm{meV}} , \quad (5.2.26)$$

for $k_B T \ll \epsilon_k \ll \hbar v_s k_{\mathrm{TF}}$.

Likewise, at nonzero temperatures ($\epsilon_k/k_B \ll T \ll T_{\mathrm{BG}}$), one gets from Eq. (5.2.21):

$$\frac{\mathrm{Im}\,\Sigma_+^{\mathrm{PA}}(k,\epsilon_k)}{\mathrm{Im}\,\Sigma_+^{\mathrm{DA}}(k,\epsilon_k)} \simeq \frac{100}{[k_F]^2}\lambda\,\overline{\varepsilon}_0^2 \frac{k_B T}{1\ \mathrm{meV}} . \quad (5.2.27)$$

Finally, at high temperatures ($\epsilon_k/k_B \ll T_{\mathrm{BG}} \ll T$), one obtains from

Eq. (5.2.23) the k-independent ratio:

$$\frac{\mathrm{Im}\,\Sigma_+^{\mathrm{PA}}(k,\epsilon_k)}{\mathrm{Im}\,\Sigma_+^{\mathrm{DA}}(k,\epsilon_k)} \simeq \frac{35\,g\left(\frac{2\alpha_{\mathrm{fs}}}{\bar{\varepsilon}_0}\right)}{[k_F]}\lambda\ . \tag{5.2.28}$$

From these ratios, one concludes that piezoelectric acoustic phonons can dominate over deformation acoustic phonons in an appreciable range of realistic material parameters, especially for small carrier concentrations. The smaller value of $D \simeq 6.8$ eV also found in the literature [50, 88] would increase further the relative importance of piezoelectric phonons against intrinsic ones. The values of $D \simeq 7.8$ eV and 12 eV used in Refs. [107, 108], respectively, are closer to the value of 6.8 eV considered in the Refs. [50, 88]. This seems to suggest that the value of 25 eV from Ref. [104], which we have used, might be too large.

5.2.2 Real part

For the real part of the self-energy, one obtains from Eq. (5.2.7):

$$\begin{aligned}\mathrm{Re}\,\Sigma_+^{\mathrm{PA}}(\mathbf{k},\omega) = \sum_{s=\pm}\int \frac{d\mathbf{q}}{(2\pi)^2}\left|\frac{\gamma_{\mathbf{q}}^{\mathrm{PA}}}{\varepsilon_{\mathrm{RPA}}(\mathbf{q},0)}\right|^2 F_{+s}(\mathbf{k},\mathbf{k}') \\ \times\left[\frac{n_B(\hbar\omega_{\mathbf{q}})+n_F(\epsilon_{k's})}{\hbar\omega+\hbar\omega_{\mathbf{q}}-\epsilon_{k's}}+\frac{n_B(\hbar\omega_{\mathbf{q}})+1-n_F(\epsilon_{k's})}{\hbar\omega-\hbar\omega_{\mathbf{q}}-\epsilon_{k's}}\right]\ ,\end{aligned} \tag{5.2.29}$$

where the denominators are to be understood as principal values. Unlike for many-body effects directly caused by the electron-electron interaction, this phonon contribution to the electron self-energy tends to be negligibly small compared to the Fermi energy. However, its derivatives are larger. As a result, the phonon-induced contributions to the Fermi-velocity renormalization are larger than those stemming from the direct electron-electron interactions.

Since the partial derivative $\partial\mathrm{Re}\,\Sigma_+^{\mathrm{PA}}(\mathbf{k},\omega)/\partial(v_F\mathbf{k})$ is, by a factor of v_s/v_F, smaller than $\partial\mathrm{Re}\,\Sigma_+^{\mathrm{PA}}(\mathbf{k},\omega)/\partial\omega$ (see Ref. [109]), it suffices to focus on the

frequency derivative, in contrast to the case of electron-electron interactions, where both derivatives matter [61, 110]. We thus approximate:

$$\tilde{v}_F(\hat{\mathbf{k}}) = v_F \left[1 - \frac{\partial \mathrm{Re}\, \Sigma_+^{\mathrm{PA}}(\hat{\mathbf{k}} k_F, \omega)}{\partial \omega} \bigg|_{\omega=0} \right]^{-1} , \tag{5.2.30}$$

for the (direction-dependent) renormalization of the Fermi velocity in graphene induced by piezoelectric acoustic substrate phonons.

For further analysis, it us useful to separate Eq. (5.2.7) into three terms [61]:

$$\Sigma_+^{\mathrm{PA}} = \Sigma_+^{(\mathrm{ph})} + \Sigma_+^{(\mathrm{el})} + \Sigma_+^{(\mathrm{vac})} , \tag{5.2.31}$$

where $\Sigma_+^{(\mathrm{ph})}$ contains just the Bose factor $n_B(\hbar\omega_{\mathbf{q}})$, $\Sigma_+^{(\mathrm{el})}$ the Fermi factor $n_F(\epsilon_{k's})$, and $\Sigma_+^{(\mathrm{vac})}$ the remaining vacuum term. In the following, as in the previous subsection, angle-independent material parameters are assumed.

The real part of $\Sigma_+^{(\mathrm{vac})}$ at $\omega = 0$ is independent of the Fermi energy:

$$\mathrm{Re}\, \Sigma_+^{(\mathrm{vac})}(k, 0) \simeq -\frac{\lambda}{16} \frac{v_s}{v_F} \left[\hbar v_F k_c + \hbar v_F k \log \left(\frac{k_c - k}{k} \right) \right] , \tag{5.2.32}$$

where k_c is a cutoff momentum of the order of the inverse lattice spacing. Because of the small prefactor, $\mathrm{Re}\, \Sigma_+^{(\mathrm{vac})}(k_F, 0)$ represents a weak correction to the chemical potential for all relevant carrier densities, even for $k_c \gg k_F$. We will see that its derivative can also be neglected because $\partial_\omega \mathrm{Re}\, \Sigma_+^{(\mathrm{vac})}(k_F, 0) \simeq (\lambda/4)(v_s/v_F)(1 + \log k_F/k_c) \ll \partial_\omega \mathrm{Re}\, \Sigma_+^{(\mathrm{el})}(k_F, 0)$.

At temperatures $T \ll T_{\mathrm{BG}}$, the term containing the Bose factors $\mathrm{Re}\, \Sigma_+^{(\mathrm{ph})}$ is exponentially small, while at temperatures $T \gg T_{\mathrm{BG}}$ it does not grow larger than a factor T/T_{BG} times the expression in Eq. (5.2.32). Hence one can also neglect $\partial_\omega \mathrm{Re}\, \Sigma_+^{(\mathrm{ph})}$.

Thus the only term that can affect the electronic properties is $\mathrm{Re}\, \Sigma_+^{(\mathrm{el})}(\mathbf{k}, \omega)$, which is likewise small in magnitude, at most twice the term shown in Eq. (5.2.32), but has a larger derivative. Note that here the quasi-elastic approximation ($\hbar\omega_{\mathbf{q}} \ll \epsilon_{k'}$) is not informative, since $\mathrm{Re}\, \Sigma_+^{(\mathrm{el})}(\mathbf{k}, \omega)$ vanishes

when $\hbar\omega_{\mathbf{q}}$ is set to zero.

The integral:

$$\left.\frac{\partial \mathrm{Re}\,\Sigma_+^{(\mathrm{el})}(\hat{\mathbf{k}}k_F,\omega)}{\partial\omega}\right|_{\omega=0} = -\sum_{s=\pm}\int\frac{d\mathbf{q}}{(2\pi)^2}\left|\frac{\gamma_{\mathbf{q}}^{\mathrm{PA}}}{\varepsilon_{\mathrm{RPA}}}\right|^2 F_{+s}(\mathbf{k},\mathbf{k}')\; n_F(\epsilon_{k's}) \times\left[\frac{1}{(\epsilon_{k's}-\hbar\omega_{\mathbf{q}})^2}-\frac{1}{(\epsilon_{k's}+\hbar\omega_{\mathbf{q}})^2}\right] \tag{5.2.33}$$

can be computed by changing variables ($d\mathbf{q}\to d\mathbf{k}'$, with $\mathbf{k}'=\mathbf{k}+\mathbf{q}$) and performing the radial integral first by parts, with:

$$u = k' n_F(\epsilon_{k's})\,,\;\; dv = \frac{dk'}{(\epsilon_{k's}\pm\hbar v_s q)^2}\,.$$

One arrives at a direction-dependent expression which integrates over the Fermi surface:

$$\left.\frac{\partial \mathrm{Re}\,\Sigma_+^{(\mathrm{el})}(\hat{\mathbf{k}}k_F,\omega)}{\partial\omega}\right|_{\omega=0} = -\int_0^{2\pi}\frac{d\alpha}{\hbar v_F(2\pi)^2}\left|\frac{\gamma_{\mathbf{k}+\mathbf{q}}^{\mathrm{PA}}}{\varepsilon_{\mathrm{RPA}}}\right|^2 F_{+s}(\mathbf{k},\mathbf{k}+\mathbf{q})\frac{2}{\hbar\omega_{\mathbf{q}}}\,, \tag{5.2.34}$$

where, as in Eq. (5.2.3), α is the angle between $\mathbf{k}$ and $\mathbf{k}+\mathbf{q}$.

After further averaging over the Fermi surface (i.e., over $\hat{\mathbf{k}}$ directions), the ratio in Eq. (5.2.30) becomes similar to the temperature prefactor of the high-temperature damping in Eq. (5.2.23):

$$\tilde{v}_F = \frac{v_F}{1+\frac{\lambda}{4\pi}f\left(\frac{k_{\mathrm{TF}}}{2k_F}\right)} = \frac{v_F}{1+\frac{K_R^2 r_s}{\pi}f\left(2r_s\right)}\;, \tag{5.2.35}$$

where, we recall, all variables are angle-averaged. Inspection of Eq. (5.2.35) shows that the renormalization of the Fermi velocity cannot exceed 3% even for $K_R^2\sim 1$, and K_R is usually much smaller. The result shown in Eq. (5.2.35) permits us to confirm the validity of neglecting the vacuum and phonon self-energy parts. A more accurate estimate of the ra-

tios between derivatives yields $\partial_\omega \mathrm{Re}\,\Sigma_+^{(\mathrm{vac})}/\partial_\omega \mathrm{Re}\,\Sigma_+^{(\mathrm{el})} = \mathcal{O}(v_s/v_F) \ll 1$, while $\partial_\omega \mathrm{Re}\,\Sigma_+^{(\mathrm{ph})}/\partial_\omega \mathrm{Re}\,\Sigma_+^{(\mathrm{el})}$ is $\mathcal{O}(v_s/v_F)$ for $T \ll T_{\mathrm{BG}}$ and $\mathcal{O}(T/T_F)$ for $T_{\mathrm{BG}} \ll T \ll T_F$.

5.2.3 Electron mobility

Within Boltzmann transport theory, the momentum (or transport) relaxation time $\tau_{+\mathrm{tr}}(\mathbf{k})$ (where the subscript denotes "transport" and + denotes the band) is calculated analogously to the inverse lifetime in Sec. 5.2.1, but with an extra angular factor $(1-\cos\alpha) = 2\sin^2(\alpha/2) = q^2/2k^2$ in the integrand, which increases the weight of large-angle scattering processes. Specifically, Eq. (5.2.11) is replaced by:

$$\frac{\hbar}{2\,\tau_{+\mathrm{tr}}^{\mathrm{PA}}(\mathbf{k})} = \pi \sum_{s=\pm}\sum_{t=\pm}\int \frac{d\mathbf{q}}{(2\pi)^2}\frac{q^2}{2k^2}\left|\frac{\gamma_{\mathbf{q}}^{\mathrm{PA}}}{\varepsilon_{\mathrm{RPA}}(\mathbf{q},0)}\right|^2 \frac{1+s\cos\alpha}{2} \times \left[n_F(\hbar\omega_{\mathbf{q}}+t\epsilon_k)+n_B(\hbar\omega_{\mathbf{q}})\right]\delta(\epsilon_{k+}-\epsilon_{k's}) \;, \tag{5.2.36}$$

where the quasielastic approximation has been made. The inclusion of this additional q^2 factor in the integrand improves the quasielastic approximation, changes the power-law scaling at low temperatures (by generating an extra factor T^2), and corrects the lifetime with a constant factor at temperatures greater than T_{BG}.

Low temperature

For quasiparticle energies such that $\epsilon_k/k_B \ll T$, one finds (after angle averaging) results that are essentially independent of ϵ_k, i.e., $\tau_{+\mathrm{tr}}^{\mathrm{PA}}(k) \simeq \tau_{+\mathrm{tr}}^{\mathrm{PA}}(k_F)$. In the low, yet nonzero temperature regime $\epsilon_k/k_B \ll T \ll 2r_s T_{\mathrm{BG}}$, one ob-

tains:

$$\frac{\hbar}{2\,\tau^{\rm PA}_{+\rm tr}(k_F)} \simeq \frac{\lambda k_B T}{8}\left(\frac{k_B T}{\hbar v_s k_{\rm TF}}\right)^4 \frac{k_{\rm TF}^2}{k_F^2}\int_0^\infty dx\; x^4 {\rm csch}(x)$$
$$= \frac{\lambda k_B T}{8}\left(\frac{\bar{\varepsilon}_0}{\alpha_{\rm fs}}\right)^2\left(\frac{T}{T_{\rm BG}}\right)^4 \frac{93\,\zeta(5)}{2}\;, \qquad (5.2.37)$$

$(93\,\zeta(5)/2 \simeq 48.2)$ which should be compared to Eq. (5.2.21). The shift from a T^3 to a T^5 behavior is due to the transport-induced reduced weight (by a factor $q^2/2k_F^2$) of the low-q values dominating the inverse transport lifetime at low temperatures.

If the vertex screening is neglected, one still obtains a convergent result, despite the temperature being nonzero, because the low-q divergence is already suppressed by the transport-associated angular weighting factor. We obtain

$$\frac{\hbar}{2\,\tau^{\rm PA}_{+\rm tr}(k_F)_{(\rm no\ scr)}} \simeq \frac{\lambda 7\zeta(3)}{4} k_B T\left(\frac{T}{T_{\rm BG}}\right)^2\;, \qquad (5.2.38)$$

and recall that the non-transport equivalent of this equation is divergent, as discussed in the Sec. 5.2.1 [see the discussion before Eq. (5.2.21)]. The limit (5.2.38) is coincident with the T^3 dependence found in Ref. [50], where the vertex screening (in the particular case of GaAs) is not taken into account. The neglect of vertex screening is acceptable in the temperature regime $2r_s T_{\rm BG} \lesssim T \ll T_{\rm BG}$ in those materials with $4r_s \ll 1$, because in that case the integral in Eq. (5.2.36) is dominated by exchanged momenta q such that $k_{\rm TF} \ll q \ll k_F$, which are little sensitive to vertex screening. This intermediate regime of temperatures does not exist for substrate materials such that $2r_s \sim 1$.

A similar situation is found for the electron decay caused by intrinsic deformation phonons: at these low temperatures, the inverse electron-momentum relaxation time due to intrinsic phonons may decay like T^4 or T^6 depending on the details of the DFT calculation [88], which can be interpreted as an effect of the screened interaction at low-q processes. From the comments regarding the screening of these phonons, given in Sec. 3.1.3, it

does not seem correct to explicitly screen them, and the actual mechanism for the change of the decay law should be another.

High temperature

For the high-temperature range $T \gg T_{\rm BG}$, it is:

$$\frac{\hbar}{2\,\tau^{\rm PA}_{+{\rm tr}}(k_F)} \simeq \frac{\lambda}{2} k_B T \int_0^1 x\sqrt{1-x^2}\,dx = \frac{\lambda}{6} k_B T \ , \tag{5.2.39}$$

to be compared with Eq. (5.2.23). The absence of a qualitative change in the temperature dependence as one shifts from non-transport to transport lifetime is due to the relatively small weight, at high temperatures, of the transport-reduced, low-q processes.

Thus one sees that the transport scattering rates are comparable to the previous imaginary self-energies except for an extra $(T/T_{\rm BG})^2$ factor appearing at low temperatures, due to extra angular suppression of the otherwise-dominant low-q events. A similar comparison holds for the intrinsic acoustic deformation-potential phonons, where:

$$\frac{\hbar}{2}\tau^{\rm DA}_{+{\rm tr}}(k_F)^{-1} \simeq 10\left(\frac{T}{T_{\rm BG}}\right)^2 {\rm Im}\,\Sigma^{\rm DA}_{+}(k_F,0) \tag{5.2.40}$$

at low temperatures, while:

$$\frac{\hbar}{2}\tau^{\rm DA}_{+{\rm tr}}(k_F)^{-1} \simeq \frac{1}{2}\,{\rm Im}\,\Sigma^{\rm DA}_{+}(k_F,0) \tag{5.2.41}$$

for high temperatures. In the last two equations, we compare the results of Refs. [50, 104] for the transport scattering rate and the inverse lifetime, respectively.

Comparison with graphene intrinsic phonons

In analogy with Sec. 5.2.1, one may compare the transport rates due to deformation and piezoelectric phononic modes. In the low-temperature limit

(as before, $[k_F]$ is k_F in units of $10^6\,\mathrm{cm}^{-1}$),

$$\frac{\tau_{+\mathrm{tr}}^{\mathrm{PA}}(k_F)^{-1}}{\tau_{+\mathrm{tr}}^{\mathrm{DA}}(k_F)^{-1}} \simeq \frac{200}{[k_F]^2}\lambda\bar{\varepsilon}_0^2\frac{k_BT}{1\ \mathrm{meV}}\ , \tag{5.2.42}$$

while at temperatures above T_{BG}:

$$\frac{\tau_{+\mathrm{tr}}^{\mathrm{PA}}(k_F)^{-1}}{\tau_{+\mathrm{tr}}^{\mathrm{DA}}(k_F)^{-1}} \simeq \frac{45}{[k_F]}\lambda\ , \tag{5.2.43}$$

independent of temperature. Upon inserting the specific material parameters, Eq. (5.2.43) is in agreement with the calculations of Ref. [50], where PA and DA transport rates are compared for GaAs. Equations (5.2.42) and (5.2.43) must be compared to Eqs. (5.2.27) and (5.2.28) of Sec. 5.2.1, respectively. Like in the non-transport lifetime estimates there presented, note that piezoelectric phonons dominate over deformation phonons at non-small couplings and low densities. We recall that Ref. [50] used a deformation constant $D = 6.8$ eV, quite smaller than the value $D = 25\,\mathrm{eV}$ [104] used here. That replacement reduces $1/\tau^{\mathrm{DA}}$ by about a factor of ten and makes the substrate PA phonons relatively more important.

Mobility

Finally, in order to compute the electron mobility, one averages the momentum relaxation time [see Eq. (5.2.36)] ,

$$\overline{\tau_{\mathrm{tr}}} \equiv \int d\epsilon D(\epsilon)\tau_{+\mathrm{tr}}(k(\epsilon))[-dn_F(\epsilon)/d\epsilon]\ , \tag{5.2.44}$$

and because the energy derivative peaks at E_F while $\tau_{+\mathrm{tr}}(k)$ varies slowly with k, one can write the classical Drude formula for the mobility:

$$\mu = \frac{e\,\tau_{+\mathrm{tr}}(k_F)}{m^*} = \frac{ev_F}{\hbar k_F}\tau_{+\mathrm{tr}}(k_F)\ , \tag{5.2.45}$$

in terms of $\tau_{+\mathrm{tr}}(k)$ computed at the Fermi level and the "effective mass" $m^* = \hbar k_F/v_F$ of the graphene Dirac fermions.

5.3 Numerical results

In the following, numerical results for the various rates and mean free paths derived in Secs. 5.2.1 and 5.2.3 are presented and discussed. Unless otherwise stated, the numerical values of this section are computed for ZnO (see Sec. C.1, Fig. C.1) substrates in the Z-Cut, which is isotropic (see Fig. 3.2) and whose parameters are $\lambda = 0.03$ and $\overline{\varepsilon}_0 = 4.8$, which implies $k_{\mathrm{TF}}/k_F \simeq 2$ and $k_B T_{\mathrm{BG}}/E_F \simeq 0.0054$.

Imaginary part

In the upper plot of Fig. 5.2, the imaginary part of the on-shell self-energy is shown, as a function of the parameter $\epsilon_k/E_F > 0$, for different temperatures. The curves are universal in the sense that they are density-independent. The zero-temperature curve shows, for small ϵ_k, the limiting ϵ_k^3 behavior of Eq. (5.2.15), which arises due to the combined effect of screening and the phase-space restrictions faced by the electrons when losing energy via phonon emission. This restriction disappears when ϵ_k is greater than any phononic energy, i.e., $\epsilon_k \gg k_B T_{\mathrm{BG}}$. Above this threshold, the imaginary part of the self-energy becomes energy-independent, as predicted by Eq. (5.2.18). At still higher energies ($\epsilon_k \gg E_F$, not shown in the upper plot of Fig. 5.2), it increases linearly with the length of the constant-energy circumference at the quasiparticle energy $E_{k+} \propto k$. Such a linear increase with k would appear with a negligible slope in the tiny scale of $\epsilon_k \propto (k - k_F)$ of the upper plot of Fig. 5.2. Specifically, the slope is, in the dimensionless units of the upper plot of Fig. 5.2, $(\lambda\pi/16)(v_s/v_F)$.

The upper plot of Fig. 5.2 also shows that a further increase in temperature ($T > T_{\mathrm{BG}}$) smears these features due to phonon excitation and electron heating near the Fermi energy, as exemplified in Eq. (5.2.23). The effect of vertex screening in the regime of low ϵ_k, low T can be appreciated in Fig. 5.3, for both ZnO and (angle-averaged) PZT substrates with their much higher dielectric constant (and thus smaller λ). For the sake of comparison, the graphics include also the linear approximation (5.2.20), which holds better for PZT because its large dielectric constant reduces the

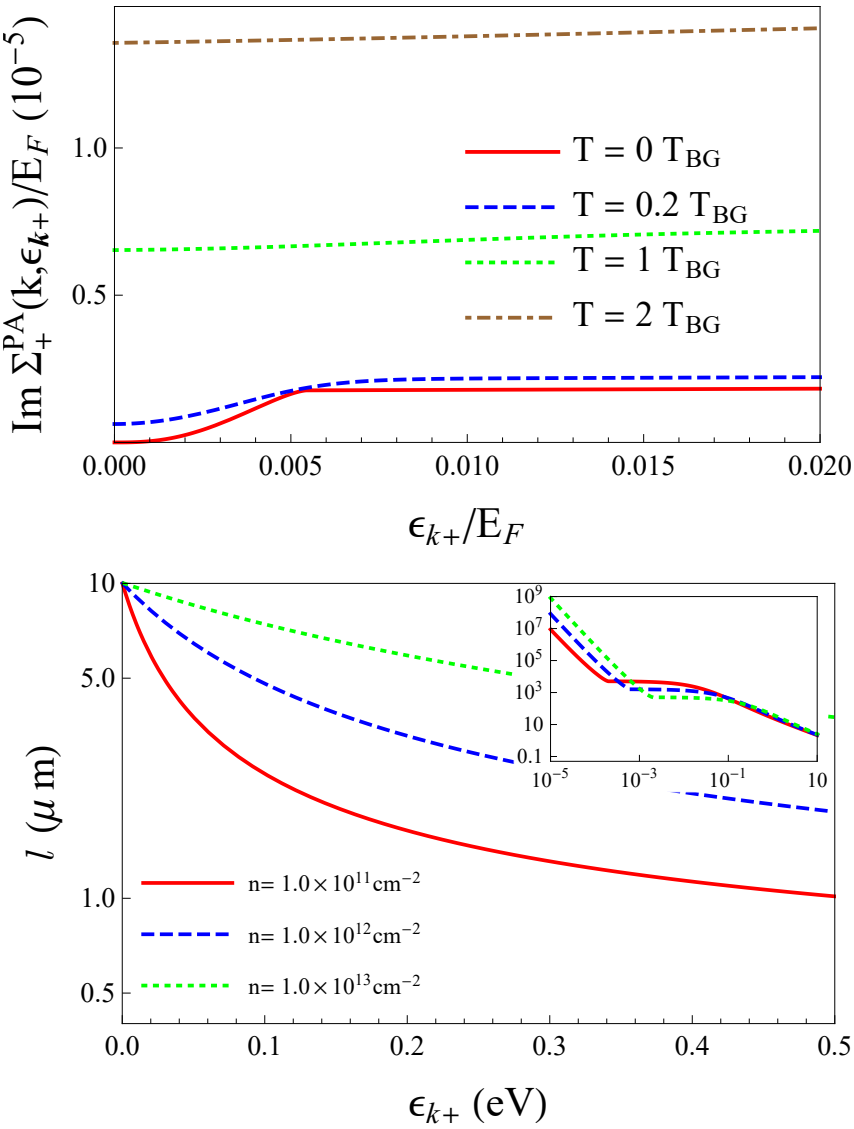

Figure 5.2: Imaginary part of the self-energy and inelastic scattering length of charge carriers in graphene on ZnO (Z-cut) as a function of the energy, $\epsilon_k/E_F = (k - k_F)/k_F$. Upper: $\mathrm{Im}\,\Sigma_+^{\mathrm{PA}}$ for different temperatures. The curves are valid for all densities. Lower: Inelastic mean free path l for different carrier concentrations at room temperature ($T = 300$ K $= 26$ meV$/k_B$). The inset shows l at $T = 0$ for the same densities. The Bloch-Grüneisen temperature T_{BG} is given in Eq. (5.2.14). For this material, $k_B T_{\mathrm{BG}} = 0.0054 E_F$ (for all carrier densities) and $k_{\mathrm{TF}}/k_{\mathrm{F}} \simeq 2$ (thus $T_{\mathrm{BG}} \simeq \hbar v_s k_{\mathrm{TF}}/k_B$). For these three densities, $k_B T_{\mathrm{BG}} = 0.2, 0.63, 2$ meV, while $E_F = 37.4, 117, 374$ meV.

size of the phase-space region where the screening of the phonon interaction by the electron cloud (vertex correction) is really important. Unlike for ZnO, in this material k_{TF} is considerably smaller than k_F, which leaves room for an intermediate range of ϵ_k values for which the approximation $\varepsilon_{\mathrm{RPA}} \simeq 1$ is acceptable while the linear behavior still holds. As announced in Sec. 5.2.1, after Eq. (5.2.20), there is an offset between the true imaginary self-energy and the linear approximation due to the reduced contribution of the screened low-q processes.

The upper plot of Fig. 5.4 shows the temperature dependence of $\mathrm{Im}\,\Sigma_+^{\mathrm{PA}}$ for fixed values of ϵ_k. At low temperatures ($T \ll \epsilon_k$, hot-electron regime), these decay linewidths are independent of T. Note that in this figure the nonzero values of ϵ_k are well above $\hbar v_s k_{\mathrm{TF}}$ and thus the limit in Eq. (5.2.15) does not apply. At higher temperatures ($T > T_{\mathrm{BG}}$), the linear behavior of Eq. (5.2.23) is recovered.

Inelastic mean free path

The lower plots of Figs. 5.2 and 5.4 are devoted to the inelastic scattering mean free path, which is the inverse of the imaginary part of the on-shell self-energy:

$$l(k) = \frac{\hbar v_F}{2\,\mathrm{Im}\,\Sigma_+^{\mathrm{PA}}(k, \epsilon_k)} \ . \tag{5.3.1}$$

The lower plot of Fig. 5.2 shows values for $l(k)$ as a function of ϵ_k for three cases of typical doping conditions. Note that they tend to coincide at small ϵ_k, as suggested by Eq. (5.2.23) (case $T > T_{\mathrm{BG}}$), which predicts a doping-independent low-ϵ_k ($k \to k_F$) limit at nonzero temperatures. Finally, the inset of the lower plot of Fig. 5.2 clearly displays the three energy regimes that hold at zero temperature and which can be inferred from Eqs. (5.2.15)-(5.2.19).

The temperature dependence of l is shown in the lower plot of Fig. 5.4. A crossover from (T-independent) low-temperature to (T^{-1}) high-temperature behavior can be appreciated for $T \sim T_{\mathrm{BG}}$, in agreement with Eqs. (5.2.15) and (5.2.23). One must note, however, that Eq. (5.2.15) does not truly

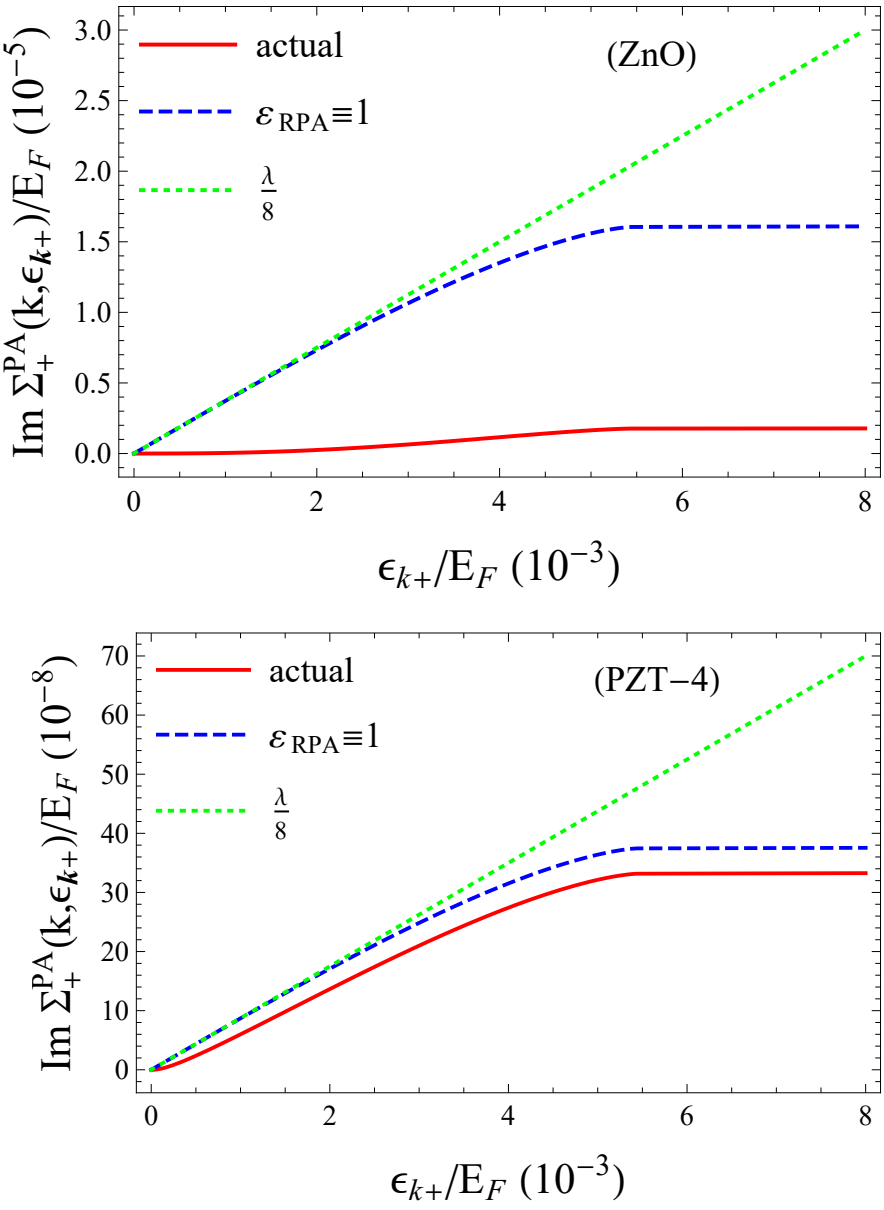

Figure 5.3: Low-energy behavior of the imaginary part of the self-energy at zero temperature. The solid, dashed and dotted lines correspond, respectively, to the exact values, the values without vertex screening, and the values obtained (in the unscreened case) from the linear $\lambda/8$ approximation of Eq. (5.2.20). Upper: Graphene on ZnO (Z-cut). Lower: Graphene on PZT-4 (Z-cut), for which $k_B T_{\mathrm{BG}}/E_F = 0.0045$, $k_{\mathrm{TF}}/k_{\mathrm{F}} \simeq 0.025$, and $\hbar v_s k_{\mathrm{TF}}/E_F \simeq 5.7 \times 10^{-5}$. See Table 4.1 for λ values.

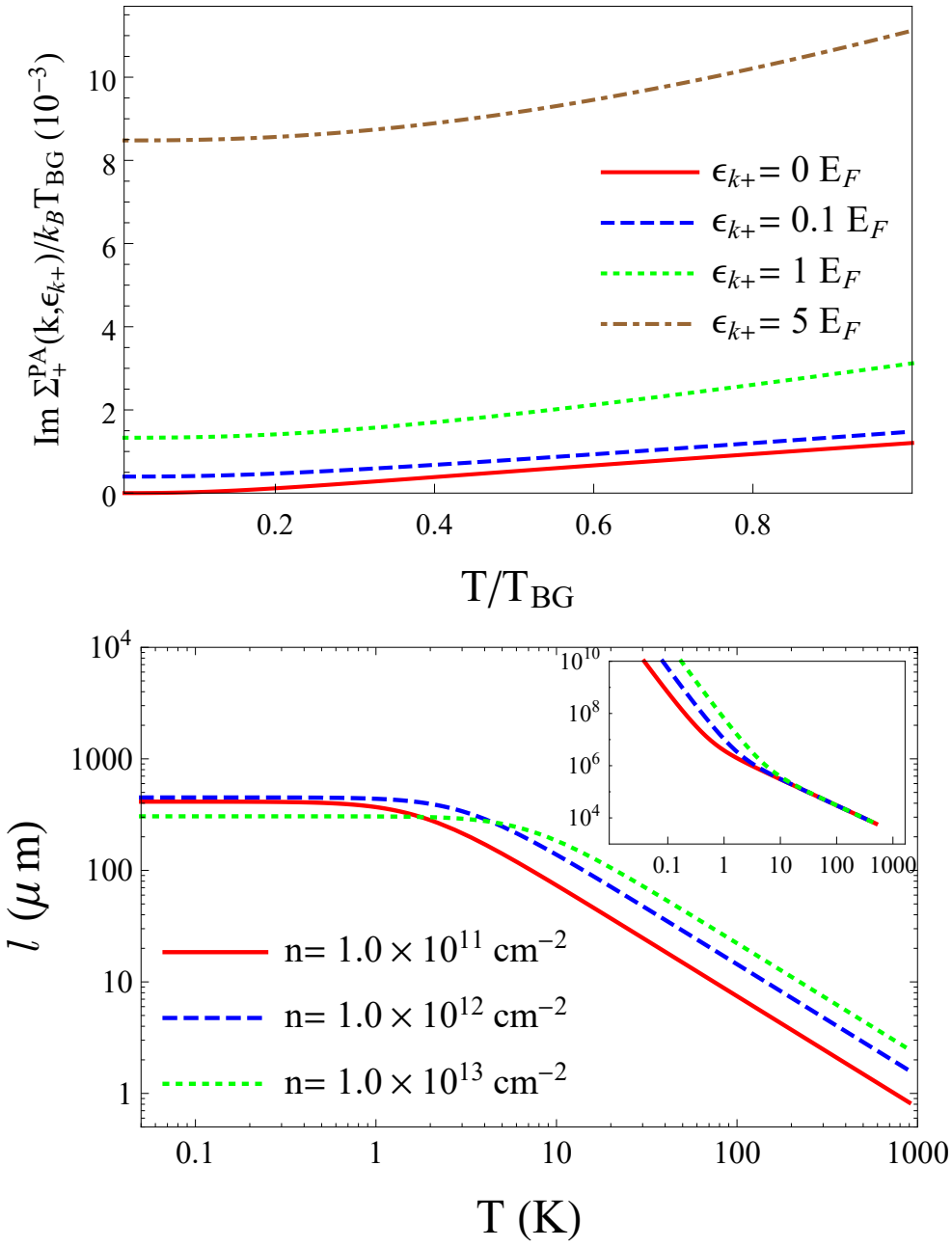

Figure 5.4: Imaginary part of the self-energy and inelastic scattering length. Upper: $\mathrm{Im}\,\Sigma_+^{\mathrm{PA}}$ as a function of T/T_{BG} for different values of ϵ_k/E_F. Lower: l as a function of T for $\epsilon_k = 0.1\,\mathrm{eV} \simeq 1160\,\mathrm{K}$ and different doping levels. The inset shows the corresponding curves for $\epsilon_k = 0$. Here, $E_F \simeq 185\,k_B T_{\mathrm{BG}}$. The values of T_{BG} for these three densities are $2.35, 7.35, 23.5$ K.

apply to the low-temperature sector of this graph, because here $\epsilon_k > \hbar v_s k_{\mathrm{TF}}$, unlike the assumption in Eq. (5.2.15). This explains the discrepancy in the density dependence. For this material, $\hbar v_s k_{\mathrm{TF}}$ takes values 0.2, 0.63, 2 meV for the three listed densities, all much smaller than the value $\epsilon_k = 100$ meV there considered.

The inset shows the corresponding curves for $\epsilon_k = 0$. A clear crossover for T^{-3} to T^{-1} behavior is observed at $T \sim T_{\mathrm{BG}}$, in agreement with Eqs. (5.2.21) and (5.2.23).

Density dependence (divergent without screening)

For a fixed value of k and at room temperature, Fig. 5.5 shows the variation of $\mathrm{Im}\,\Sigma_+^{\mathrm{PA}}$ and of the mean free path as a function of the carrier density. A logarithmic divergence in the linewidth, accompanied by a vanishing mean free path, is seen to appear in the undoped regime, where the description of the system employed in the present paper is not valid anymore (see, e.g. Ref. [111]). This spurious low-doping behavior can be expected from an extrapolation of Eq. (5.2.23) to low doping.

Mobility values and comparison with intrinsic phonons

In the upper plot of Fig. 5.6, the electron mobility μ [see Eq. (5.2.45)], due only to piezoelectric phonons, is shown. The T^{-5} and T^{-1} behaviors can be appreciated at low and high temperatures, respectively, as expected from Eqs. (5.2.37) and (5.2.39) taking into account Eq. (5.2.45) for the density dependence.

Finally, in the lower plot of Fig. 5.6, we compare the substrate-induced mobility to that stemming only from graphene intrinsic phonons, with $D = 25\,\mathrm{eV}$. The total combined mobility due to (piezoelectric and intrinsic-deformation) acoustic phonons is $\mu = \left(\mu_{\mathrm{PA}}^{-1} + \mu_{\mathrm{DA}}^{-1}\right)^{-1}$. Specifically, the ratio between the two inverse mobilities is plotted. The smaller value of $D = 6.8\,\mathrm{eV}$ would reduce the intrinsic inverse mobility by an order of magnitude and correspondingly would increase the relative importance of piezoelectric phonons. This ratio between transport scattering rates shows two clear low- and high-T regimes with linear-in-T and T-independent behav-

iors, respectively, in agreement with Eqs. (5.2.42) and (5.2.43). At low and high temperatures, the relative importance of the PA phonons increases with decreasing density. There is an intermediate temperature regime in which the density dependence is inverted. Thus one sees that the piezoelectric phonons dominate over a wide range of temperatures and densities. If $D = 6.8\,\mathrm{eV}$ for the intrinsic phonons is chosen, then the momentum relaxation due to PA phonons here computed prevails essentially always except at very high temperature and density or for extremely low temperatures.

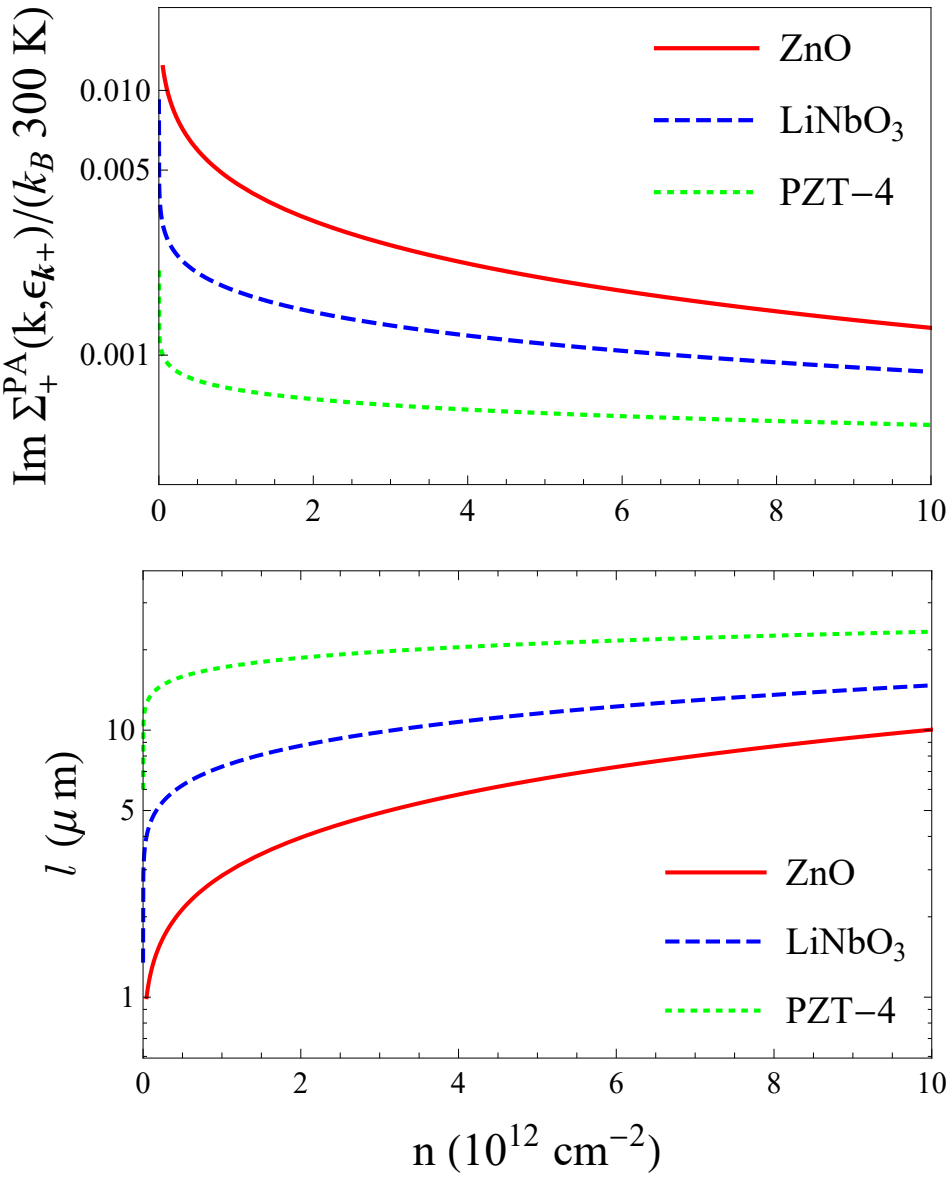

Figure 5.5: Imaginary part of the self-energy and inelastic scattering length as a function of the doping, for different materials, at fixed (room) temperature and electronic state $k = \sqrt{\pi \times 10^{13}\,\mathrm{cm}^{-2}}$ (recall $k_F = \sqrt{\pi n}$). Upper: $\mathrm{Im}\,\Sigma_+^{\mathrm{PA}}$ as a function of carrier density n. Lower: l as a function of n in the same units for the same materials.

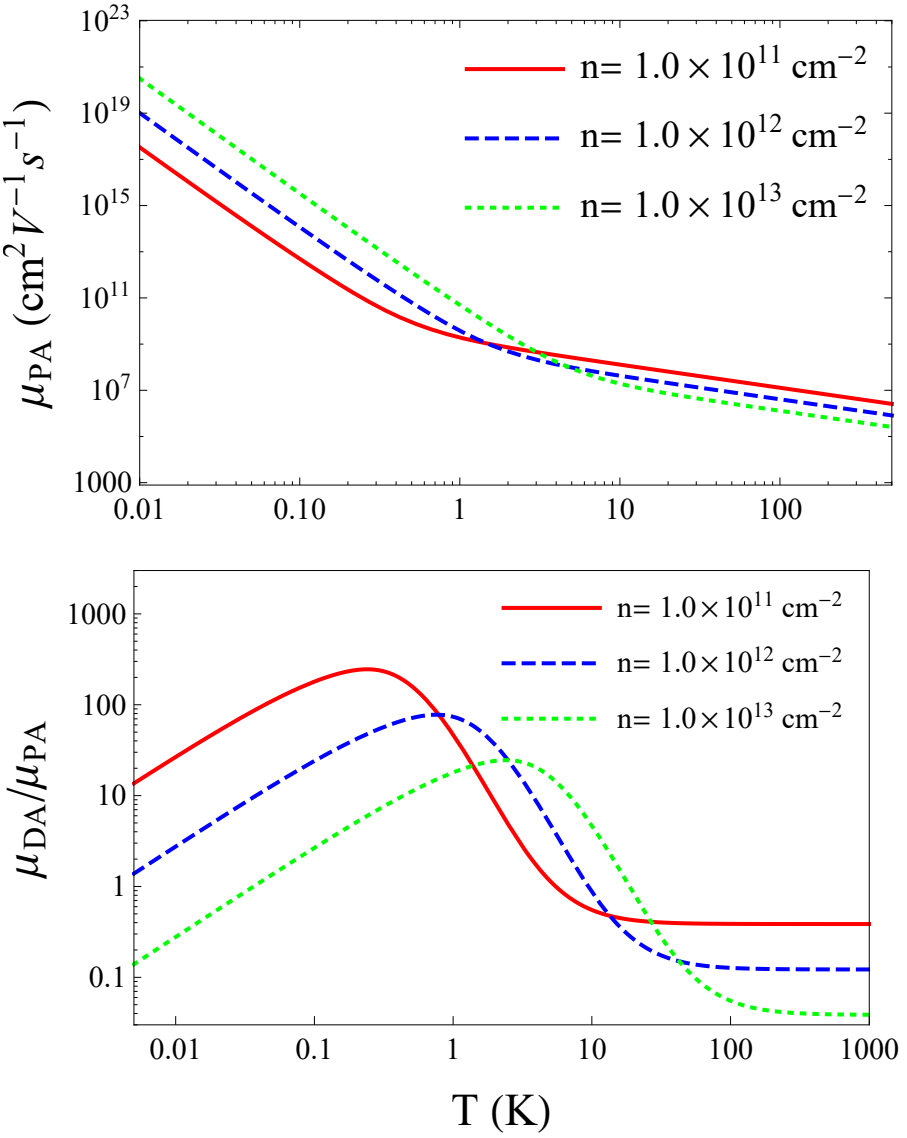

Figure 5.6: Electron mobility due only to piezoelectric acoustic phonons and its comparison with that due to intrinsic phonons. Upper: The mobility $\mu_{\rm PA}$ as a function of the temperature, for several carrier concentrations. Lower: The ratio $\mu_{\rm DA}/\mu_{\rm PA}$, where $\mu_{\rm DA}$ is the mobility obtained when only the deformation potential of intrinsic phonons (with $D = 25\,\text{eV}$) is included. The ratio between mobilities must be increased by a factor $(25/6.8)^2 \simeq 13.5$ when the value $D = 6.8\,\text{eV}$ is used [50]. The values of $T_{\rm BG}$ for these doping levels are given in the caption of Fig. 5.4, while $T_F = 434, 1360, 4340$ K.

Chapter 6

Conclusions

6.1 General conclusions

We have derived a general expression for the two-dimensional piezoelectric electron-phonon interaction valid for any piezoelectric substrate covered by a two-dimensional electron system, as in the classical 2D Fröhlich Hamiltonian for the optical phonons, and characterized the magnitude of the interaction.

From the derived interaction vertex, it can be shown that the relative size of the static phonon-mediated electron-electron interaction with respect to the original Coulomb repulsion turns out to be exactly $K_R^2 < 1$. By applying the Eliashberg formalism to graphene [98], one is able to assess, in terms of K_R, the influence that these low-frequency and long-wavelength phonons have on possible BCS-type instabilities. The conclusion is that present piezoelectric materials are not able to either induce s-wave pairing by themselves or affect in a significant way any pairing instability which could be already present in graphene, a conclusion that could change in case novel strongly piezoelectric materials were found.

Our results show that electron overscreening cannot be achieved even with the strongest piezoelectric phonons because, as we have proved in this work, $K_R^2 < 1$ is always satisfied. Nevertheless, these phonons could enhance

superconductivity in contexts where it already exists in the absence of the substrate. This can be the case, for example, in bulk few-layer MoS_2 with most of the carriers confined to the first layer [112, 113], or in Ca-decorated graphene laminates, consisting of well separated and electronically decoupled graphene crystallites [114]. It can be the case too in other contexts where superconductivity is postulated to exist but not yet observed due to experimental difficulties (e.g. very heavily doped graphene [98] or metal-adatom-decorated graphene [115]). Other examples are the recent high-temperature superconductor system of 2D FeSe on top of the ferroelectric $SrTiO_3$ (whose optical phonons have been analyzed, with conclusions similar to ours [100] and where the strong piezoelectric phonons could play an important role as well), and the recent "magic-angle" twisted bilayer graphene systems [116].

For typical materials, with relatively low values of K_R^2 and λ as shown in Tab. 4.1, it seems that the effect of the piezoelectric phonons should not be big. However, any hypothetical material with similar values of the dielectric constant and elastic tensors (such as e.g. ZnO in the Z-Cut) but whose piezoelectric constants were around 5 times bigger (so that values of $K_R^2 \sim 0.5$ and $\lambda \sim 0.9$ could be reached), which is not an unrealistic assumption; would change the scenario considerably. In particular, the former Eliashberg-McMillan theory would not apply [72, 117]. An important change in this scenario could occur as well if it were possible to enhance the interaction via stimulated phonon absorption and emission, something which could be made feasible by introducing a grid of SAWs under the 2DEG, a case that has not been contemplated in the present work.

Our diagrammatic approach for electron-phonon interactions also takes into account the renormalization of both phonon modes and carrier states due to electron-phonon interactions, and it emphasizes the importance of all the involved screening processes for a correct evaluation of the mean free path and carrier mobility. We have obtained numerous analytical limits as a function of carrier energy, density, and temperature, which have allowed us to understand the trends shown by the numerical results.

We may emphasize that the inverse mobility due to piezoelectric acoustic phonons increases with carrier density at high temperatures, while it is a decreasing function of density at low temperatures [see the upper plot in Fig. (5.6)], the latter trend being understandable in terms of increased electron screening at high densities. On the other hand, the temperature dependence of the inverse mobility is much more pronounced at low temperatures.

When compared with the values obtained when only intrinsic deformation phonons are taken into account, one finds that the contributions of the piezoelectric acoustic phonons to the inverse lifetime and to the mobility dominate over a considerable range of temperatures and doping levels, a parameter range that becomes almost pervasive if low values of the deformation coupling constant are chosen from the literature.

As our results are applicable to piezoelectric materials of various lattice symmetries and interaction strengths, they will be helpful in the development of electronic devices involving graphene deposited on piezoelectric substrates. Among such potential devices, we may mention the graphene field-effect transistor on a piezoelectric substrate as studied experimentally in Refs. [107] and [118] with PZT and $LiNbO_3$, respectively. That class of setups was also investigated as a possible basis for the building of nonvolatile memories [119]. Finally, a suitable understanding of the interaction between graphene electrons and acoustic piezoelectric phonons will enhance applications based on the use of piezoelectric surface acoustic waves beneath a graphene layer.

Appendix A

Basic electronic properties of graphene

A.1 Generalities

Although it was thought to not exist at that time, the basic electronic properties of graphene were derived many decades ago as a starting point to understand graphite [120]. The analysis of a single layer of graphene is the natural starting point too when it is placed on a (3D) substrate, which can strongly modify the properties of the monolayer material. So let us first consider a single, perfect layer of carbon arranged in the graphene structure (as in Fig. 1.1, bottom right). We reproduce below the derivation of one of its most interesting aspects: its low-energy quasiparicles are equivalent to the so-called massless, chiral, Dirac fermions.

In fact, the graphene honeycomb lattice is formed from a triangular Bravais lattice with a basis of two atoms per unit cell, separated by the distance $a = 1.42\,\text{Å}$, such that the lattice-basis vectors are:

$$\mathbf{a}_1 = \frac{a}{2}\left(3, \sqrt{3}\right) \ , \quad \mathbf{a}_2 = \frac{a}{2}\left(3, -\sqrt{3}\right) \ , \tag{A.1.1}$$

and the reciprocal-lattice (also triangular) vectors are thus given by:

$$\mathbf{b}_1 = \frac{2\pi}{3a}\left(1, \sqrt{3}\right) \ , \quad \mathbf{b}_2 = \frac{2\pi}{3a}\left(1, -\sqrt{3}\right) \ . \tag{A.1.2}$$

From this hexagonal structure, each atom from one sublattice is connected to three nearest-neighbor atoms from the other sublattice, their position vectors being [see Fig. A.1(a)]:

$$\boldsymbol{\delta}_1 = \frac{a}{2}\left(1, \sqrt{3}\right) \ , \quad \boldsymbol{\delta}_2 = \frac{a}{2}\left(1, -\sqrt{3}\right) \ , \quad \boldsymbol{\delta}_3 = \frac{a}{2}\left(-1, 0\right) \ . \tag{A.1.3}$$

In this array of carbon atoms, the sp^2-hybridized states give rise to occupied bonding and empty antibonding bands, separated respectively by a large gap [see Fig. A.1(b) for a planar representation]. On the other hand, the π-states form a single band, whose energies near the Fermi surface give rise to a conical linear dispersion in the first approximation, as will be seen below.

In a tight-binding Hamiltonian described by a 2×2 matrix with hopping parameter t, the basis of electron states consists of two π-states belonging to atoms from the first [amplitude $\psi_A(\mathbf{k})$] and the second [amplitude $\psi_B(\mathbf{k})$] sublattices, having no coupling within each sublattice in the nearest-neighbor approximation:

$$H(\mathbf{k})\psi(\mathbf{k}) = \begin{bmatrix} 0 & -tf(\mathbf{k}) \\ -tf^*(\mathbf{k}) & 0 \end{bmatrix} \begin{bmatrix} \psi_A(\mathbf{k}) \\ \psi_B(\mathbf{k}) \end{bmatrix} = E(\mathbf{k}) \begin{bmatrix} \psi_A(\mathbf{k}) \\ \psi_B(\mathbf{k}) \end{bmatrix} \ , \tag{A.1.4}$$

$$\text{with} \quad f(\mathbf{k}) = \sum_{i=1}^{3} \exp(\mathbf{k} \cdot \boldsymbol{\delta_i}) = 2\exp\left(\frac{ik_x a}{2}\right)\cos\left(\frac{k_y a\sqrt{3}}{2}\right) + \exp(-ik_x a) \ .$$

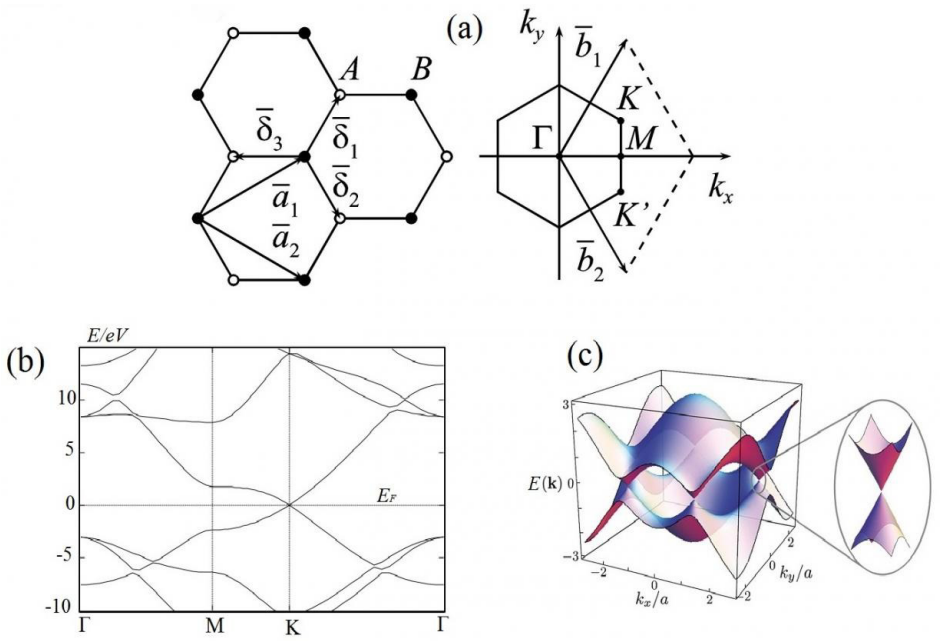

Figure A.1: The basic crystal and band structure of graphene. (a) The honeycomb lattice of graphene with the two sublattices and basis vectors, together with the reciprocal lattice. (b) Planar representation of the band structure near the high-symmetry points. (c) 3D representation of the π-band structure including a zoom at the conical dispersion from the Dirac point in K.

Therefore, the energies of the eigenstates turn out to be [see Fig. A.1(c)]:

$$E(\mathbf{k}) = \pm t\,|f(\mathbf{k})| = \pm\left[3 + 2\cos(\sqrt{3}k_y a) + 4\cos\left(\frac{\sqrt{3}k_y a}{2}\right)\cos\left(\frac{3k_x a}{2}\right)\right]^{1/2}, \tag{A.1.5}$$

where the plus sign applies to the upper (π^*-antibonding) band and the minus is for the lower (π-bonding) band.

There are two very special high-symmetry points at the edge of the Brillouin zone which are very important for the physics of graphene [see

Fig. A.1(a)], given by:

$$\mathbf{K} = \frac{2\pi}{3a}\left(1, \frac{1}{\sqrt{3}}\right) \ , \quad \mathbf{K}' = \frac{2\pi}{3a}\left(1, -\frac{1}{\sqrt{3}}\right) \ . \tag{A.1.6}$$

These two points, located at the corners of the Brillouin zone, are called *Dirac points*. As can be seen from Eq. (A.1.5), they are the only points where the energy becomes 0 and they are equivalent to the other four points in the corners (two are equivalent to $\mathbf{K}$ and the other two are equivalent to $\mathbf{K}'$), since they can be joined to each other by reciprocal lattice vectors. That is, $E(\mathbf{K}) = E(\mathbf{K}') = 0$.

In the zero-doping ideal regime, and since each carbon atom contributes precisely with one electron to the band, all negative-energy states are filled and all positive-energy ones are empty. The Fermi "surface" is located precisely at those two points with a zero gap, like any other semiconductor. This clear symmetry between electron and hole states is broken by taking into account the next-nearest-neighbor hopping energy t' in the tight-binding Hamiltonian. From first-principle calculations and experiment, t turns out to be $t \simeq 2.8$ eV $\gg t' \simeq$ 0.07 eV, so that t' can be well neglected to a first approximation and thus the nearest-neighbor approximation is really accurate throughout the whole Brillouin zone.

One of the fundamental properties of graphene becomes manifest when expanding the energies near the Dirac points. In fact, taking $\mathbf{q} = \mathbf{k} - \mathbf{K}$ and $\mathbf{q}' = \mathbf{k} - \mathbf{K}'$ with $q \ll K,\ q' \ll K'$, the Hamiltonian in Eq. (A.1.4) becomes (after excluding a constant phase factor by an unitary transformation of the basis):

$$H(\mathbf{q}) = \frac{3at}{2}\begin{pmatrix} 0 & q_x + iq_y \\ q_x - iq_y & 0 \end{pmatrix} + \mathcal{O}(q^2) \ , \tag{A.1.7}$$

$$H(\mathbf{q}') = \frac{3at}{2}\begin{pmatrix} 0 & q_x - iq_y \\ q_x + iq_y & 0 \end{pmatrix} + \mathcal{O}(q^2) \ , \tag{A.1.8}$$

with $\frac{3at}{2} = \hbar v_F$, being $v_F \simeq 10^6$ ms^{-1}. This is a linear dispersion for the

energy around the Dirac points [see Eq. (A.1.5)], as first obtained by P. Wallace [120] in 1947 [see the zoom in Fig. A.1(c)]:

$$E(\mathbf{q}) = E(\mathbf{q}') = \pm\hbar v_F q + \mathcal{O}(q^2) \ . \tag{A.1.9}$$

A.2 Dirac fermions

Within any realistic experimental scenario, graphene appears to be electron or hole-doped via impurities or surrounding electric fields, and $E_F \ll t$, being the density of carriers much smaller than one electron per carbon atom (usually around $n \sim 10^{10} - 10^{14}$ cm^{-2}). As can be seen from straightforward algebra [121], it is possible to derive an effective Hamiltonian around the Dirac points, with the replacements $q_x \to -i\partial_x$; $q_y \to -i\partial_y$ and such that:

$$H_{\mathbf{K}} = -i\hbar v_F \, \boldsymbol{\sigma} \cdot \boldsymbol{\nabla} \ , \tag{A.2.1}$$

$$\boldsymbol{\sigma} = (\sigma_x, \sigma_y) = \left[\begin{pmatrix} 0 & 1 \\ 1 & 0 \end{pmatrix}, \begin{pmatrix} 0 & -i \\ i & 0 \end{pmatrix} \right], \ \boldsymbol{\nabla} = (\partial_x, \partial_y) \ . \tag{A.2.2}$$

This is the effective Hamiltonian around the conical point (called *valley*) **K**. It corresponds to the effective-mass approximation, or $\mathbf{k} \cdot \mathbf{p}$ theory. It is possible to derive a description around the two valleys **K**, **K′**, with the basis vectors:

$$\Psi = (\psi_{KA}, \psi_{KB}, \psi_{K'A}, \psi_{K'B})^T \ , \tag{A.2.3}$$

and with the 4×4 Hamiltonian:

$$H = \begin{pmatrix} H_{\mathbf{K}} & 0 \\ 0 & H_{\mathbf{K}'} \end{pmatrix}, \quad \text{being } H_{\mathbf{K}'} = H_{\mathbf{K}}^T \ , \tag{A.2.4}$$

which is more complete than the Hamiltonian arising from taking just one valley.

The eigenspinors of the reduced 2×2 Hamiltonian take the form (around

K, for example):

$$\psi_{\pm}(\mathbf{q}) = \frac{1}{\sqrt{2}} \begin{bmatrix} \exp\left(-i\theta_{\mathbf{q}}/2\right) \\ \pm \exp\left(i\theta_{\mathbf{q}}/2\right) \end{bmatrix} , \tag{A.2.5}$$

with the signs corresponding to the energies $E_{\mathbf{k}} = \pm\hbar v_F k$ (the eigenspinor around $\mathbf{K}'$ is the time-reversal transformed one) and $\theta_{\mathbf{q}} = \arctan(q_x/q_y)$.

In the terminology of graphene, the sublattice degree of freedom regarding the sublattice position (and not the real spin, as it is usually the case for spinors) is called *pseudospin*. This means that the eigenfunctions have a well-defined (pseudo-)*helicity*, given by the projection operator of the momentum along the pseudospin direction $h = \frac{1}{2}\boldsymbol{\sigma} \cdot \hat{\mathbf{q}}$. Thus, the electrons (holes) have a positive (negative) energy with the direction of the momentum positively (negatively) oriented along the pseudospin.

In summary, the graphene carriers are described as in Quantum Electrodynamics (QED), by massless (ultra-relativistic) Dirac chiral fermions of spin 1/2, with the real velocity of light ($c \simeq 3 \times 10^8$ m/s) replaced by the Fermi velocity $v_F \simeq c/300$.

A.3 Effective mass and density of states

This description of graphene electrons in terms of massless Dirac fermions was demonstrated experimentally soon after the discovery of graphene [9] regarding measures of the ciclotron mass of the carriers, and the latter discovery of the anomalous (half-integer) quantum Hall effect, chirality, Berry's phase, and impressive relativistics effects such as Klein tunneling [122].

Above all, there is one fundamental difference between the graphene-energy dispersion in Eq. (A.1.9) and the energy dispersion of the usual two-dimensional electron gas (2DEG) in classical electronics, where $E_{\mathrm{2DEG}}(\mathbf{q}) = \frac{\hbar^2 q^2}{2m}$, and m is a constant effective electron mass. In the case of graphene, the Fermi velocity is constant and does not depend on the energy or momentum, whereas $v_{F,\mathrm{2DEG}} = \hbar q/m = \sqrt{2E/m}$. The graphene effective mass is zero,

but for some purposes one may define an "effective mass" $m^* = \hbar k_F / v_F$, with k_F denoting the Fermi wave vector.

The density of states in graphene changes substantially from the finite-mass 2DEG. Most importantly, it does depend on the doping level. One obtains:

$$D(E) = \frac{dn(E)}{dE} = \frac{2E}{\pi(\hbar v_F)^2} = \frac{2k_F}{\pi \hbar v_F} \ , \tag{A.3.1}$$

where a factor of 4 should be added to account for the valley and spin degeneracy. The total density of electrons is related to the Fermi wave vector as $n = k_F^2/\pi$. This result is in stark contrast to the 2DEG with finite mass, whose density of states is constant and given by $D(E) = \frac{g_v m}{\pi \hbar^2}$, with g_v accounting for a possible valley degeneracy (see Ref. [7] for a good comparison between both types of electronic systems).

Appendix B

Macroscopic description of piezoelectric materials

B.1 Basic elements of elasticity theory and thermodynamics

From a macroscopic point of view, a material is considered as a compact, continuous set of material points with the surface as its boundary, without taking into account any atomic structure as in actual materials. In this continuum limit, the physical magnitudes are averaged over small volume elements which macroscopically look infinitesimal.

To understand the mathematical description of piezoelectricity, the reader needs to know the basic elements of elasticity (linear) theory and thermodynamics. Let us suppose that any point in an elastic continuous body, as described by the coordinates $(x_1, x_2, x_3) \equiv x_i$ becomes slightly deformed to the new coordinates x_i', such that the displacement in that point becomes $u_i = x_i' - x_i$. From the smallness of the deformations, the *strain tensor* is

defined as the symmetrical second-rank tensor [51]:

$$u_{ij} = \frac{1}{2}\left(\frac{\partial u_i}{\partial x_j} + \frac{\partial u_j}{\partial x_i}\right) = \begin{pmatrix} u_{11} & u_{12} & u_{13} \\ u_{12} & u_{22} & u_{23} \\ u_{13} & u_{23} & u_{33} \end{pmatrix} \overset{\text{(Voigt notation)}}{\equiv} \begin{pmatrix} u_1 & \frac{1}{2}u_6 & \frac{1}{2}u_5 \\ \frac{1}{2}u_6 & u_2 & \frac{1}{2}u_4 \\ \frac{1}{2}u_5 & \frac{1}{2}u_4 & u_3 \end{pmatrix} , \quad \text{(B.1.1)}$$

sometimes written as a six-component vector within the *Voigt notation*. In this notation, the new suffix 1 now stands for the old 11, 2 for 22, 3 for 33, 4 for 23 (or 32), 5 for 31 (or 13) and 6 for 12 (or 21).

On the other hand, an analysis of the forces applied in an elastic body leads to de definition of the *stress tensor* as:

$$T_{ij} = \begin{pmatrix} T_{11} & T_{12} & T_{13} \\ T_{12} & T_{22} & T_{23} \\ T_{13} & T_{23} & T_{33} \end{pmatrix} \overset{\text{(Voigt notation)}}{\equiv} \begin{pmatrix} T_1 & T_6 & T_5 \\ T_6 & T_2 & T_4 \\ T_5 & T_4 & T_3 \end{pmatrix} , \quad \text{(B.1.2)}$$

such that $T_{ik}n_k = \mathbf{T}_i \cdot \hat{\mathbf{n}}$ is the force acting in the surface element given by the normal $\hat{\mathbf{n}} = (n_1, n_2, n_3)$ in x_i and $\frac{\partial T_{ik}}{\partial x_k} = \nabla \cdot \mathbf{T}_i$ is the i-th component of the force applied per unit volume in x_i. An analysis of the torques in equilibrium shows that this tensor is symmetric as well, allowing the use of the Voigt notation as shown in this last equation above (with the convenient omission of the 1/2 fractions as in the case of the strain tensor).

A generalization of Hooke's law for small deformations leds to the definition of the fourth-rank *elastic stiffness tensor* $\hat{c} = c_{ijkl}$, such that the linear relation between the stress and strain tensors holds (where the typical Einstein summation convention is assumed throughout the appendices):

$$T_{ij} = c_{ijkl}u_{kl} , \quad \text{(B.1.3)}$$

From the symmetry of the stress and the strain, one realizes that the tensor $\hat{c}$ is symmetric with regard to the interchanges $i \leftrightarrow j$ or $k \leftrightarrow l$. From thermodynamic arguments [given below in Eq. (B.1.11)], it can be seen that

it is also symmetric with respect to the interchange $(ij) \leftrightarrow (kl)$. This allows one to extend the Voigt notation to this 4-rank tensor $\hat{c}$ so that Eq. (B.1.3) becomes:

$$\begin{pmatrix} T_1 \\ T_2 \\ T_3 \\ T_4 \\ T_5 \\ T_6 \end{pmatrix} = \begin{pmatrix} c_{11} & c_{12} & c_{13} & c_{14} & c_{15} & c_{16} \\ c_{12} & c_{22} & c_{23} & c_{24} & c_{25} & c_{26} \\ c_{13} & c_{23} & c_{33} & c_{34} & c_{35} & c_{36} \\ c_{14} & c_{24} & c_{34} & c_{44} & c_{45} & c_{46} \\ c_{15} & c_{25} & c_{35} & c_{45} & c_{55} & c_{56} \\ c_{16} & c_{26} & c_{36} & c_{46} & c_{56} & c_{66} \end{pmatrix} \begin{pmatrix} u_1 \\ u_2 \\ u_3 \\ u_4 \\ u_5 \\ u_6 \end{pmatrix} , \tag{B.1.4}$$

with $(c_{11}, c_{12}, c_{13}, c_{14}, c_{15}, c_{16}) \equiv (c_{1111}, c_{1122}, c_{1133}, c_{1123}, c_{1113}, c_{1112})$ and so on, having thus $\hat{c}$ at most 21 independent coordinates.

In an elastic body at temperature T with internal-energy density per unit volume U and entropic density per unit volume S subjected to an elastic, quasistatic, infinitesimal deformation with homogeneous strain $du_{ij} \equiv du_\lambda$ and stress $\hat{T}$; the first and second laws of thermodynamics lead to the internal-energy change:

$$dU = TdS + \delta W = TdS + T_{ij}du_{ij} \overset{\text{(Voigt notation)}}{\equiv} TdS + T_\lambda du_\lambda \ , \tag{B.1.5}$$

since the infinitesimal work per unit volume in the elastic solid can be shown to be given by the double-dot product $\delta W = \hat{T} : d\hat{u} = T_{ij}\, du_{ij}$. This allows to express the stress tensor as the derivative (at constant entropy):

$$T_\lambda = \left(\frac{\partial U}{\partial u_\lambda} \right)_S . \tag{B.1.6}$$

For isothermal processes, it is more convenient to use differentials of other thermodynamic potentials as the Helmholtz free energy $F = U - TS$ or the Gibbs free energy $G = U - TS - u_\lambda T_\lambda = F - u_\lambda T_\lambda$, which satisfy the linear

constitutive equations:

$$dF = -SdT + T_\lambda du_\lambda \ , \tag{B.1.7}$$

$$dG = -SdT - u_\lambda dT_\lambda \ , \tag{B.1.8}$$

so that the stress and strain tensors become related by the derivatives at constant temperature:

$$T_\lambda = \left(\frac{\partial F}{\partial u_\lambda}\right)_T \ , \tag{B.1.9}$$

$$u_\lambda = -\left(\frac{\partial G}{\partial T_\lambda}\right)_T \ . \tag{B.1.10}$$

From the exactness of the differentials of the thermodynamic potentials, as given by the Maxwell's relations in thermodynamics, one gets the aforementioned symmetry of the stiffness tensor. For example, at constant temperature:

$$c_{\lambda\mu} = \left(\frac{\partial T_\lambda}{\partial u_\mu}\right)_T = \left(\frac{\partial^2 F}{\partial u_\mu \partial u_\lambda}\right)_T = \left(\frac{\partial^2 F}{\partial u_\lambda \partial u_\mu}\right)_T = \left(\frac{\partial T_\mu}{\partial u_\lambda}\right)_T = c_{\mu\lambda} \ . \tag{B.1.11}$$

B.2 Introduction to piezoelectricity

Any piezoelectric material is a polarizable material and thus it has dielectric properties. To characterize these from a macroscopic point of view, one must work with macroscopic Maxwell equations, first derived by Lorentz, and disregard microscopic local variations associated with the molecular structure [76]. The key electrical magnitudes to describe them are the electric displacement $\mathbf{D}$, the electric field $\mathbf{E}$ and the electric polarization $\mathbf{P}$, which are related (in SI units) as $\mathbf{D} = \varepsilon_0 \mathbf{E} + \mathbf{P}$. In a dielectric material, one must replace this vacuum permittivity constant ε_0 with a general tensor called *permittivity tensor* $\hat{\varepsilon} = \varepsilon_{ij}$ to express the following linear constitutive

equation, similar to the previous Hooke's law:

$$D_i = \varepsilon_{ij} E_j \ . \tag{B.2.1}$$

In a dielectric, elastic body subject to a reversible, infinitesimal process with electric fields E_i, D_i, the electrostatic field-energy density must be added to Eq. (B.1.5) as:

$$dU = TdS + T_\lambda du_\lambda + E_i dD_i \ , \tag{B.2.2}$$

since the work per unit volume of the electric forces can be shown to be $\delta W = \mathbf{E} \cdot d\mathbf{D}$. As in the case of a purely elastic material, sometimes it can be more convenient to introduce other thermodynamic potentials like the Helmholtz free energy $F = U - TS$ or the Gibbs free energy, given in this case by $G = U - TS - u_\lambda T_\lambda - D_k E_k = F - u_\lambda T_\lambda - D_k E_k$, which satisfy the new linear constitutive equations:

$$dF = -S\, dT + T_\lambda\, du_\lambda + E_k\, dD_k \ , \tag{B.2.3}$$

$$dG = -S\, dT - u_\lambda\, dT_\lambda + D_k\, dE_k \ . \tag{B.2.4}$$

In a dielectric, elastic material as thermodynamically described by three independent variables, one being thermal (entropy or temperature), one elastic (strain or stress) and one electric (electric displacement or electric field); any independent variable can be obtained from the first partial derivatives of the thermodynamic potentials, as in the previous subsection. Namely, for example:

$$T_\lambda = \left(\frac{\partial F}{\partial u_\lambda}\right)_{T,\mathbf{D}} \ , \qquad u_\lambda = -\left(\frac{\partial G}{\partial T_\lambda}\right)_{T,\mathbf{E}} \ , \tag{B.2.5}$$

$$E_k = \left(\frac{\partial F}{\partial D_k}\right)_{T,\hat{u}} \ , \qquad D_\lambda = -\left(\frac{\partial G}{\partial E_k}\right)_{T,\hat{T}} \ , ... \tag{B.2.6}$$

and the dielectric tensor from a second partial derivative of a thermodynamic potential, like the elastic tensor. Now:

$$\varepsilon_{ij} = \left(\frac{\partial D_i}{\partial E_j}\right)_{T,\hat{T}} = \left(\frac{-\partial^2 G}{\partial E_j \partial E_i}\right)_{T,\hat{T}} = \left(\frac{-\partial^2 G}{\partial E_i \partial E_j}\right)_{T,\hat{T}} = \left(\frac{\partial D_j}{\partial E_i}\right)_{T,\hat{T}} = \varepsilon_{ji} \ , \tag{B.2.7}$$

proving in addition from basic thermodynamics that this dielectric tensor is symmetrical (this is not general, since it does not hold out of equilibrium or upon introducing magnetic fields [48]). Thus the dielectric tensor allows one to use the Voigt notation with the previous convention:

$$\varepsilon_{ij} = \begin{pmatrix} \varepsilon_{11} & \varepsilon_{12} & \varepsilon_{13} \\ \varepsilon_{12} & \varepsilon_{22} & \varepsilon_{23} \\ \varepsilon_{13} & \varepsilon_{23} & \varepsilon_{33} \end{pmatrix} \overset{\text{(Voigt notation)}}{\equiv} \begin{pmatrix} \varepsilon_1 & \frac{1}{2}\varepsilon_6 & \frac{1}{2}\varepsilon_5 \\ \frac{1}{2}\varepsilon_6 & \varepsilon_2 & \frac{1}{2}\varepsilon_4 \\ \frac{1}{2}\varepsilon_5 & \frac{1}{2}\varepsilon_4 & \varepsilon_3 \end{pmatrix} \ . \tag{B.2.8}$$

Now, in a material with both elastic and dielectric properties, it is possible that the two kinds of magnitudes couple in first order. This manifests macroscopically as the non-vanishing of other second-order derivatives of thermodynamic potentials, giving rise to the piezoelectric effect, described by a third-rank tensor. For example:

$$e_{ijk} = \left(\frac{\partial D_i}{\partial u_{jk}}\right)_{T,\mathbf{E}} = \left(\frac{-\partial^2 G}{\partial u_{jk} \partial E_i}\right)_{T} \overset{\text{(Voigt)}}{\equiv} \left(\frac{-\partial^2 G}{\partial u_{\lambda} \partial E_i}\right)_{T} = \left(\frac{\partial D_i}{\partial u_{\lambda}}\right)_{T,\mathbf{E}} = e_{i\lambda} \ , \tag{B.2.9}$$

the aforementioned *piezoelectric tensor*, having at most 18 independent coordinates. From this relation, one gets immediately the converse piezoelectric effect for these materials, just reversing the order of derivation:

$$e_{i\lambda} = \left(\frac{\partial D_i}{\partial u_{\lambda}}\right)_{T,\mathbf{E}} = \left(\frac{-\partial^2 G_e}{\partial u_{\lambda} \partial E_i}\right)_{T} = \left(\frac{-\partial^2 G_e}{\partial E_i \partial u_{\lambda}}\right)_{T} = -\left(\frac{\partial T_{\lambda}}{\partial E_i}\right)_{T,\hat{u}} = e_{i\lambda} \ , \tag{B.2.10}$$

where we have invoked the electric Gibbs function $G_e = F - D_k E_k$ satisfying $dG_e = -SdT - D_k dE_k + T_\lambda du_\lambda$ [17].

In these piezoelectric materials, the Hooke's law and the proportionality between **D** and **E** are replaced by the more general coupled linear equations (in practice, one must note a difference between the $\hat{\varepsilon}, \hat{e}$ components at constant strain or at constant stress, which are close to each other but not equal. In the following equation, those at constant strain are implied):

$$D_i = \varepsilon_{ik} E_k + e_{i\lambda} u_\lambda \ , \tag{B.2.11}$$

$$T_\mu = - e_{k\mu} E_k + c_{\lambda\mu} u_\lambda \ . \tag{B.2.12}$$

In the Voigt notation, the previous product of the piezoelectric tensor and the strain in the sum can be expressed by the matrix product:

$$e_{ijk} u_{jk} = e_{i\lambda} u_\lambda = \begin{pmatrix} e_{11} & e_{12} & e_{13} & e_{14} & e_{15} & e_{16} \\ e_{21} & e_{22} & e_{23} & e_{24} & e_{25} & e_{26} \\ e_{31} & e_{32} & e_{33} & e_{34} & e_{35} & e_{36} \end{pmatrix} \begin{pmatrix} u_1 \\ u_2 \\ u_3 \\ u_4 \\ u_5 \\ u_6 \end{pmatrix} \ . \tag{B.2.13}$$

Appendix C

Microscopic theories of the piezoelectric effect

C.1 A simple one-dimensional model

Bearing in mind the atomic structure of materials, and of crystals among them, one is led to explain the phenomenon of piezoelectricity in terms of the atoms forming each piezoelectric crystal, where the origin of the physical mechanism underlies.

As a rough, simple one-dimensional example (as in Ref. [18]), one can consider a relatively simple diatomic crystal such as ZnO, which is studied in the main text as a substrate for graphene and which forms the wurtzite structure (see Fig. C.1). Let us consider a row along the Z-direction in the material, that is, the c-axis of the hexagonal structure, where positively charged zinc atoms are alternated with negatively charged oxygen atoms. These rows are repeated along that axis of symmetry and one of them is isolated for the calculations, as in Fig. C.1.

Let Q and $-Q$ be the effective charges of each ion, let K_1 and K_2 be the spring force constants of the short and long bonds, respectively; and let a be the lattice length, that is, the separation between each ZnO molecule in

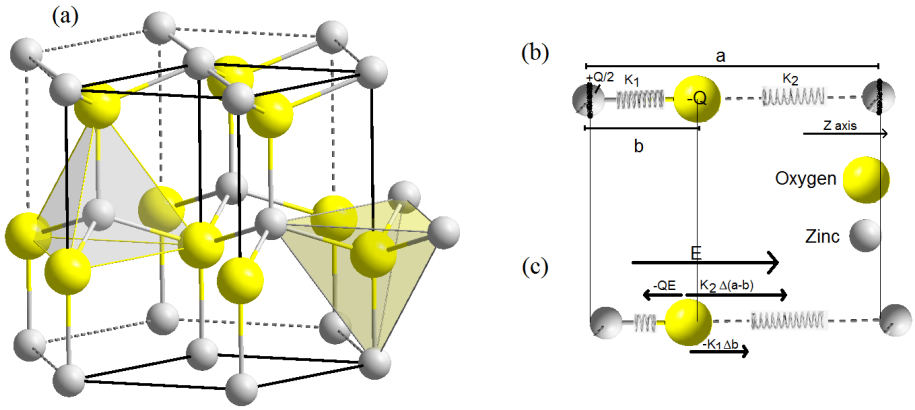

Figure C.1: Microscopic view of the wurtzite structure of ZnO and a rough model for its piezoelectricity in the vertical Z-direction. (a) Atomic structure of the wurtzite showing the bonds between the alternating atoms. Note that the Z-axis is perpendicular to the faces of the hexagonal prisms, and a plane perpendicular to this axis cuts alternating bonds. (b) An elementary part of a row along the (now horizontal) Z-axis showing the two kind of bonds between oxygen and zinc atoms, without any applied forces or strain. (c) Forces applied to an atom in equilibrium after the introduction of a field or a strain.

the lattice, whereas b ($< a$) is the intra-molecule atomic distance. From the equilibrium at rest, the cells are subjected to an applied uniform electric field $E_z \equiv E$ along the positive Z-direction and an uniform strain $u_{zz} = \frac{\Delta a}{a} \equiv U$ along the axis, both either finite or zero.

Now one can consider the unit cell consisting of two electric dipoles, one formed by half the negative O atom (charge $Q/2$) joining half the positive close intra-cell Zn atom; and the other dipole formed by the other half O atom and half the positive far Zn atom from the next cell. The deformation by itself induces an asymmetric change between both dipoles (since the spring constants K_1, K_2 are different) leading to an electric dipole (direct piezoelectric effect), and the applied electric field alone causes the ions to be moved in opposite directions, thus generating a strain (and also stress via the induced forces, which is the inverse piezoelectric effect). If n is the

number of ZnO molecules per unit volume, then $N = na$ is the number of rows crossing the area perpendicular to the axis. This unit area in the wurtzite structure is cut by alternating rows separated by a half period $a/2$, crossing each one by springs of constants K_1 and K_2, as in the picture.

Therefore, in this rough model, the estimates for the induced polarization along the Z-axis $P_z \equiv P$ (electric dipole per unit volume) and stress $T_{zz} \equiv T$ (net force per unit area in the positive Z-direction) are:

$$P = \frac{nQ}{2}\Delta(a-b) - \frac{nQ}{2}\Delta b = \frac{nQ\,(\Delta a - 2\Delta b)}{2}\ , \tag{C.1.1}$$

$$T = \frac{N}{2}K_2\Delta(a-b) + \frac{N}{2}K_1\Delta b = \frac{na}{2}\left[K_2\Delta a + (K_1-K_2)\Delta b\right]\ . \tag{C.1.2}$$

From the forces applied in the oxygen atoms, the equilibrium condition allows to get one displacement from the other:

$$-QE + K_2\Delta(a-b) - K_1\Delta b = 0\ , \tag{C.1.3}$$

so that the electric displacement $D = \varepsilon_0 E + P$ and the stress are finally related to E and u by:

$$D = \left(\varepsilon_0 + \frac{nQ^2}{K_1+K_2}\right)E + \frac{nQ}{2}\frac{K_1-K_2}{K_1+K_2}\,a\,U = \varepsilon E + eU, \tag{C.1.4}$$

$$T = Na^2\frac{K_1K_2}{K_1+K_2}U - \frac{nQ}{2}\frac{K_1-K_2}{K_1+K_2}\,a\,E = cU - eE\ . \tag{C.1.5}$$

In this simple model, one obtains roughly the piezoelectric coefficient $e_{333} \equiv e$, the stiffness constant $c_{3333} \equiv c$ and the dielectric constant $\varepsilon_{33} \equiv \varepsilon$, such that the direct and inverse-piezoelectric-effect laws in Eq. (B.2.10) hold. It is very important to note that the asymmetry is the key ingredient, since there would be no piezoelectricity if both spring constants K_1, K_2 were equal. The real mechanism is more complex, not only because of the dimensionality, because of the tensorial proportionality between the fields and elastic strain and stresses and because of the couplings of the dynamics in all directions; but also because the effect occurs as well in monatomic

crystals. Moreover, everything is much more subtle than the facts that this model can show, as will be seen in the last subsection of this App. C.

C.2 Symmetry considerations

From the knowledge of the symmetry of the crystal, one can infer many restrictions for the piezoelectric tensor, exactly the same that happens with the elasticity (and dielectric) tensor and the elastic (and dielectric) properties [48, 51]. A very immediate result stated in many general solid-state books [86] as an example of a tensor transformation under a symmetry operation, is the fact that no centrosymmetrical material can show piezoelectric properties.

From the 32 possible point groups among the crystals, 11 are centrosymmetric, so they have no piezoelectric effect. This occurs because an inversion operation [namely $(x, y, z) \rightarrow (-x, -y, -z)$] leaves the crystal invariant, but the piezoelectric tensor $\hat{e}$, as a third-rank tensor relating the proportionality between the vector $\mathbf{E}$ and the two-rank strain tensor $\hat{u}$, transforms to minus $\hat{e}$ (i.e., $e_{ijk} \rightarrow -e_{ijk}$). Since the initial and transformed piezoelectric tensors must be equal, also being one opposite of the other, they are both zero.

The non-centrosymmetrical condition is necessary but not sufficient to bear piezoelectricity. The cubic 432 class has no center of symmetry, but its symmetry itself is enough to make all piezoelectric coefficients vanish. The other 20 classes do show piezoelectric properties.

A complete discussion on the crystallographic point groups, their transformations and their effects on the piezoelectric coefficients, together with all the derivations, can be found elsewhere in the literature (e.g. Refs. [17, 18, 22, 23, 51, 123]). As an example, we can show some examples of tensors which are specific of materials used in this thesis.

Trigonal 3m class

For example, $LiNbO_3$ and tourmaline belong to this class.

$$\hat{e} = \begin{pmatrix} 0 & 0 & 0 & 0 & e_{15} & -e_{22} \\ -e_{22} & e_{22} & 0 & e_{15} & 0 & 0 \\ e_{13} & e_{13} & e_{33} & 0 & 0 & 0 \end{pmatrix} , \tag{C.2.1}$$

$$\hat{c} = \begin{pmatrix} c_{11} & c_{12} & c_{13} & c_{14} & 0 & 0 \\ c_{12} & c_{11} & c_{13} & -c_{14} & 0 & 0 \\ c_{13} & c_{13} & c_{33} & 0 & 0 & 0 \\ c_{14} & -c_{14} & 0 & c_{44} & 0 & 0 \\ 0 & 0 & 0 & 0 & c_{44} & 0 \\ 0 & 0 & 0 & 0 & 0 & \frac{c_{11}-c_{12}}{2} \end{pmatrix} , \; \hat{\varepsilon} = \begin{pmatrix} \varepsilon_{11} & 0 & 0 \\ 0 & \varepsilon_{11} & 0 \\ 0 & 0 & \varepsilon_{33} \end{pmatrix} . \tag{C.2.2}$$

Tetragonal 4mm class and hexagonal 6mm class

For example, ferroelectric $BaTiO_3$, PZT and $KNbO_3$ belong to the class 4mm; whereas non-ferroelectric ZnO, CdS, AlN belong to the class 6mm.

$$\hat{e} = \begin{pmatrix} 0 & 0 & 0 & 0 & e_{15} & 0 \\ 0 & 0 & 0 & e_{15} & 0 & 0 \\ e_{31} & e_{31} & e_{33} & 0 & 0 & 0 \end{pmatrix} , \tag{C.2.3}$$

$$\hat{c} = \begin{pmatrix} c_{11} & c_{12} & c_{13} & 0 & 0 & 0 \\ c_{12} & c_{11} & c_{13} & 0 & 0 & 0 \\ c_{13} & c_{13} & c_{33} & 0 & 0 & 0 \\ 0 & 0 & 0 & c_{44} & 0 & 0 \\ 0 & 0 & 0 & 0 & c_{44} & 0 \\ 0 & 0 & 0 & 0 & 0 & c_{66} \end{pmatrix} , \; \hat{\varepsilon} = \begin{pmatrix} \varepsilon_{11} & 0 & 0 \\ 0 & \varepsilon_{11} & 0 \\ 0 & 0 & \varepsilon_{33} \end{pmatrix} . \tag{C.2.4}$$

The only difference among these three tensors for both classes is that for the latter hexagonal 6mm class: $c_{66} = \frac{c_{11}-c_{12}}{2}$ (as in the case of the 3m class).

Cubic 43m class

For example, GaAs and CuI belong to this class.

$$\hat{e} = \begin{pmatrix} 0 & 0 & 0 & e_{14} & 0 & 0 \\ 0 & 0 & 0 & 0 & e_{14} & 0 \\ 0 & 0 & 0 & 0 & 0 & e_{14} \end{pmatrix} , \tag{C.2.5}$$

$$\hat{c} = \begin{pmatrix} c_{11} & c_{12} & c_{12} & 0 & 0 & 0 \\ c_{12} & c_{11} & c_{12} & 0 & 0 & 0 \\ c_{12} & c_{12} & c_{11} & 0 & 0 & 0 \\ 0 & 0 & 0 & c_{44} & 0 & 0 \\ 0 & 0 & 0 & 0 & c_{44} & 0 \\ 0 & 0 & 0 & 0 & 0 & c_{44} \end{pmatrix} , \; \hat{\varepsilon} = \begin{pmatrix} \varepsilon_{11} & 0 & 0 \\ 0 & \varepsilon_{11} & 0 \\ 0 & 0 & \varepsilon_{11} \end{pmatrix} . \tag{C.2.6}$$

C.3 The geometric-phase theory of polarization

After the introduction of a simple atomic model and the following crystal-symmetry considerations (the latter will always remain valid, without any dependence on the model for piezoelectricity but just on the point group of the crystal), one can try to deepen in order to find a precise quantum-theoretical model for the phenomenon of piezoelectricity. A further exploration leads to the conclusion that the first atomic model in Sec. C.1 is more than just rough, it is indeed wrong for several reasons. All the details regarding the problems in the definition of polarization are pointed out in the literature [124, 125, 126]. For the sake of completeness and without trying to go very deeply into a subject which is not the central matter of this thesis, the main points of the precise quantum-mechanical theory shall be described in this subsection, following the review by R. Resta [125].

First of all, the (macroscopic) polarization, given as the dipole moment per unit volume after it is defined inside a unit cell, is ill-defined; even in classical models taking into account the Clausius-Mossotti equation with localized charges, when no ambiguity arises. This problem on the choice of the unit cell is already pointed out in the old literature [76]. Moreover, the existence of covalent bondings would make this definition inapplicable, even in the case that one tries a definition using the precise charge density $\rho(\mathbf{r})$

taking integrals such as $V^{-1}\int d\mathbf{r}\,\mathbf{r}\,\rho(\mathbf{r})$ in the volume V. In this case, the polarization $\mathbf{P}$ would impose problems that are dependent on the surfaces and the shape of the material, and making it to be not a relevant bulk property, well defined in the termodynamic limit.

Regarding the total polarization, one must note that it is actually the "differential" polarization which is measured in the experiment, defined as the variation $\Delta\mathbf{P} = \int d\lambda\,\frac{d\mathbf{P}}{d\lambda}$ in the polarization $\mathbf{P}$ from a previous initial state, induced upon the introduction of some new parameter λ (such as the stress/strain to compute a piezoelectric effect, or the relative displacement between sublattices to compute the polarization from optical phonons). That has actually been done in the rough previous model, since Eq. (C.1.1) was taking implicitly the difference of polarization from the initial state, and not the total dipole moment.

A precise quantum-mechanical description of the macroscopic polarization is possible within the geometric-phase approach [127]. Let us consider the variation of some parameter λ between 0 and 1, other than an external electric field and let us assume zero temperature as well. Let $H^{(\lambda)} = (-i\hbar\partial_{\mathbf{r}})^2/2m_e + V^{(\lambda)}(\mathbf{r})$ be a Hamiltonian of the electronic system in the solid for each value of λ with single-particle eigenstates $\psi_n^{(\lambda)}(\mathbf{r})$, being connected to each other continuously in λ and lying in $\overline{n}$ bands, $n = 1, ..., \overline{n}$. In this one-body scenario, $V^{(\lambda)}$ is given from a Kohn-Sham, Hartree-Fock or any other mean-field electronic potential.

From Bloch's theorem, the single-electron orbitals can be chosen with a wave vector $\mathbf{q}$ so that:

$$\psi_n^{(\lambda)}(\mathbf{r}) = e^{i\mathbf{q}\cdot\mathbf{r}}\,u_n^{(\lambda)}(\mathbf{r})\ , \quad \text{with } u_n^{(\lambda)}(\mathbf{r}+\mathbf{R}_l) = u_n^{(\lambda)}(\mathbf{r}) \tag{C.3.1}$$

for any lattice vector $\mathbf{R}_l$, and these $u_n^{(\lambda)}$ are eigenstates of this other Hamiltonian:

$$H^{(\lambda)}(\mathbf{q}) = \frac{1}{2m_e}\,(-i\hbar\partial_{\mathbf{r}} + \hbar\mathbf{q})^2 + V^{(\lambda)}(\mathbf{r})\ , \tag{C.3.2}$$

provided that the direct-lattice vectors are spanned by the primitive $\mathbf{R}_i$ (with $i = 1, 2, 3$). If the reciprocal-lattice vectors are spanned by the prim-

itive vectors $\mathbf{G}_j$ $(j = 1, 2, 3)$, it is possible to transform the coordinates $(\mathbf{q}, \lambda)$ of the problem to the dimensionless $\xi_k, k = 1, 2, 3, 4$, given by:

$$\mathbf{q} = \xi_1 \mathbf{G}_1 + \xi_2 \mathbf{G}_2 + \xi_3 \mathbf{G}_3 \ , \quad \text{with } \xi_j = \frac{1}{2\pi} \mathbf{q} \cdot \mathbf{R}_j, j = 1, 2, 3 \text{ and } \xi_4 = \lambda \ . \tag{C.3.3}$$

This allows to write the Berry connection and curvature of the problem as

$$\mathbf{X}(\boldsymbol{\xi}) = i \sum_{n=1}^{\overline{n}} \langle u_n(\boldsymbol{\xi}) | \nabla_{\boldsymbol{\xi}} | u_n(\boldsymbol{\xi}) \rangle \ , \tag{C.3.4}$$

$$\mathbf{Y}_{ij} = \frac{\partial X_j(\boldsymbol{\xi})}{\partial \xi_i} - \frac{\partial X_i(\boldsymbol{\xi})}{\partial \xi_j} = 2 \ \mathrm{Im} \sum_{n=1}^{\overline{n}} \left\langle \frac{\partial u_n(\boldsymbol{\xi})}{\partial \xi_i} \middle| \frac{\partial u_n(\boldsymbol{\xi})}{\partial \xi_j} \right\rangle \ , \tag{C.3.5}$$

respectively, the former being gauge-dependent and playing the same role as the usual vector potential in the Aharonov-Bohm effect, while the curvature is gauge-invariant and plays the role of the magnetic field.

Finally, it can be shown [125] that the physical polarization $\Delta\mathbf{P}$ in each direction j is given from the four-dimensional $\boldsymbol{\xi}$-integral in the unit hypercube $[0, 1] \times [0, 1] \times [0, 1] \times [0, 1]$ (Ω is the cell volume):

$$\mathbf{G}_j \cdot \Delta\mathbf{P} = \frac{2e}{\Omega} \int d\boldsymbol{\xi} \ Y_{j4}(\boldsymbol{\xi}) \ , \ j = 1, 2, 3 \ . \tag{C.3.6}$$

It is the fact that a change of polarization induces an electring current (from the continuity equation) that allows one to get a definition of the polarization as a bulk property. At the end, all the relevant information is contained in the phases of the electronic wave functions, which account for the currents, and making a valid definition in the thermodynamic limit. It is not enough to find the charge densities, given from the modulus of the wave functions.

The result in Eq. (C.3.6) can be shown as well to coincide with the ordinary linear-response theory, from a displacement current $\mathbf{j} = \frac{\partial \mathbf{P}}{\partial t}$ obtained

via perturbation theory. The equation here reads (BZ means Brillouin zone):

$$\mathbf{P}(\lambda) = \frac{4\hbar e}{(2\pi)^3 m_e} \mathrm{Im} \sum_{n=1}^{\overline{n}} \sum_{m=\overline{n}+1}^{\infty} \int_{\mathrm{BZ}} d\mathbf{q} \frac{\langle u_n^{(\lambda)}(\mathbf{q}) | \, i\hbar\partial_{\mathbf{r}} \, | u_m^{(\lambda)}(\mathbf{q}) \rangle \, \langle u_m^{(\lambda)}(\mathbf{q}) | \, \partial_\lambda V^{(\lambda)} \, | u_n^{(\lambda)}(\mathbf{q}) \rangle}{\left[E_m^{(\lambda)}(\mathbf{q}) - E_n^{(\lambda)}(\mathbf{q}) \right]^2} \, . \tag{C.3.7}$$

In this section, we have shown how non-trivial and theoretically involved this subject of piezoelectricity actually is, despite its usual orientation for engineers and technicians in the majority of books.

Appendix D

Elastic waves in crystals

D.1 Equation of motion

Focusing on the elastic materials without the piezoelectric effect, it is easy to obtain a wave equation [18, 22, 23, 56] from the most elementary concepts in elasticity theory as summarized in Sec. B.1. It is Newton's second law at each pointlike volume element of the material, whose acceleration is given by the second derivative of the displacement, that is $\partial^2 u_i/\partial t^2 \equiv \ddot{u}_i$, in the directions $i = 1, 2, 3$. As explained in that section, the force (per unit volume) applied on the volume element of the elastic body in that point has its components in each direction i given from the stress tensor, as the sum $\partial T_{ij}/\partial x_j$. This means that Newton's second law reads:

$$\rho \ddot{u}_i = \frac{\partial T_{ij}}{\partial x_j}, \quad i = 1, 2, 3 \ , \tag{D.1.1}$$

where ρ is the mass density, since the forces are given per unit volume, and the fields u_i, T_{ij} are implicitly functions of the three position coordinates and time $(\mathbf{r}, t) = (x_1, x_2, x_3, t)$.

When the approximations of elasticity theory are valid, which is the case for the typical waves in crystals, the previous equations can be written in

terms of just the displacement vector at each point, with the aid of Hooke's law and the definition of strain. That is:

$$\rho\ddot{u}_i = c_{ijkl}\frac{\partial u_{kl}}{\partial x_j} = c_{ijkl}\frac{\partial^2 u_l}{\partial x_j \partial x_k}, \quad i = 1, 2, 3 \ , \tag{D.1.2}$$

where the symmetry of the elastic tensor $\hat{c}$ has been used to rearrange the terms in the sum.

D.2 Plane-wave solutions

Let us suppose the simplest possible solution, that is, a plane-wave solution to the equation of motion with a given wave vector $\mathbf{k} = (k_1, k_2, k_3)$. This wave is given by the real part of:

$$u_i = A_i \exp\left[i(\omega t - \mathbf{k}\cdot\mathbf{r})\right] = A_i \exp\left[i(\omega t - k_j x_j)\right] \ . \tag{D.2.1}$$

Here, A_i is the wave amplitude in the i-direction (whose subscript should not to be confused with $i = \sqrt{-1}$ when it is not a subscript, as in the argument of the exponential), and ω is the angular frequency. Now, in the equation of motion, Eq. (D.1.2), one must note that the time derivative equals the product by $i\omega$ and the space derivative in the j-direction equals the product by ik_j. So the three equations of motion read:

$$(\rho\omega^2\delta_{il} - c_{ijkl}k_j k_k)u_l = 0 = (\rho\omega^2\delta_{il} - c_{ijkl}k_j k_k)A_l \ , \quad i = 1, 2, 3 \ . \tag{D.2.2}$$

These equations are called *Christoffel equations*. This homogeneous linear system of 3 equations has a solution provided that the determinant of the coefficients matrix $(\rho\omega^2\delta_{il} - c_{ijkl}k_j k_k)$ is 0.

From the three roots of ω^2 in the determinant, one obtains the displacements $\mathbf{A}$ (up to an arbitrary global factor due to homogeneity) of the three possible waves. One gets also the phase velocity $\omega/|\mathbf{k}|$ [of order $v \sim (\hat{c}/\rho)^{1/2}$] and the group velocity $\mathbf{v}_g = \partial_{\mathbf{k}}\omega$ (which in general does not have the same direction as $\mathbf{k}$; both velocities are parallel just for some isotropic cases where

ω only depends on $|\mathbf{k}|$). It is to be noted that the function $\omega(\mathbf{k})$ is homogeneous of degree one, which can be seen after dividing the previous equations by $|\mathbf{k}|$. In particular, the group velocity just depends on the direction of propagation, and there are in general three different velocities for each direction, depending on the chosen solution. Those solutions, giving the directions $\mathbf{A}/|\mathbf{A}|$ of the displacements, are orthogonal to each other, since the above determinant gives the principal values of a symmetrical second-rank tensor.

The phase-velocity surface (it is usually the inverse, namely, the slowness surface) can be plotted for different materials, highlighting their anisotropy. Lots of examples can be found in the literature, in particular in those books cited in this section, such as the plots in Fig. D.1.

D.3 The isotropic case

The anisotropic properties among crystals generate wave equations so cumbersome that they can be solved commonly just by numerical methods. But there are isotropic materials such as polycrystalline solids, glasses and normal liquids, whose elastic waves can be easily found, and having solutions that are valid for other materials as a first approximation.

From symmetry considerations, it can be shown [51, 18] that an isotropic material has just two independent components of the elastic tensor, being of the form of an elastic tensor in a cubic crystal [see Eq. (C.2.6)], with the further restriction that $c_{44} = 1/2(c_{11} - c_{12})$. The *Lamé coefficients* are introduced so that the elastic tensor of such material is $c_{ijkl} = \lambda\delta_{ij}\delta_{kl} +$

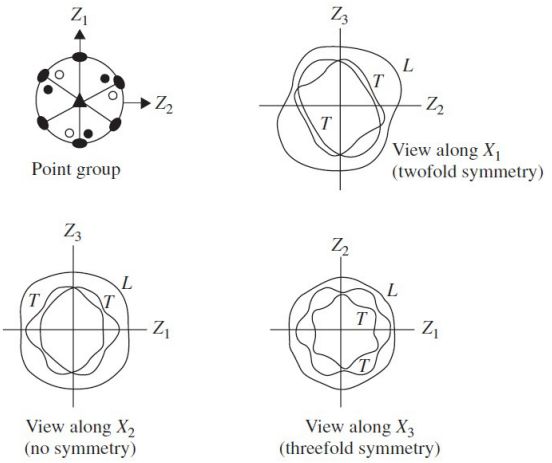

Figure D.1: Point group of α-quartz and wave-velocity surfaces from three different directions. The letters L and T refer to "longitudinal" and "transversal", where the former waves are faster. Actually they are quasi-longitudinal and quasi-transversal, being just purely longitudinal or transversal in some isotropic cases or directions. Here the Z-directions mean $Z_1 = [100], Z_2 = [120], Z_3 = [001]$. Figures taken from Ref. [22].

$\mu(\delta_{ik}\delta_{il} + \delta_{il}\delta_{jk})$, or equivalently:

$$\hat{c} = \begin{pmatrix} \lambda+2\mu & \lambda & \lambda & 0 & 0 & 0 \\ \lambda & \lambda+2\mu & \lambda & 0 & 0 & 0 \\ \lambda & \lambda & \lambda+2\mu & 0 & 0 & 0 \\ 0 & 0 & 0 & \mu & 0 & 0 \\ 0 & 0 & 0 & 0 & \mu & 0 \\ 0 & 0 & 0 & 0 & 0 & \mu \end{pmatrix}, \tag{D.3.1}$$

and Hooke's law becomes:

$$T_{ij} = \lambda\,(u_{11} + u_{22} + u_{33})\,\delta_{ij} + 2\mu\,u_{ij}. \tag{D.3.2}$$

From thermodynamical arguments, it can be shown [48] too that $\mu > 0$ and $\mu + (2/3)\lambda > 0$. Both coefficients are related to the Young's modulus and the Poisson's ratio of the material as well.

Everything together allows one to obtain a relatively simple solution to the acoustic wave with the aid of Eq. (D.2.2) and its notation. Here, it becomes:

$$\rho\omega^2\mathbf{A} = (\lambda + \mu)(\mathbf{k} \cdot \mathbf{A})\mathbf{k} + \mu|\mathbf{k}|^2\mathbf{A} \ . \tag{D.3.3}$$

This equation produces three exact solutions. Two of them have their directions $\mathbf{A}$ perpendicular to $\mathbf{k}$, consisting in pure transverse waves with velocity v_t (they satisfy $\partial_t^2\mathbf{A} = v_t^2\nabla^2\mathbf{A}$, $\nabla \cdot \mathbf{A} = 0$). The other solution has its direction parallel to $\mathbf{k}$, consisting in a pure longitudinal wave with velocity v_l (it satisfies $\partial_t^2\mathbf{A} = v_l^2\nabla^2\mathbf{A}$, $\nabla \times \mathbf{A} = 0$). The velocities, of the order of some thousands of m/s, are independent of the frequency. They are equal to the group velocities, given by:

$$v_t = \sqrt{\frac{\mu}{\rho}} < v_l = \sqrt{\frac{\lambda + 2\mu}{\rho}} \ , \tag{D.3.4}$$

so that the projections of the velocity surfaces (as in the previous Fig. D.1) in this case would consist in three circumferences centered at the origin, two of them with the same radii for the transversal (T) modes, and one with a bigger radius for the longitudinal (L) mode.

Sometimes, the *anisotropy factor* is defined as $A =: 2c_{44}/(c_{11} - c_{12})$ for cubic crystals, so that the closer it is to 1, the more purely longitudinal and transversal the waves are, and the closer to circumferences the curves like those in Fig. D.1 become. This subject is well described in Ref. [56]. In Ref. [21], a table of anisotropic ratios is given for many cubic crystals, ranging from the relatively high value of sodium, $A_{\mathrm{Na}} = 7.00$ to the low value of potassium chloride, $A_{\mathrm{KCl}} = 0.375$, with the almost-isotropic tungsten value in the middle, given by $A_{\mathrm{W}} = 0.995$. There, the influence of this factor on the properties and velocities of some kind of elastic surface waves is shown as well in different crystals

Appendix E

Elastic surface acoustic waves

E.1 Rayleigh waves in isotropic elastic solids

Rayleigh waves were discovered more than 100 years ago [20] and are presented as well in the most basic literature of elasticity theory [51]. In this kind of surface waves, the amplitude of the displacement decays exponentially fast from the surface, such that all the mechanics is essentially concentrated within a distance of the order of the wavelength below the surface (see Fig. E.1a).

Let the infinite isotropic surface be extended in the x_1, x_2-directions and given by the equation $\{x_3 = 0\}$, such that the material occupies the half-space $\{x_3 \leq 0\}$. Then, Rayleigh waves can be described from the longitudinal $\partial^2 \mathbf{u}_l / \partial t^2 = v_l^2 \Delta \mathbf{u}_l$ and transversal $\partial^2 \mathbf{u}_t / \partial t^2 = v_t^2 \Delta \mathbf{u}_t$ components. Both partial waves satisfy the plane-wave condition in Eq. (D.2.1) and are added up to build the Rayleigh wave that satisfies Eq. (D.3.3) and the boundary conditions. Each partial wave is allowed to have imaginary components of

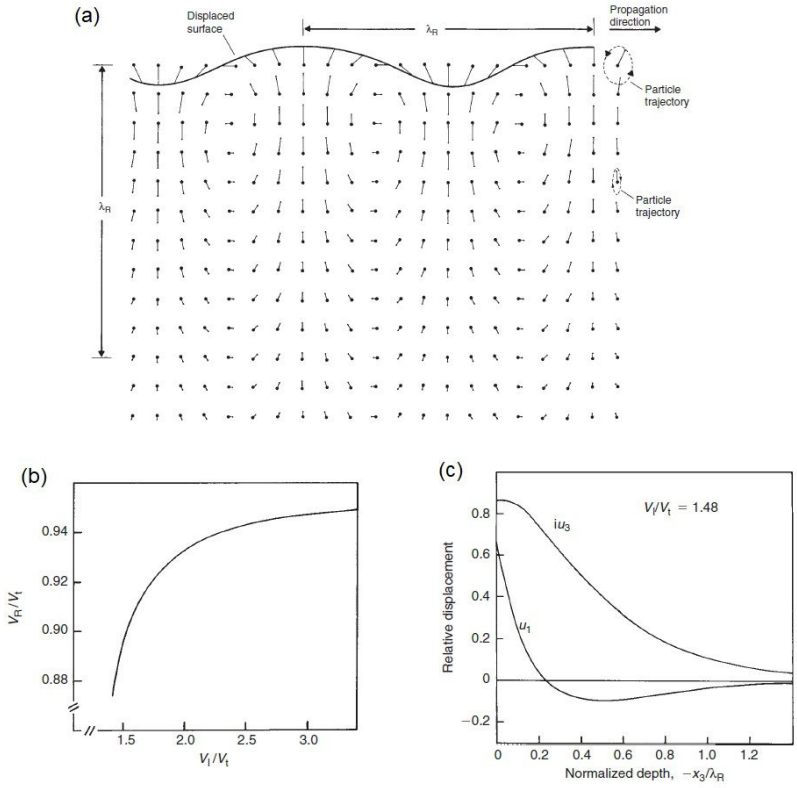

Figure E.1: Properties of a Rayleigh wave including the fast decrease of its displacement below the surface. Here $\lambda_R = 2\pi/q$ is the Rayleigh wavelength. (a) Sketch of the -exaggerated- displacement (the lines) in any point of the material near the surface (at the top layer) from the equilibrium points (the dots). (b) Solutions for $\zeta = v_s/v_t$ as a function of $\sqrt{\alpha} = v_t/v_l$, depending on each material's elastic properties. (c) Amplitudes of the displacements u_3, in the direction perpendicular to the surface and u_1, parallel to the wave vector, as a function of the distance $|x_3|$ to the surface. The factor i is due to the elliptic polarization. Taken from Ref. [23].

the wave vectors $\mathbf{k}_l, \mathbf{k}_t$, in order to decay to the bulk. The solution is:

$$\mathbf{u}_\mathbf{q}(\mathbf{r}, t) = \mathbf{A}_\mathbf{q}(x_3) \exp\left[i(\mathbf{q} \cdot \mathbf{R} - \omega_\mathbf{q} t)\right] \ , \tag{E.1.1}$$

for 3D bulk vectors $\mathbf{r} = (x_1, x_2, x_3)$, $\mathbf{k} = (k_1, k_2, k_3)$ and 2D surface vectors

$\mathbf{R} = (x_1, x_2)$, $\mathbf{q} = (k_1, k_2)$. Due to the general wave equation, to avoid diverging magnitudes when $x_3 \to -\infty$, each component ik_3 in the longitudinal and transversal-wave exponentials must be taken as the (negative) roots $-\sqrt{q^2 - \frac{\omega^2}{v^2}}$, being $v = v_l, v_t$ for each case, respectively.

On the other side, the free surface must satisfy the boundary conditions given by the cancellation of the stresses in the normal direction of the surface, that is:

$$T_{i3}(x_1, x_2, x_3 \equiv 0, t) = 0 \ , \quad i = 1, 2, 3 \ . \tag{E.1.2}$$

All the equations together are enough to obtain the solution. After some algebra, one finds that this Rayleigh wave has elliptic polarization contained in the *saggital plane* (that plane containing the surface normal in the x_3-direction and the wave-propagation direction, given by $\mathbf{q}$). The solution is Eq. (E.1.1) with:

$$\frac{\mathbf{A_q}(z)}{|\mathbf{A_q}(z)|} = -i\hat{\mathbf{q}}\,(e^{\kappa_l q z} - f\kappa_t e^{\kappa_t q z}) + \hat{\mathbf{z}}\,(\kappa_l e^{\kappa_l q z} - f e^{\kappa_t q z}) \ , \tag{E.1.3}$$

provided that $\hat{\mathbf{q}} = \mathbf{q}/q$, $\hat{\mathbf{z}} = \hat{\mathbf{n}}$ are the proper unit vectors, $\kappa_l(\alpha) = \sqrt{1 - \alpha\zeta^2}$, $\kappa_t(\alpha) = \sqrt{1 - \zeta^2}$, $\alpha = v_t^2/v_l^2$, $\omega_{\mathbf{q}} = \zeta v_t q = v_s q$, $f(\alpha) = \sqrt{\kappa_l/\kappa_t}$ and ζ is the solution of a sixth-order equation containing just the parameter α, which determines the sound velocity of the Rayleigh modes v_s (as in Fig. E.1b.) [51, 49]. This number ζ is less than 1 (usually between 0.85-0.97), so that the Rayleigh-wave velocity $v_s = \frac{\omega}{q}$ is less than the transversal velocity in the crystal, which was obvious from the fact that $q > \frac{\omega}{v_t}$.

E.2 Other types of waves

Rayleigh waves are not the only waves that can exist at the surface of an elastic solid. In the case of an isotropic material, though, the only alternative type of surface wave with a nonzero component in a direction perpendicular to the sagittal plane is the SH (shear-horizontal) wave. From the boundary conditions ($T_{13} = T_{23} = T_{33} = 0$ for $z = 0$), one gets that

this is a transversal plane wave with wave vector $\mathbf{q}$ along the surface, and displacement orthogonal to $\mathbf{q}$. It can be shown that this is not a true surface wave, since the displacements are independent of x_3 [23].

Other possibilities arise when the semi-infinite solid is layered, that is, covered with another layer of finite thickness. Such a structure can happen, for example, in the litosphere (Fig. 1.4) or in a surface-wave device, when a metal layer is deposited on a piezoelectric insulator. In this case, there can exist the so-called *Rayleigh layered waves* and the *Love waves*.

The former ones are analogous to the Rayleigh waves of the previous section. One must remember that the 3D wave vector $\mathbf{k} = (q_1, q_2, k_3)$ of the Rayleigh partial waves had k_3 such that ik_3 was the negative root of $q^2 - \omega^2/v^2$, so that $u_3 \underset{x_3 \to -\infty}{\longrightarrow} 0$. Since the first layer is finite, it is possible to take both roots for $ik_3 = \pm\sqrt{q^2 - \omega^2/v^2}$ for the partial solution there. For the surface of the semi-infinite crystal, one must build a Rayleigh wave matching continuously the wave in the layer above, satisfying the boundary conditions, and the general solutions can be found in the literature [23, 56]. As expected intuitively, the velocity of this wave is nearly the same as that occurring at the covering material if its thickness is much bigger than the wavelength (the whole wave would be contained there essentially), and it tends to be the Rayleigh velocity of the semi-infinite material for lower thicknesses. Besides the fundamental Rayleigh modes here described, there exist the higher *Sezawa* modes [128].

For the Love waves, the partial wave in the covering layer is of the SH form (mentioned in the first paragraph) matching a Rayleigh wave in the infinite material. The dispersion properties are similar to those of layered Rayleigh waves. Both kind of waves are shown schematically in Fig. E.2.

There exist as well analogs of the previous waves for materials which are infinite in the x_1, x_2-directions, but bounded in the x_3-direction, such as a parallel-sided plate. In that context, the Rayleigh-type solution is called *Lamb wave*, and there are SH-waves as well.

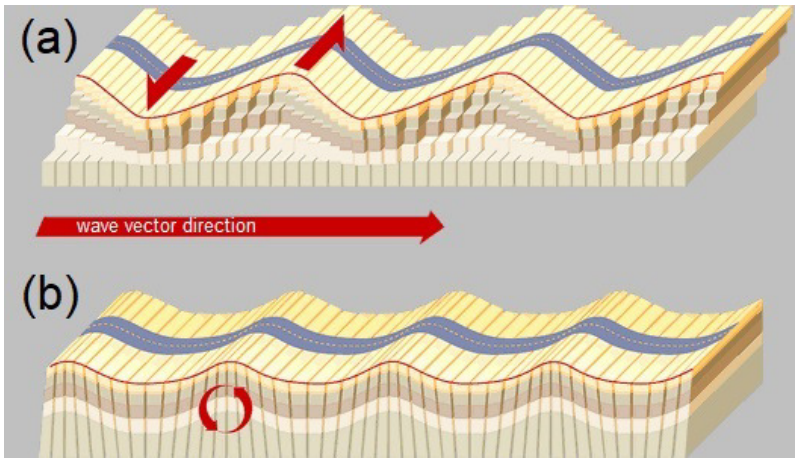

Figure E.2: Different possible surface waves arising at the surface of layered media. (a) Love wave, showing the displacements (red arrows) perpendicular to the wave direction and localized near the surface. (b) Rayleigh layered wave, equivalent to those studied in the previous section (see Sec. E.1).

Appendix F

Piezoelectricity in an elastic medium

F.1 Equation of motion rewritten

In the context of piezoelectricity, one cannot merely apply Hooke's law like in a purely elastic medium, but rather must use its generalization in Eq. (B.2.12), where the electric-field degree of freedom is introduced.

Like the strain, which derives from the mechanical displacement in each point, the electric field derives from a potential, namely, the electric potential φ, i.e., $\mathbf{E} = -\nabla\varphi$. This quasistatic approximation is justified provided that these elastic waves travel much slower than the electromagnetic ones, and this is the case for the studied sound-like waves, since the ratio of the light and sound velocities is of the order of 10^5 (a useful mnemonic rule for many estimates is the rough approximation $c/v_F \sim v_F/v_s \sim 300$, which compares the speed of light and typical Fermi and sound velocities).

A fourth equation is obtained from the electric displacement $\mathbf{D}$ as given in Eq. (B.2.11). In order to relate it to the electric-potential degree of freedom φ, one notes that the piezoelectric solid is taken to be a dielectric insulator, so that the absence of free charges implies $\nabla \cdot \mathbf{D} = 0$. This fact

adds the fourth equation to the previous ones arising for each spatial degree of freedom, and these four equations together read now:

$$\begin{aligned} \rho\ddot{u}_i &= c_{ijkl}\frac{\partial^2 u_k}{\partial x_j \partial x_l} + e_{kij}\frac{\partial^2 \varphi}{\partial x_j \partial x_k} \ , \quad i = 1,2,3 \ , \\ 0 &= \varepsilon_{jk}\frac{\partial^2 \varphi}{\partial x_j \partial x_k} - e_{jkl}\frac{\partial^2 u_k}{\partial x_j \partial x_l} \ , \end{aligned} \tag{F.1.1}$$

analogous to the three equations in (D.1.2).

F.2 Plane waves in the bulk. Piezoelectric stiffening

For the simplest case of a plane wave in an infinite material, namely, a wave described by the displacement in Eq. (D.2.1), the set of equations are supplemented with the electric-potential degree of freedom. The solution is assumed to be the real part of:

$$\begin{aligned} u_i &= A_i \exp\left[i(\omega t - \mathbf{k}\cdot\mathbf{r})\right] \ , \quad i = 1,2,3, \\ \varphi &= A_4 \exp\left[i(\omega t - \mathbf{k}\cdot\mathbf{r})\right] \ . \end{aligned} \tag{F.2.1}$$

The new equations of motion, Eq. (F.1.1), modify the previous Christoffel equations [see Eq. (D.2.2)]. Now it is necessary to solve:

$$\begin{aligned} \rho\omega^2 u_i &= c_{ijkl}k_j k_l u_k + e_{kij}k_j k_k \varphi \ , \quad i = 1,2,3 \ , \\ 0 &= e_{jkl}k_l k_j u_k - \varepsilon_{jk}k_j k_k \varphi \ . \end{aligned} \tag{F.2.2}$$

After substitution in φ, the modified Christoffel equations read:

$$\left[\rho\omega^2\delta_{ik} - c_{ijkl}k_j k_l - \frac{(e_{mkn}k_m k_n)(e_{jil}k_j k_l)}{\varepsilon_{mn}k_m k_n}\right] A_k \ , \quad i = 1,2,3 \ . \tag{F.2.3}$$

This implies that one must address a new problem which appears to be equal to the pure-elastic-wave-propagation problem in Sec. D.2 albeit with

a correction to the coefficients matrix in Eq. (D.2.2) given by terms of the form $C_i C_k/C$, with $C_i = e_{jil}k_j k_l$, $C = \varepsilon_{jl}k_j k_l$. This correction takes into account the new electric forces which appear in the material upon inclusion of the piezoelectric effect and which are added to the elastic restoring forces.

This relative correction to the purely elastic problem is always of order (relative to the term $c_{ijkl}k_j k_l$) $\hat{e}^2/\hat{\varepsilon}\hat{c}$ and is called *piezoelectric stiffening*. It is measured in a given direction by a number, called the *electromechanical coupling constant/factor*, which is $K^2 = e^2/\varepsilon c$ in a rough 1D model, as it is well illustrated in Ref. [30]. This very important number measures also the relative change in velocity $(v - v_0)/v_0$ from an acoustic wave propagation without piezoelectricity, whose velocity v_0 is of the order of $v_0 \sim \sqrt{\rho/\hat{c}}$ (see Sec. D.2), to the new scenario with piezoelectric-stiffened elastic constants of the order $\hat{c} \to \hat{c}\,(1 + {}^{\hat{e}^2}/_{\hat{\varepsilon}\hat{c}})$.

Of fundamental importance for the topic of surface acoustic waves is the boundedness of this coefficient, which will be seen to be very restricted to small numbers, usually a few percent and sometimes zero for some specific propagation directions, as can be seen in the change of the slowness surfaces [22]. The more piezoelectric a material is (as measured by the constants of the tensor $\hat{e}$, sometimes as big as dozens of $\mathrm{C/m^2}$), the bigger the constants in $\hat{c}$ and $\hat{\varepsilon}$ are. For example, in quartz one has $\hat{c} \sim 0.1\,\mathrm{C/m^2}$ and $\varepsilon \simeq 5\,\varepsilon_{\mathrm{vac}}$, so that the electromechanical factor for waves travelling along the Z-axis is $K^2 = {}^{e_{33}^2}/_{c_{33}\varepsilon_{33}} \simeq 0.0085$. The ferroelectric PZT has $\hat{e} \simeq 20\,\mathrm{C/m^2}$, which increases $\hat{e}^2$ by four orders of magnitude, but ε turns to be so large ($\sim 10^2$-$10^3\varepsilon_{\mathrm{vac}}$) that $K^2 \simeq 0.36$. An intermediate case is found in lithium niobate, where $\hat{e}$ is of order $1\,\mathrm{C/m^2}$ and ε some dozens of $\varepsilon_{\mathrm{vac}}$, yielding $K^2 \simeq 0.027$.

The smallness of these corrections also proves that the isotropic or purely elastic approximation can be an excellent one in many cases. In particular, it is still possible to speak of quasi-longitudinal or quasi-transversal waves. More important for this work are the piezoelectric (quasi-)Rayleigh waves, described for isotropic materials in App. E and detailed in Ch. 2.

F.3 Power flow. Energy of a displacement field

Any acoustic disturbance in a piezoelectric crystal involves the generation, storage and transport of energy. Their description comes from the basic energetic considerations of these materials, as discussed in App. B.1 and shown in Eqs. (B.1.5), (B.2.2).

The instantaneous internal-energy density is given from these considerations by products of the form

$$E_p = T_{ij} u_{ij} + E_i D_i \ , \tag{F.3.1}$$

which must be added to the kinetic-energy density per unit volume at each point, given by:

$$E_k = \frac{1}{2} \rho \dot{u}_i^2 \ . \tag{F.3.2}$$

In the linear elasticity theory, when the linear Eqs. (B.2.11), (B.2.12) hold, both quantities can be readily expressed in terms of just the four fields u_i, φ. For example, in an elastic, isotropic, non-piezoelectric material as extensively studied in the Apps. E, D.3, the total energy functional can be written [49, 51]:

$$E[\mathbf{u}] = \frac{1}{2}\, \rho \int_{\mathrm{V}} d^3\mathbf{r} \left[(\ddot{\mathbf{u}})^2 + (v_l^2 - 2v_t^2)(\nabla \cdot \mathbf{u})^2 + 2v_t^2 \sum_{ij} (u_{ij})^2 \right] \ , \tag{F.3.3}$$

where the two acoustic (longitudinal and transversal) velocities are given in terms of the elastic coefficients appearing in Hooke's law, Eq. (D.3.4).

When the wave solutions are given in terms of the typical harmonic, plane-wave, complex functions as in Eq. (F.2.1) and it is needed to compute the time-average energy, it is easy to show that the mean values of the previous energy densities are given by:

$$\langle E_p \rangle = \frac{1}{2} \mathrm{Re} \left(T_{ij} u_{ij}^* + E_i D_i^* \right) , \qquad \langle E_k \rangle = \frac{1}{2} \mathrm{Re} \left(\frac{1}{2} \rho \dot{u}_i \dot{u}_i^* \right) = \frac{1}{4} \rho \dot{u}_i \dot{u}_i^* \ . \tag{F.3.4}$$

F.4 Poynting's theorem for piezoelectrics

There exists a variant of Poynting's theorem for piezoelectric media analogous to the famous theorem for electromagnetic fields. The latter (merely electromagnetic) theorem reads [56, 65]:

$$\frac{\partial u}{\partial t} + \nabla \cdot \mathbf{S} = -\mathbf{J} \cdot \mathbf{E} \ , \tag{F.4.1}$$

where $u = {}^1\!/_2(\mathbf{E} \cdot \mathbf{D} + \mathbf{B} \cdot \mathbf{H})$ is the energy density of the electric and magnetic fields, $\mathbf{J}$ is the current density and $\mathbf{S} = \mathbf{E} \times \mathbf{H}$ is the Poynting vector. Integrating that differential expression in an arbitrary volume with the aid of the divergence theorem, one finds an important energy-balance result: the change in the electromagnetic energy in any region of the space per unit time is given by the sum of the work exerted by the field forces and the energy radiated outwards from the volume in that unit time. The energy radiated away is given exactly by the flux of the Poynting vector $\mathbf{S}$ through the surface embracing that volume.

Analogous principles operate in a piezoelectric material [18, 21, 56]. In this scenario, the change of energy density stored in the fields is given by the time derivative ${}^d\!/_{dt}(E_k + E_p)$ of the sum of the energies in Eqs. (F.3.1), (F.3.2). It can be shown from the wave equation (D.1.2) and both energy-density expressions, that the work density w per unit volume exerted by the mechanical and electric fields follows the rate

$$\frac{dw}{dt} = \frac{d}{dt}(E_k + E_p) + \nabla \cdot \mathbf{P} \ , \tag{F.4.2}$$

where the generalized piezoelectric Poynting vector is given by the expression:

$$P_i(\mathbf{r}, t) = -T_{ij}\frac{\partial u_j}{\partial t} + \varphi\frac{\partial D_i}{\partial t} \ . \tag{F.4.3}$$

Again, in the case of plane-wave, complex, harmonic solutions such as those in Eq. (F.2.1), the piezoelectric time-averaged Poynting vector can be

rewritten as

$$\langle P_i(\mathbf{r},t)\rangle = \frac{1}{2}\mathrm{Re}\left(-T_{ij}\frac{\partial u_j^*}{\partial t} + \varphi\frac{\partial D_i^*}{\partial t}\right) , \tag{F.4.4}$$

which, when averaged in time, leads to (F.4.2).

Bibliography

[1] D. G. González, F. Sols, F. Guinea, and I. Zapata, "Electron-phonon vertex and its influence on the superconductivity of two-dimensional metals on a piezoelectric substrate," *Phys. Rev. B*, vol. 94, p. 085423, 2016. [9 pp.].

[2] D. G. González, I. Zapata, J. Schiefele, F. Sols, and F. Guinea, "Many-body effects in doped graphene on a piezoelectric substrate," *Phys. Rev. B*, vol. 96, p. 125119, 2017. [12 pp.].

[3] K. S. Novoselov, A. K. Geim, S. V. Morozov, D. Jiang, Y. Zhang, S. V. Dubonos, I. V. Grigorieva, and A. A. Firsov, "Electric field effect in atomically thin carbon films," *Science*, vol. 306, pp. 666–669, 2004.

[4] M. S. Dresselhaus and P. T. Araujo, "Perspectives on the 2010 nobel prize in physics for graphene," *ACS Nano*, vol. 4, pp. 6297–6302, 2010.

[5] A. H. Castro Neto, F. Guinea, N. M. R. Peres, K. S. Novoselov, and A. K. Geim, "The electronic properties of graphene," *Rev. Mod. Phys.*, vol. 81, pp. 109–162, 2009.

[6] M. Katsnelson, *Graphene: Carbon in Two Dimensions.* Cambridge University Press, 2012.

[7] S. Das Sarma, S. Adam, E. H. Hwang, and E. Rossi, "Electronic transport in two-dimensional graphene," *Rev. Mod. Phys.*, vol. 83, pp. 407–470, 2011.

[8] K. S. Novoselov, D. Jiang, F. Schedin, T. J. Booth, V. V. Khotkevich,

S. V. Morozov, and A. K. Geim, "Two-dimensional atomic crystals," *Proceedings of the National Academy of Science*, vol. 102, pp. 10451–10453, 2005.

[9] K. S. Novoselov, A. K. Geim, S. V. Morozov, D. Jiang, M. I. Katsnelson, I. V. Grigorieva, S. V. Dubonos, and A. A. Firsov, "Two-dimensional gas of massless dirac fermions in graphene," *Nature*, vol. 438, pp. 197–200, 2005.

[10] N. D. Mermin, "Crystalline order in two dimensions," *Phys. Rev.*, vol. 176, pp. 250–254, 1968.

[11] J. Meyer, A. Geim, M. Katsnelson, K. Novoselov, T. Booth, and S. Roth, "The structure of suspended graphene sheets," *Nature*, vol. 446, pp. 60–63, 2007.

[12] K. S. Novoselov, A. Mishchenko, A. Carvalho, and A. H. Castro Neto, "2D materials and Van der Waals heterostructures," *Science*, vol. 353, 2016.

[13] K. Bolotin, K. Sikes, Z. Jiang, M. Klima, G. Fudenberg, J. Hone, P. Kim, and H. Stormer, "Ultrahigh electron mobility in suspended graphene," *Solid State Communications*, vol. 146, pp. 351 – 355, 2008.

[14] E. V. Castro, H. Ochoa, M. I. Katsnelson, R. V. Gorbachev, D. C. Elias, K. S. Novoselov, A. K. Geim, and F. Guinea, "Limits on charge carrier mobility in suspended graphene due to flexural phonons," *Phys. Rev. Lett.*, vol. 105, p. 266601, 2010.

[15] R. C. Dean, A. F. Young, I. Meric, C. Lee, L. Wang, S. Sorgenfrei, K. Watanabe, T. Taniguchi, P. Kim, K. L. Shepard, and J. Hone, "Boron nitride substrates for high-quality graphene electronics," *Nat Nano*, vol. 5, pp. 722–726, 2010.

[16] J. Schiefele, F. Sols, and F. Guinea, "Temperature dependence of the conductivity of graphene on boron nitride," *Phys. Rev. B*, vol. 85, p. 195420, 2012.

[17] J. Tichỳ, J. Erhart, E. Kittinger, and J. Prívratská, *Fundamentals of*

Piezoelectric Sensorics: Mechanical, Dielectric, and Thermodynamical Properties of Piezoelectric Materials. Springer Berlin Heidelberg, 2010.

[18] D. Royer and E. Dieulesaint, *Elastic Waves in Solids I: Free and Guided Propagation.* Springer Science & Business Media, 2000.

[19] D. Royer and E. Dieulesaint, *Elastic Waves in Solids II: Generation, Acousto-optic Interaction, Applications.* Springer Science & Business Media, 2000.

[20] L. Rayleigh, "On waves propagated along the plane surface of an elastic solid," *Proceedings of the London Mathematical Society*, vol. s1-17, pp. 4–11, 1885.

[21] G. W. Farnell, "Properties of elastic surface waves," *Physical acoustics*, vol. 6, pp. 109–166, 1970.

[22] R. E. Newnham, *Properties of Materials : Anisotropy, Symmetry, Structure: Anisotropy, Symmetry, Structure*, vol. 11. OUP Oxford, 2004.

[23] D. Morgan, *Surface Acoustic Wave Filters: With Applications to Electronic Communications and Signal Processing.* Academic Press, 2010.

[24] I. Viktorov, *Rayleigh and Lamb Waves: Physical Theory and Applications.* Ultrasonic Technology, Springer US, 2013.

[25] R. M. White and F. W. Voltmer, "Direct piezoelectric coupling to surface elastic waves," *Applied Physics Letters*, vol. 7, pp. 314–316, 1965.

[26] R. M. White and F. W. Voltmer, "Ultrasonic surfacewave amplification in cadmium sulfide," *Applied Physics Letters*, vol. 8, pp. 40–42, 1966.

[27] R. C. Williamson, "Case studies of successful surface-acoustic-wave devices," in *1977 Ultrasonics Symposium*, pp. 460–468, 1977.

[28] K. A. Ingebrigsten, "Surface Waves in Piezoelectrics," *Journal of Ap-*

plied Physics, vol. 40, p. 2681, 1969.

[29] S. H. Simon, "Coupling of surface acoustic waves to a two-dimensional electron gas," *Phys. Rev. B*, vol. 54, pp. 13878–13884, 1996.

[30] A. Wixforth, J. Scriba, M. Wassermeier, J. P. Kotthaus, G. Weimann, and W. Schlapp, "Surface acoustic waves on GaAs/$Al_xGa_{1-x}As$ heterostructures," *Phys. Rev. B*, vol. 40, pp. 7874–7887, 1989.

[31] P. Thalmeier, B. Dóra, and K. Ziegler, "Surface acoustic wave propagation in graphene," *Phys. Rev. B*, vol. 81, p. 041409, 2010.

[32] R. H. Parmenter, "The acousto-electric effect," *Phys. Rev.*, vol. 89, pp. 990–998, 1953.

[33] G. Weinreich and H. G. White, "Observation of the acoustoelectric effect," *Phys. Rev.*, vol. 106, pp. 1104–1106, 1957.

[34] V. I. Fal'ko, S. V. Meshkov, and S. V. Iordanskii, "Acoustoelectric drag effect in the two-dimensional electron gas at strong magnetic field," *Phys. Rev. B*, vol. 47, pp. 9910–9912, 1993.

[35] V. Miseikis, J. E. Cunningham, K. Saeed, R. O'Rorke, and A. G. Davies, "Acoustically induced current flow in graphene," *Appl. Phys. Lett.*, vol. 100, p. 133105, 2012.

[36] L. Bandhu, L. M. Lawton, and G. R. Nash, "Macroscopic acoustoelectric charge transport in graphene," *Appl. Phys. Lett.*, vol. 103, p. 133101, 2013.

[37] T. Poole and G. R. Nash, "Acoustoelectric current in graphene nanoribbons," *Scientific Reports*, vol. 7, 2017.

[38] C. H. W. Barnes, J. M. Shilton, and A. M. Robinson, "Quantum computation using electrons trapped by surface acoustic waves," *Phys. Rev. B*, vol. 62, pp. 8410–8419, 2000.

[39] M. J. A. Schuetz, E. M. Kessler, G. Giedke, L. M. K. Vandersypen, M. D. Lukin, and J. I. Cirac, "Universal quantum transducers based on surface acoustic waves," *Phys. Rev. X*, vol. 5, p. 031031, 2015.

[40] M. R. Connolly, K. L. Chiu, S. P. Giblin, M. Kataoka, J. D. Fletcher, C. Chua, J. P. Griffiths, G. A. C. Jones, V. I. Fal'ko, C. G. Smith, and T. J. B. M. Janssen, "Gigahertz quantized charge pumping in graphene quantum dots," *Nature Nanotechnology*, vol. 8, pp. 417–420, 2013.

[41] R. Arsat, M. Breedon, M. Shafiei, P. Spizziri, S. Gilje, R. Kaner, K. Kalantar-zadeh, and W. Wlodarski, "Graphene-like nano-sheets for surface acoustic wave gas sensor applications," *Chemical Physics Letters*, vol. 467, pp. 344 – 347, 2009.

[42] J. Schiefele, J. Pedrós, F. Sols, F. Calle, and F. Guinea, "Coupling light into graphene plasmons through surface acoustic waves," *Phys. Rev. Lett.*, vol. 111, p. 237405, 2013.

[43] R. Peach, "On the existence of surface acoustic waves on piezoelectric substrates," *IEEE Transactions on Ultrasonics, Ferroelectrics and Frequency Control*, vol. 48, pp. 1308–1320, 2001.

[44] J. Lothe and D. Barnett, "On the existence of surface wave solutions in piezoelectric crystals, an example of non-existence," *Wave Motion*, vol. 1, pp. 107 – 112, 1979.

[45] E. L. Albuquerque, "Surface modes in piezoelectric crystals," *physica status solidi (b)*, vol. 96, pp. 475–482, 1979.

[46] K.-Y. Hashimoto, *Surface acoustic wave devices in telecommunications*. Springer, 2000.

[47] V. Gantmakher and Y. Levinson, *Carrier Scattering in Metals and Semiconductors*. Elsevier Science, 2012.

[48] L. Landau, E. Lifshitz, and L. Pitaevskii, *Electrodynamics of continuous media:*. Pergamon international library of science, technology, engineering, and social studies, Pergamon, 1984.

[49] A. Knäbchen, Y. B. Levinson, and O. Entin-Wohlman, "Surface acoustic-wave attenuation by a two-dimensional electron gas in a strong magnetic field," *Phys. Rev. B*, vol. 54, pp. 10696–10708, 1996.

[50] S. H. Zhang, W. Xu, S. M. Badalyan, and F. M. Peeters, "Piezoelectric surface acoustical phonon limited mobility of electrons in graphene on a gaas substrate," *Phys. Rev. B*, vol. 87, p. 075443, 2013.

[51] L. D. Landau and E. M. Lifshitz, *Theory of elasticity, Volume 7 (Theoretical Physics)*. Butterworth-Heinemann, 1986.

[52] R. Stoneley, "The propagation of surface elastic waves in a cubic crystal," *Proceedings of the Royal Society of London. Series A, Mathematical and Physical Sciences*, pp. 447–458, 1955.

[53] G. Gumbs, G. Azin, and M. Pepper, "Interaction of surface acoustic waves with a narrow electron channel in a piezoelectric material," *Physical Review B*, vol. 57, p. 1654, 1998.

[54] J. L. Bleustein, "A new surface wave in piezoelectric materials," *Appl. Phys. Lett.*, vol. 13, p. 412, 1968.

[55] J. Campbell and W. Jones, "A method for estimating optimal crystal cuts and propagation directions for excitation of piezoelectric surface waves," *Sonics and Ultrasonics, IEEE Transactions on*, vol. 15, pp. 209–217, 1968.

[56] B. Auld, *Acoustic Fields and Waves in Solids*. Krieger Publishing Company, 1990.

[57] K. Hashimoto and M. Yamaguchi, "Free software products for simulation and design of surface acoustic wave and surface transverse wave devices," in *Proceedings of 1996 IEEE International Frequency Control Symposium*, pp. 300–306, 1996.

[58] J. Lothe and D. M. Barnett, "Integral formalism for surface waves in piezoelectric crystals. existence considerations," *J. Appl. Phys.*, vol. 47, pp. 1799–1807, 1976.

[59] A. N. Darinskii, E. Le Clezio, and G. Feuillard, "Acoustic waves in the vicinity of the normal to the surface of piezoelectric crystals," *IEEE Transactions on Ultrasonics, Ferroelectrics, and Frequency Control*, vol. 54, pp. 612–620, 2007.

[60] R. Kubo, M. Toda, and N. Hashitsume, *Statistical physics II: nonequilibrium statistical mechanics*, vol. 31. Springer Science & Business Media, 2012.

[61] G. D. Mahan, *Many-Particle Physics*. Springer Science & Business Media, 2013.

[62] R. D. Mattuck, *A Guide to Feynman Diagrams in the Many-Body Problem*. Courier Corporation, 2012.

[63] A. Fetter and J. Walecka, *Quantum Theory of Many-particle Systems*. Dover Books on Physics, Dover Publications, 2003.

[64] C. Kittel, *Quantum theory of solids*. Wiley, 1963.

[65] J. D. Jackson, *Classical electrodynamics*. New York, NY: Wiley, 3rd ed., 1999.

[66] T. Ando, A. B. Fowler, and F. Stern, "Electronic properties of two-dimensional systems," *Rev. Mod. Phys.*, vol. 54, pp. 437–672, 1982.

[67] S. Das Sarma, S. Adam, E. H. Hwang, and E. Rossi, "Electronic transport in two-dimensional graphene," *Rev. Mod. Phys.*, vol. 83, pp. 407–470, 2011.

[68] S. Q. Wang and G. D. Mahan, "Electron scattering from surface excitations," *Phys. Rev. B*, vol. 6, pp. 4517–4524, 1972.

[69] N. Mori and T. Ando, "Electron optical-phonon interaction in single and double heterostructures," *Phys. Rev. B*, vol. 40, pp. 6175–6188, 1989.

[70] M. V. Fischetti, D. A. Neumayer, and E. A. Cartier, "Effective electron mobility in Si-inversion layers in metal-oxide-semiconductor systems with a high-κ insulator: The role of remote phonon scattering," *Journal of Applied Physics*, vol. 90, pp. 4587–4608, 2001.

[71] E. H. Hwang, R. Sensarma, and S. Das Sarma, "Plasmon-phonon coupling in graphene," *Phys. Rev. B*, vol. 82, p. 195406, 2010.

[72] A. S. Alexandrov, *Theory of Superconductivity: From Weak to Strong*

Coupling. CRC Press, 2003.

[73] A. S. Alexandrov and J. T. Devreese, *Advances in Polaron Physics*. Springer Science & Business Media, 2009.

[74] J. T. Devreese, "Polarons," *Encyclopedia of Applied Physics*, vol. 14, p. 383, 1996.

[75] D. Emin, *Polarons*. Cambridge University Press, 2013.

[76] N. W. Ashcroft and N. D. Mermin, *Solid State Physics*. Cengage Learning, 2011.

[77] B. Wunsch, T. Stauber, F. Sols, and F. Guinea, "Dynamical polarization of graphene at finite doping," *New J. Phys.*, vol. 8, pp. 318–318, 2006.

[78] S. Fratini and F. Guinea, "Substrate-limited electron dynamics in graphene," *Phys. Rev. B*, vol. 77, p. 195415, 2008.

[79] J.-H. Chen, C. Jang, S. Xiao, M. Ishigami, and M. S. Fuhrer, "Intrinsic and extrinsic performance limits of graphene devices on SiO_2," *Nat Nano*, vol. 3, pp. 206–209, 2008.

[80] B. Amorim, J. Schiefele, F. Sols, and F. Guinea, "Coulomb drag in graphene-boron nitride heterostructures: Effect of virtual phonon exchange," *Phys. Rev. B*, vol. 86, p. 125448, 2012.

[81] Z.-Y. Ong and M. V. Fischetti, "Theory of interfacial plasmon-phonon scattering in supported graphene," *Phys. Rev. B*, vol. 86, p. 165422, 2012.

[82] Z.-Y. Ong and M. V. Fischetti, "Top oxide thickness dependence of remote phonon and charged impurity scattering in top-gated graphene," *Applied Physics Letters*, vol. 102, p. 183506, 2013.

[83] K. Zou, X. Hong, D. Keefer, and J. Zhu, "Deposition of high-quality HfO_2 on graphene and the effect of remote oxide phonon scattering," *Phys. Rev. Lett.*, vol. 105, p. 126601, 2010.

[84] E. H. Hwang and S. Das Sarma, "Surface polar optical phonon in-

teraction induced many-body effects and hot-electron relaxation in graphene," *Phys. Rev. B*, vol. 87, p. 115432, 2013.

[85] J. Bardeen and W. Shockley, "Deformation potentials and mobilities in non-polar crystals," *Phys. Rev.*, vol. 80, pp. 72–80, 1950.

[86] W. Harrison, *Solid State Theory*. Dover Books on Physics, Dover Publications, 1980.

[87] B. Scharf, V. Perebeinos, J. Fabian, and P. Avouris, "Effects of optical and surface polar phonons on the optical conductivity of doped graphene," *Phys. Rev. B*, vol. 87, p. 035414, 2013.

[88] K. Kaasbjerg, K. S. Thygesen, and K. W. Jacobsen, "Unraveling the acoustic electron-phonon interaction in graphene," *Phys. Rev. B*, vol. 85, p. 165440, 2012.

[89] H. Min, E. H. Hwang, and S. Das Sarma, "Chirality-dependent phonon-limited resistivity in multiple layers of graphene," *Phys. Rev. B*, vol. 83, p. 161404, 2011.

[90] E. H. Hwang and S. Das Sarma, "Acoustic phonon scattering limited carrier mobility in two-dimensional extrinsic graphene," *Phys. Rev. B*, vol. 77, p. 115449, 2008.

[91] J. Pedrós, L. García-Gancedo, C. J. B. Ford, C. H. W. Barnes, J. P. Griffiths, G. A. C. Jones, and A. J. Flewitt, "Guided propagation of surface acoustic waves and piezoelectric field enhancement in ZnO/GaAs systems," *J. Appl. Phys.*, vol. 110, p. 103501, 2011.

[92] H. F. Tiersten, *Linear Piezoelectric Plate Vibrations*. Springer, 1969.

[93] R. S. Weis and T. K. Gaylord, "Lithium niobate: Summary of physical properties and crystal structure," *Applied Physics A*, vol. 37, pp. 191–203, 1985.

[94] S. Sanna and W. G. Schmidt, "Lithium niobate X-cut, Y-cut, and Z-cut surfaces from ab initio theory," *Phys. Rev. B*, vol. 81, p. 214116, 2010.

[95] H. Ezawa, "Phonons in a half space," *Annals of Physics*, vol. 67, pp. 438 – 460, 1971.

[96] E. H. Hwang and S. Das Sarma, "Dielectric function, screening, and plasmons in two-dimensional graphene," *Phys. Rev. B*, vol. 75, p. 205418, 2007.

[97] G. Giuliani and G. Vignale, *Quantum Theory of the Electron Liquid*. Cambridge University Press, 2005.

[98] M. Einenkel and K. B. Efetov, "Possibility of superconductivity due to electron-phonon interaction in graphene," *Phys. Rev. B*, vol. 84, p. 214508, 2011.

[99] F. Guinea and B. Uchoa, "Odd-momentum pairing and superconductivity in vertical graphene heterostructures," *Phys. Rev. B*, vol. 86, p. 134521, 2012.

[100] L. P. Gor'kov, "Peculiarities of superconductivity in the single-layer FeSe/$SrTiO_3$ interface," *Phys. Rev. B*, vol. 93, p. 060507, 2016.

[101] W. Kohn and J. Luttinger, "New mechanism for superconductivity," *Physical Review Letters*, vol. 15, p. 524, 1965.

[102] P. Morel and P. W. Anderson, "Calculation of the superconducting state parameters with retarded electron-phonon interaction," *Phys. Rev.*, vol. 125, pp. 1263–1271, 1962.

[103] N. J. G. Couto, D. Costanzo, S. Engels, D.-K. Ki, K. Watanabe, T. Taniguchi, C. Stampfer, F. Guinea, and A. F. Morpurgo, "Random strain fluctuations as dominant disorder source for high-quality on-substrate graphene devices," *Phys. Rev. X*, vol. 4, p. 041019, 2014.

[104] Q. Li and S. Das Sarma, "Finite temperature inelastic mean free path and quasiparticle lifetime in graphene," *Phys. Rev. B*, vol. 87, p. 085406, 2013.

[105] W.-K. Tse and S. Das Sarma, "Phonon-induced many-body renormalization of the electronic properties of graphene," *Phys. Rev. Lett.*,

vol. 99, p. 236802, 2007.

[106] T. Ando, "Screening effect and impurity scattering in monolayer graphene," *J. Phys. Soc. Jpn.*, vol. 75, p. 074716, 2006.

[107] X. Hong, A. Posadas, K. Zou, C. H. Ahn, and J. Zhu, "High-mobility few-layer graphene field effect transistors fabricated on epitaxial ferroelectric gate oxides," *Phys. Rev. Lett.*, vol. 102, p. 136808, 2009.

[108] N. Sule and I. Knezevic, "Phonon-limited electron mobility in graphene calculated using tight-binding Bloch waves," *Journal of Applied Physics*, vol. 112, p. 053702, 2012.

[109] A. Migdal, "Interaction between electrons and lattice vibrations in a normal metal," *Sov. Phys. JETP*, vol. 7, pp. 996–1001, 1958.

[110] S. Das Sarma, E. H. Hwang, and W.-K. Tse, "Many-body interaction effects in doped and undoped graphene: Fermi liquid versus non-fermi liquid," *Phys. Rev. B*, vol. 75, p. 121406, 2007.

[111] D. C. Elias, R. V. Gorbachev, A. S. Mayorov, S. V. Morozov, A. A. Zhukov, P. Blake, L. A. Ponomarenko, I. V. Grigorieva, K. S. Novoselov, F. Guinea, and A. K. Geim, "Dirac cones reshaped by interaction effects in suspended graphene," *Nat. Phys.*, vol. 7, pp. 701–704, 2011.

[112] J. T. Ye, Y. J. Zhang, R. Akashi, M. S. Bahramy, R. Arita, and Y. Iwasa, "Superconducting dome in a gate-tuned band insulator," *Science (New York, N.Y.)*, vol. 338, pp. 1193–6, 2012.

[113] R. Roldán, E. Cappelluti, and F. Guinea, "Interactions and superconductivity in heavily doped MoS_2," *Phys. Rev. B*, vol. 88, p. 054515, 2013.

[114] J. Chapman, Y. Su, C. A. Howard, D. Kundys, A. N. Grigorenko, F. Guinea, A. K. Geim, I. V. Grigorieva, and R. R. Nair, "Superconductivity in Ca-doped graphene laminates," *Scientific Reports*, vol. 6, 2016.

[115] G. Profeta, M. Calandra, and F. Mauri, "Phonon-mediated superconductivity in graphene by lithium deposition," *Nat. Phys.*, vol. 8, pp. 131–134, 2012.

[116] Y. Cao, V. Fatemi, A. Demir, S. Fang, S. L. Tomarken, J. Y. Luo, J. D. Sanchez-Yamagishi, K. Watanabe, T. Taniguchi, E. Kaxiras, R. C. Ashoori, and P. Jarillo-Herrero, "Correlated insulator behaviour at half-filling in magic-angle graphene superlattices," *Nature*, 2018.

[117] A. S. Alexandrov, "Breakdown of the Migdal-Eliashberg theory in the strong-coupling adiabatic regime," *Europhys. Lett. (EPL)*, vol. 56, pp. 92–98, 2001.

[118] S. Bidmeshkipour, A. Vorobiev, M. A. Andersson, A. Kompany, and J. Stake, "Effect of ferroelectric substrate on carrier mobility in graphene field-effect transistors," *Appl. Phys. Lett.*, vol. 107, p. 173106, 2015.

[119] E. B. Song, B. Lian, S. M. Kim, S. Lee, T.-K. Chung, M. Wang, C. Zeng, G. Xu, K. Wong, Y. Zhou, H. I. Rasool, D. H. Seo, H.-J. Chung, J. Heo, S. Seo, and K. L. Wang, "Robust bi-stable memory operation in single-layer graphene ferroelectric memory," *Applied Physics Letters*, vol. 99, p. 042109, 2011.

[120] P. R. Wallace, "The band theory of graphite," *Phys. Rev.*, vol. 71, pp. 622–634, 1947.

[121] G. W. Semenoff, "Condensed-matter simulation of a three-dimensional anomaly," *Phys. Rev. Lett.*, vol. 53, pp. 2449–2452, 1984.

[122] J. Bjorken and S. Drell, *Relativistic quantum mechanics*. International series in pure and applied physics, McGraw-Hill, 1964.

[123] J. Nye, *Physical Properties of Crystals: Their Representation by Tensors and Matrices*. Oxford science publications, Clarendon Press, 1985.

[124] R. D. King-Smith and D. Vanderbilt, "Theory of polarization of crystalline solids," *Phys. Rev. B*, vol. 47, pp. 1651–1654, 1993.

[125] R. Resta, "Macroscopic polarization in crystalline dielectrics: the geometric phase approach," *Rev. Mod. Phys.*, vol. 66, pp. 899–915, 1994.

[126] R. M. Martin, *Electronic Structure: Basic Theory and Practical Methods*. Cambridge University Press, 2004.

[127] A. Bohm, A. Mostafazadeh, H. Koizumi, Q. Niu, and J. Zwanziger, *The Geometric Phase in Quantum Systems: Foundations, Mathematical Concepts, and Applications in Molecular and Condensed Matter Physics*. Springer Science & Business Media, 2013.

[128] K. Sezawa, "Dispersion of elastic waves propagated on the surface of stratified bodies and on curved surfaces," *Bull. Earthquake Res. Inst. Tokyo*, vol. 3, pp. 1–18, 1927.